AD-770 629

OPTICS RESEARCH, 1973:1

Robert H. Rediker

Massachusetts Institute of Technology

AD 770 629

DOCUMENT CONTROL DATA - R&D

(Security classification of title, body of abstract and indexing annotation must be entered when the overall report is classified)

1. ORIGINATING ACTIVITY *(Corporate author)*	2a. REPORT SECURITY CLASSIFICATION
Lincoln Laboratory, M.I.T.	UNCLASSIFIED
	2b. GROUP

3. REPORT TITLE

Optics Research

4. DESCRIPTIVE NOTES *(Type of report and inclusive dates)*

Semiannual Report — 1 January through 30 June 1973

5. AUTHOR(S) *(Last name, first name, initial)*

Rediker, Robert H.

6. REPORT DATE	7a. TOTAL NO. OF PAGES	7b. NO. OF REFS
30 June 1973	84	50

8a. CONTRACT OR GRANT NO. F19628-73-C-0002	9a. ORIGINATOR'S REPORT NUMBER(S)
b. PROJECT NO. ARPA Order 600	Optics Research (1973:1)
c.	9b. OTHER REPORT NO(S) *(Any other numbers that may be assigned this report)*
d.	ESD-TR-73-231

10. AVAILABILITY/LIMITATION NOTICES

Approved for public release; distribution unlimited.

11. SUPPLEMENTARY NOTES	12. SPONSORING MILITARY ACTIVITY
None	Advanced Research Projects Agency, Department of Defense Air Force Systems Command, USAF

13. ABSTRACT

This report covers work of the Optics Division at Lincoln Laboratory for the period 1 January through 30 June 1973. The topics covered are laser technology and propagation and optical measurements and instrumentation.

Additional information on the optics program may be found in the semiannual technical summary reports to the Advanced Research Projects Agency.

14. KEY WORDS

optics	optical devices	KC-135
laser technology	optical systems	laser radar imaging system
thermal blooming		

	1
Optics Research	1973
	Issued 31 October 1973

Lincoln Laboratory

MASSACHUSETTS INSTITUTE OF TECHNOLOGY

LEXINGTON, MASSACHUSETTS

1a.

ABSTRACT

This report covers work of the Optics Division at Lincoln Laboratory for the period 1 January through 30 June 1973. The topics covered are laser technology and propagation, and optical measurements and instrumentation.

Additional information on the optics program may be found in the semiannual technical summary reports to the Advanced Research Projects Agency.

CONTENTS

INTRODUCTION

I. LASER TECHNOLOGY AND PROPAGATION

Laboratory experiments to study CW thermal blooming are under way and some preliminary results are reported.

Calculations indicate that thermal blooming due to the internal focus of a laser radar has little effect on the intensity distribution or wavefront shape in the far field, but can give rise to a significant chirp.

Observation of anomalous laser-supported detonation-wave velocity variations with power density suggests evidence for pulsed thermal blooming. Calculations confirm that the observations are consistent with the effects of thermal blooming.

Preliminary observations of high-power CO_2 laser pulse transmission through fog are presented. The results include measurement of total energy transmission and observation of saturation phenomena in fog, leading to pulse shaping of the incident CO_2 laser pulse.

Measurements have been made of the thermal blooming of a focused, high-energy, pulsed 10.6-μm laser and the experimental data are now being analyzed.

The effects of particle size, beam size, and pulse length on the breakdown threshold for particle-induced laser breakdown as well as transmission of energy through such induced breakdowns have been investigated.

The particle-induced laser breakdown has been studied for particles of 0.5-mm to 4-mm diameters with a 10-J Febetron laser.

Particle-induced laser breakdown was studied for a range of laser spot sizes from 3 mm to 9 mm with the 500-J E-beam laser.

Results from continuing laser-surface interaction studies which utilize the Lincoln 500-J E-beam CO_2 laser are presented. Included are measurements of the impulse transferred to large targets, peak focal-spot pressure measurements in plexiglas, and pressure and impulse distributions outside the focal spot.

A first set of measurements has been made of the electron and neutral density distribution caused by focused 10.6-micron radiation on a quartz surface using two-wavelength interferometry.

Experimental results of the optical output pulses resulting from varying the ionizing E-beam pulses are presented for dual-pulse and long-pulse excitation for the 500-J E-beam laser.

An experimental study was performed on positive unstable confocal square resonators over a range of geometric out-coupling from 34 percent to 85 percent with large equivalent Fresnel numbers. Near diffraction-limited output was obtainable for all outcouplings.

Our 500-J E-beam ionized CO_2 laser is found to lase on a single P-transition in the $001 \rightarrow 100$ band each shot for single shots. However, under certain double-pulse conditions and when a CW laser on the 9.6-μm band is injected, multiple transitions in the 10.6-μm band are observed in the lasing.

Recent additions have been made to high-power laser beam diagnostic capabilities.

Progress has continued on the design and procurement of components for a dual 500-J system. Assembly of these components was started near the end of this reporting period and will continue into the next period.

Measurements have been made of the penetration depth of traces of tri-n-propyl-amine in an N_2 buffer, and an average cross section of 7.3×10^{-18} cm^2 has been determined.

Near UV absorption spectra for three possible photoionization seedant anilines are shown and a comparison made of their potential advantages relative to tripropylamine.

A theoretical analysis is presented of the conversion efficiency of UV photon energy to the infrared photon energy produced by lasing. Both one- and two-step photo-ionization processes are considered.

A large-aperture photoelectron pumped CO_2-N_2-He gain cell doped with tri-n-propylamine is being built to demonstrate the scalability of the technique.

CW CO_2 laser beats beyond 60 GHz have been measured with HgCdTe varactor-photodiodes. The laser line frequencies and vibrational-rotational constants of the $^{12}C^{18}O_2$, $^{13}C^{16}O_2$, and $^{13}C^{18}O_2$ isotopes were also determined from microwave counter measurements of the beat frequencies.

A short-pulse, E-beam pre-ionized laser was built that delivers 10 J in 1 to 2 μsec.

The feasibility of a non-chemical HF laser which uses vibrational energy transfer from electron beam excited H_2 is being studied.

Pre-ionization and coated electrodes are some of the techniques being employed in the effort to develop a large, fast SF_2-H_2 HF laser.

II. OPTICAL MEASUREMENTS AND INSTRUMENTATION

MTF measurements of the boundary layer in the wind tunnel at NASA-Ames were carried out with the shearing interferometer. The MTF data obtained were com-pared with the flight boundary-layer measurements made earlier on board the NKC-135 aircraft with the same equipment.

A system to monitor sulfur dioxide by differential absorption of tunable infrared radiation from a semiconductor diode laser was developed. In the final report of this program, data were shown concerning system linearity, sensitivity, the effects of various interferants, and across-the-stack measurements at a coal-burning power plant. A summary of this report is included. This work was sponsored by the Environmental Protection Agency and the National Science Foundation.

Integrated-path measurements of atmospheric pollutant gases over relatively large distances (~2 km) require precise knowledge of transparency of the atmosphere in regions where the gases have strong characteristic spectral lines. For the present program, we are considering the detection of NO, CO, O_3, and SO_2 by tunable diode lasers operating within the 3- to 5-μm atmospheric "window." We describe here the use of the best available data for atmospheric transmission in this region and selection of the most appropriate pollutant gas absorption lines for monitoring purposes. This work was sponsored by the Environmental Protection Agency and the National Science Foundation.

REPORTS ON OPTICS RESEARCH

1 January through 30 June 1973

PUBLISHED REPORTS

Journal Articles*

JA No.

4121   Dynamics and Energetics of the Explosive Vaporization of Fog Droplets by a 10.6-μm Laser Pulse   P. Kafalas J. Herrmann   Appl. Opt. <u>12</u>, 772 (April 1973).

4088   High-Energy Pulsed CO_2 Laser-Target Interactions in Air   J. E. Lowder D. E. Lencioni T. W. Hilton R. J. Hull   J. Appl. Phys. <u>44</u>, 2759 (June 1973).

4117 CO_2 Laser Pulse Shaping with Saturable Absorbers   H. Kleiman S. Marcus   J. Appl. Phys. <u>44</u>, 1646 (April 1973).

4188   The Effects of Dust on 10.6-μm Laser-Induced Air Breakdown   D. E. Lencioni   Appl. Phys. Letters <u>23</u>, 12 (July 1973).

4191   Thermal Blooming of Pulsed Laser Radiation   H. Kleiman R. W. O'Neil   Appl. Phys. Letters <u>23</u>, 43 (July 1973)

*　　*　　*　　*　　*

UNPUBLISHED REPORTS

Journal Articles

JA No.

4093   Optical "Seeing" Through the Atmosphere by Interferometric Techniques   D. Kelsall   Accepted by J. Optical Society of America

4147   Aerosol Clearing with a 10.6-μm Precursor Pulse   D. E. Lencioni J. E. Lowder   Submitted to IEEE J. Quantum Electron.

4176   A Rapid Interferometer Technique for MTF Measurements in the Visible or Infrared Region   D. Kelsall   Accepted by J. Appl. Phys.

4192   Variable Pulse-Length Electron Beam CO_2 Laser   S. Marcus H. Kleiman R. W. O'Neill L. C. Pettingill   Accepted by J. Appl. Phys.

---

* Reprints available.

---

[*] Titles of Meeting Speeches are listed for information only. No copies are available for distribution.

---

[*] Author not at Lincoln Laboratory.

ORGANIZATION

OPTICS DIVISION

R. H. Rediker, *Head*
L. B. Anderson, *Associate Head*
M. J. Hudson, *Assistant*

LASER TECHNOLOGY

S. Edelberg, *Leader*
L. C. Marquet, *Associate Leader*

Bradley, L. C.
Brennan, M. J.
Bushee, J. F., Jr.
Ferdinand, A. P., Jr.
Fouche, D. G.
Granek, H.
Herrmann, J.
Johnson, J. Q.
Knfalas, P.

Kilcline, C. W.
Kleiman, H.
Lencioni, D. E.
Levine, J. S.
Lowder, J. E.
Marcus, S.
Morency, A. J.
O'Neil, R. W.
Osgood, R. M.

Pettingill, L. C.
Pike, H. A.
Pirroni, J. S.
Pitts, R. F.
Shey, S. Y.
Theriaoh, J. R.
Valcourt, G. L.
Weir, D. G.

ADVANCED SENSORS

J. O. Dimmock, *Leader*
E. S. Cottom, *Associate Leader*
T. M. Quist, *Assistant Leader*

Ariel, E. D.
Baukus, J. P.
Bielinski, J. W.
Bollman, R. A.
Dickey, D. H.
Ellis, R. H.
Fulton, M. J.
Hinkley, E. D.
Kelsall, D.

Keyes, R. J.
Marshall, A. P.
Merrill, E. R.
Mudget, D. A.
Nork, L. P.
Page, D. A.
Perry, F. H.
Sample, J. O.

Rotstein, J.
Scouler, W. J.
Sullivan, F. M.
Swedberg, J. L.
Thomas, M. A.
Wainwright, E. S.
Ziegler, H. L.
Zwicker, H. R.

OPTO-RADAR SYSTEMS

A. B. Gschwendtner, *Leader*
P. R. Longaker, *Assistant Leader*

Bauer, J. R.
Bakjps, R. R.
Brownson, J. S.
Bryant, B. W.
Clay, W. G.

Coles, R. M.
DiMarzio, E. W.
Dyjak, C. P.
Edwards, D. M.
Garavano, L. A.

Hull, R. J.
Johns, T. W.
McPhie, J. M.
Stevens, R. R.
Zieman, H. E.

LASER SYSTEMS

R. H. Kingston, *Leader*
L. J. Sullivan, *Associate Leader*

Bates, D. H.
Bicknell, W. E.
Capes, R. N., Jr.
Chanlk, L. W.
Daley, J. A., Jr.
Finsconara, J. G.

Freed, C.
Gilmartin, T. J.
Holtz, J. Z.
Huang, T. S.
Malling, L. R.
Marapoti, J. V.

O'Donnell, R. G.
Parker, A. C.
Swezey, L. W.,
Teoste, R.
Zimmerman, M. D.

1. LASER TECHNOLOGY AND PROPAGATION

A. LABORATORY EXPERIMENTS FOR SIMULATION OF CW PROPAGATION

An experiment to study thermal blooming on a laboratory scale has been planned and some preliminary results obtained. The purposes of the laboratory study are to test theoretically predicted scaling laws and to verify that thermal blooming can be reduced by adding initial phase corrections to a laser beam.[1]

An argon ion laser was chosen for this experiment because of the convenience of measuring and altering phase fronts in the visible region and because of the presence of suitable absorption lines in nitrogen dioxide. One or two sets of cylindrical lenses are used to introduce the desired phase corrections which include coma, astigmatism, and higher order aberrations. The ability of these elements to simulate the predicted optimum phase correction is discussed below.
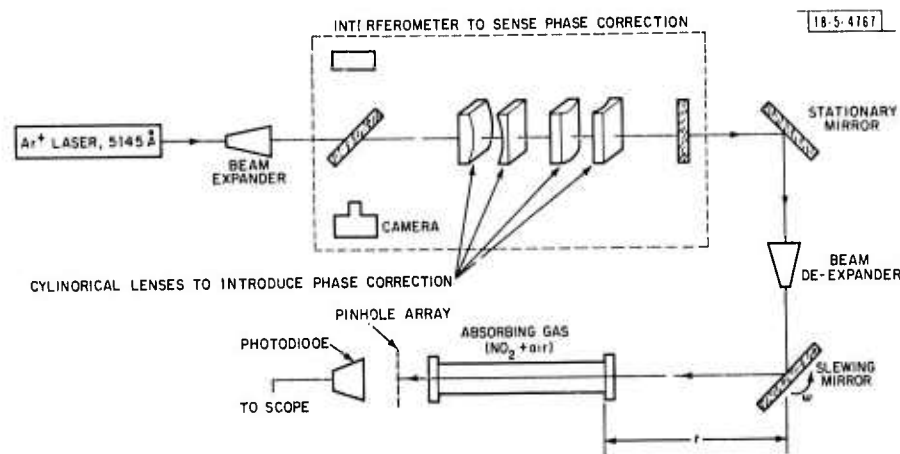
Fig. 1-1. Schematic of the experimental setup to study thermal blooming.

The experimental arrangement is shown in Fig. 1-1. The laser beam is expanded and collimated and enters an interferometer containing the phase-correction elements. The interferometer uses only a small percentage of the laser power but allows observation of a phase difference which is double that added to the transmitted beam. Following the interferometer and phase-correcting elements, the beam is contracted and strikes a rotating mirror which slews the beam through a cell containing a few torr of NO_2 mixed with air at atmospheric pressure. At the exit of this cell, the beam comes to a focus on a linear array of pinholes, which is followed by a single phototube. Because the line containing the pinholes is set at a small angle to the direction of slew, the envelope of the spikes at the phototube output gives a measure of the profile of the beam perpendicular to the direction of slew. The shape of an individual spike indicates the profile parallel to the slew direction.

As noted in Ref. 1, four dimensionless parameters are needed for scaling the thermal blooming phenomenon — the distortion number N_D, the slewing number N_ω, the Fresnel number N_F, and the absorption number N_A — and a parametric study has been undertaken first in these laboratory experiments.
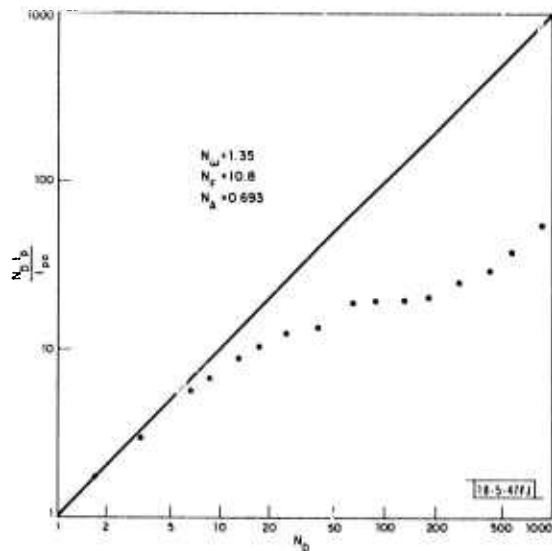
Fig. I-2. Log-log plot of $N_D I_P/I_{Po}$ vs N_D when the laser beam was slewed horizontally through the absorbing gas. The solid curve, at an angle of 45°, would result in the absence of thermal blooming.

Fig. I-3. Theoretical plots of the normalized peak irradiance as a function of Distortion Number, N_D (from Ref. 1).
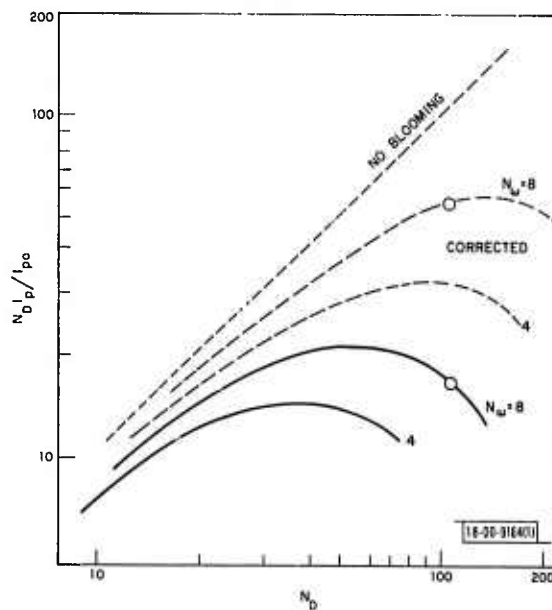
The distortion number gives a measure of the severity of thermal blooming and is defined as

$$N_D = \frac{\alpha P}{\rho c_p v_o \epsilon_o} \frac{\partial \epsilon}{\partial T} \frac{kR}{a} \quad ,$$

where P is the beam power, R the range, α the absorption coefficient, a the initial beam radius, k the propagation number $(2\pi/\lambda)$, v_o the cross-wind velocity, and $(1/\rho c_p \epsilon_o)(\partial \epsilon/\partial T)$ is a measure of the refractive index change with temperature. The slewing number is the ratio of the slew velocity at the focal region to the (constant) cross-wind velocity, $N_\omega = \omega R/v_o$, and in this experiment is determined by ratio of the cell length to the distance between the cell and the slewing mirror. The Fresnel number is $N_F = ka^2/R$ and the absorption number is defined as $N_A = \alpha R$.

Figure I-2 shows a typical result when the beam is slewed in a horizontal plane with the absorption cell sitting horizontally on a table. The ordinate is the normalized peak irradiance defined as $N_D I_P/I_{Po}$, where I_P is the peak irradiance and I_{Po} is the peak irradiance in the absence of thermal blooming. The abscissa is the distortion number. Figure I-2 should be compared to the predicted curve shapes of Fig. I-3. For low values of N_D, the curve of Fig. I-2 has the predicted shape, but for $N_D > 50$, the curve continues to rise rather than following the predicted downward trend.

The break at $N_D \approx 50$ can be explained by free convection, which was not included in the treatment of Ref. 1. Experimentally, N_D was varied by changing the rotation rate ω of the slewing mirror, which changes the velocity of the effective cross wind v_o ($= \omega r$, where r is defined in Fig. I-1). N_D is proportional to $1/v_o$. At low values of N_D, the beam is moving rapidly and traverses its diameter before free convection has a chance to start. At higher values of N_D, free convection does set in before the beam has swept through the heated area. This extra "wind," due to gravity-induced convection, reduces the amount of thermal blooming which would otherwise occur. The conclusion that free convection is present at lower slew rates is supported by the observation that the beam shifts downward (into the gravity wind) for these rates.

Because the initial experimental goal is to verify a theory that does not include free convection, an effort was made to eliminate the effect of free convection. To overcome the convection problem, the absorption cell was mounted vertically. In this configuration, the gravity wind will affect density gradients along the propagation direction only, and gradients in this direction do not significantly affect thermal blooming. Some of the preliminary results with this arrangement are shown in Fig. I-4. In all cases, the curves turn over and decrease as predicted. But, in common with the previous results, these curves eventually rise at approximately a 45° slope for large N_D. This increase occurs when conduction effects dominate free and forced convection as thermal loss mechanisms, i.e., when the beam diameter divided by the slew velocity is greater than the conduction time. For slew rates slower than this, blooming is conduction-dominated. The irradiance in this regime is constant, resulting in a positive 45° slope in the $N_D I_P/I_{Po}$ vs N_D curve.

Both theory and visual observation verify that heat conduction reaches a steady state at about the break points of the curves in Fig. I-4. Bissonnette[2] gives the time required for conduction to balance the energy input due to the absorption of radiation as $t_d = (\rho c_p a^2)/k$, where ρ, c_p, and k are the density, specific heat, and thermal conductivity of the gas, respectively, and a is the radius of the beam. The term t_d was calculated for the conditions of Fig. I-4 and is indicated at the point when the laser beam traversed its radius in t_d seconds. In all cases, t_d is close to the break point, showing agreement between the experiment and theory. Furthermore, when a
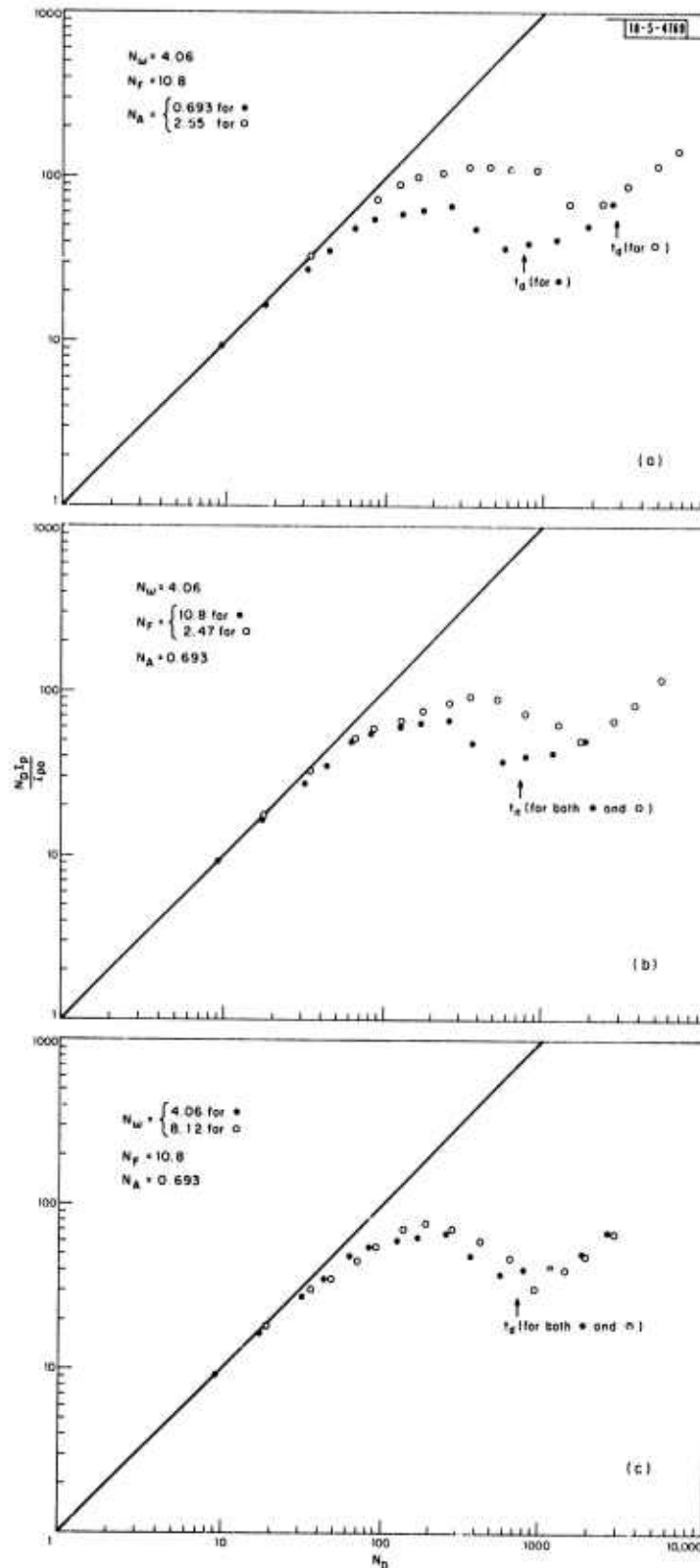
Fig. I-4. Log-log plots of $N_D I_P/I_{Po}$ vs N_D when the laser beam was slewed vertically through the absorbing gas: (a) only the absorption number N_A differs in the two curves; (b) only the Fresnel number N_F differs; (c) only the slewing number N_ω differs.

4

stationary beam was passed through the gas cell, the beam on the exit window was observed to increase from a small, focused spot to a large, bloomed circle in a time almost too quick for the eye to discern. The time was estimated to be of the order of 10^{-1} second. The calculated time t_d was 0.07 second. The break points in Fig. 1-4 thus occur near the times when conduction was observed to reach a steady state.

The curves in Fig. I-4 are arranged so that the results of changing one experimental parameter at a time can be compared. In Fig. 1-4(a), only the absorption number $N_A = \alpha R$ is different for the two curves. It was increased by a factor of $2.55/0.693 = 3.68$ by increasing α. For $\alpha R \ll 1$, the data should fall on one curve according to Ref. 1, which neglects linear depletion of the beam power. Since this is not the case in these examples, the higher absorption number shows less relative thermal blooming due to linear loss of beam power before it reaches the far-field region.

In Fig. I-4(b), only the Fresnel number $N_F = ka^2/R$ is different for the two curves. It was decreased by decreasing the radius of the beam by a factor of $0.0578/0.121 = 0.478$. Since for low Fresnel numbers thermal blooming is relatively less important near the far field as compared with the geometric limit, the total thermal blooming is less for the low Fresnel number, causing its curve in the plot of $N_D I_P/I_{Po}$ vs N_D to be shifted up and to the right.

In Fig. I-4(c), only $N_\omega = \omega R/v_o$ is different for the two curves. It was increased a factor of $8.12/4.06 = 2.00$ by decreasing the cross-wind velocity v_o. The curve for larger slew number shows the expected shift up to the right as seen in Fig. I-2, but with some scatter among data points. It should be emphasized that the results obtained thus far are preliminary. More extensive and careful studies will be undertaken.

In the next phase of the laboratory experiments, attempts will be made to decrease thermal blooming by adding appropriate phase profiles across the laser beam. The phase profile will be added by a system of lenses with matched curvatures. Initially, these lenses will be placed together to act as a parallel plate thus adding no optical path difference to the beam. The experimental parameters will be adjusted so that this uncorrected beam undergoes significant thermal blooming. Then the lenses will be separated, decentered, and tilted in order to add a phase field across the beam. If the correct phase is added, the beam should undergo less blooming.

The phase profile of Fig. I-5 was computed by the propagation code of Herrmann and Bradley[1] as that which would give a maximum decrease in thermal blooming for a typical set of experimental parameters. The main feature of this phase plot is a saddle point. The most direct way of obtaining a saddle point is to use cylindrical lenses in combination with refocusing. The beam de-expander of Fig. I-1 can compensate for any refocusing, which is an addition of a term equal to a constant times r^2 to the phase, where r is the distance from the center of the beam. Therefore, cylindrical lenses were chosen as the phase-correcting elements.

A plano-convex and a plano-concave cylindrical lens are planned for use. The two curved surfaces both have a radius of curvature of 14 cm so that they can be placed together to act as a flat plate. By separating the lenses (with no tilt or decentering), phase profiles which are nearly parabolas result, as shown in Fig. I-6.* The width of the parabola is approximately inversely proportional to the distance separating the lenses, and this distance can be adjusted to give the best fit to the desired phase profile. The parabolic optical path difference is characteristic of astigmatism.

---

*All optical path differences were calculated by computer using the ACCOS 5 program of Scientific Calculations, Incorporated.
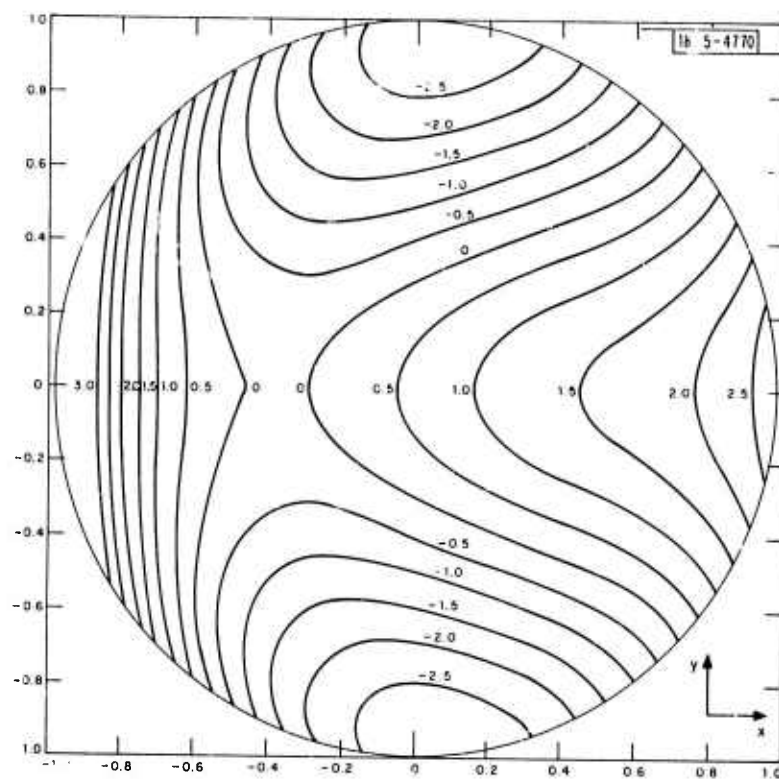
Fig. I-5.   Phase profile which will give maximum decrease in the thermal blooming for a typical set of experimental parameters.   The contour lines are separated by 0.5 radians.
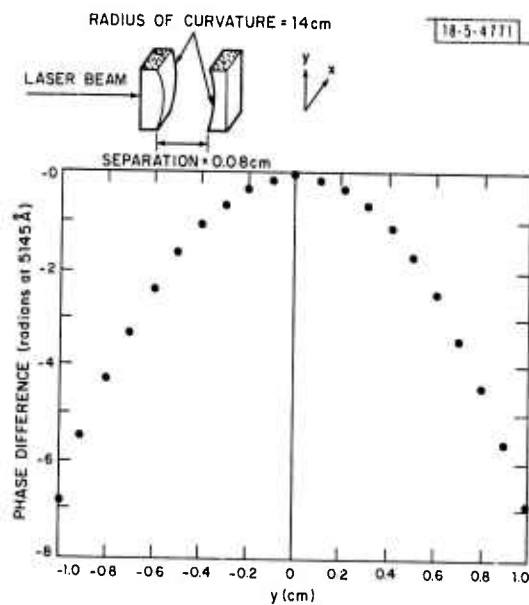
Fig. I-6.   Phase difference as a function of off-axis distance for a pair of separated cylindrical lenses.
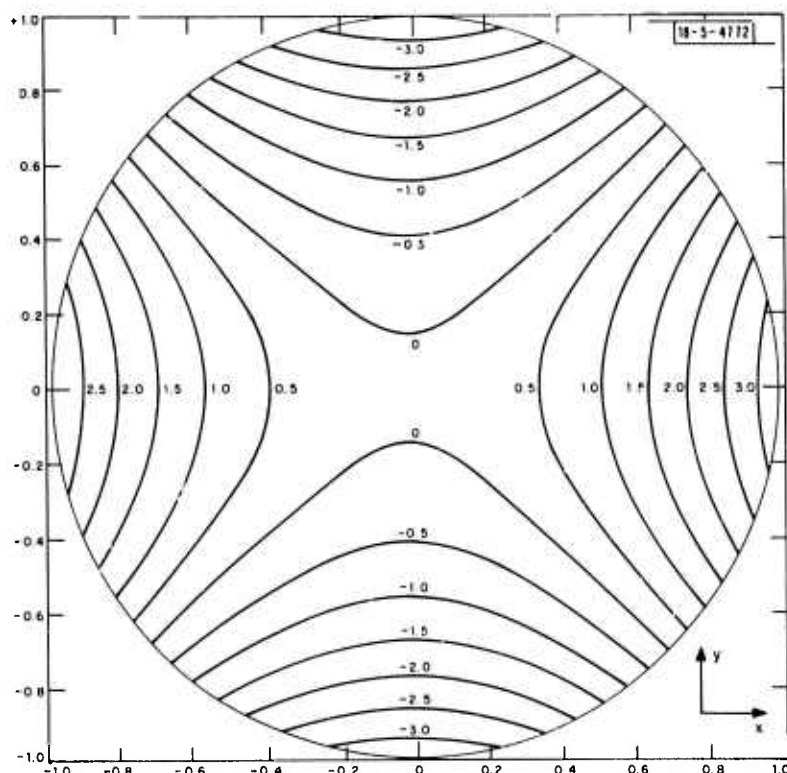
Fig. I-7. Phase plot of Fig. I-6 after $[3.200(x^2 + y^2) + 0.14986x + 0.800]$ radians have been added to it. The contour lines are separated by 0.5 radian.

Figure I-7 shows the phase profile of Fig. I-6 after a phase of $[3.200(x^2 + y^2) + 0.14986x + 0.0800]$ radians has been added to it. The first term represents refocusing, which will be accomplished by the beam expander. The second term is tilt and the third is just a constant optical path addition. Neither of these last two terms has any consequence to the experiment.

The difference between the desired contour (Fig. I-5) and that given by the two cylindrical lenses (Fig. I-7) is given in Fig. I-8. The integrated root-mean-square error of Fig. I-8 is 0.578 radian, when weighted by the Gaussian intensity distribution of the laser beam. This is less than $\lambda/10$ and will probably be less than the error added by the various optics in the experimental setup. It may, nonetheless, be advantageous to achieve a better fit to the desired contour. The difference shown in Fig. I-8 along the x-axis can be partly cancelled by using a second pair of cylindrical lenses.

The second pair of cylindrical lenses will be identical to the first; however, their axes will be rotated 90° with respect to those of the first pair (see Fig. I-9). Figure I-10 shows an example of the phase field added to the beam by first separating the lenses and then decentering one along the x-axis. The slope of the dotted, straight line is nearly linear with the amount of decentering and nearly independent of the separation. On the other hand, the amount of downturn (i.e., deviation from the straight line) is nearly linear with the separation and nearly independent of the decentering. By decreasing the decentering sufficiently, the downturn becomes great enough that the situation in Fig. I-11 results. (As the decentering approaches 0, the phase profile will approach the type of parabola shown in Fig. I-6.) A phase profile such as in Fig. I-11 will partly

7
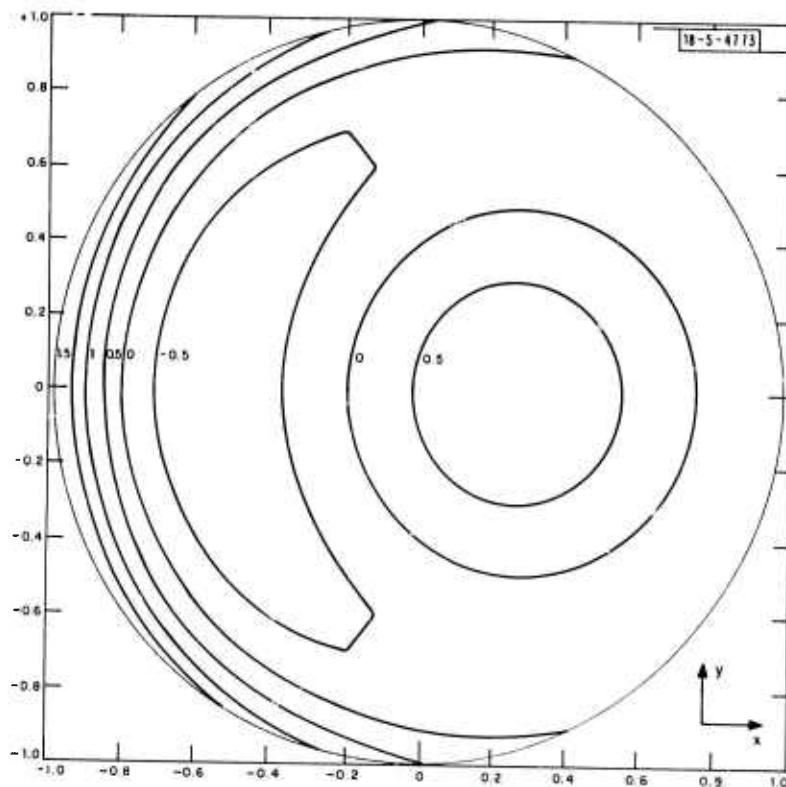
Fig. I-8. The difference between the computed contour (Fig. I-5) and the contour given by the two cylindrical lenses (Fig. I-7). The contour lines are separated by 0.5 radian.
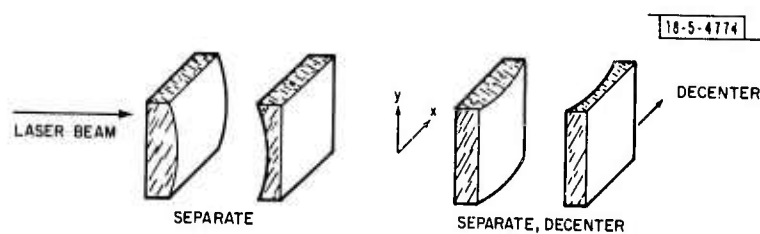
Fig. I-9. The four cylindrical lenses which will add phase corrections to the laser beam. Each curved surface has a radius of curvature equal to 14 cm.
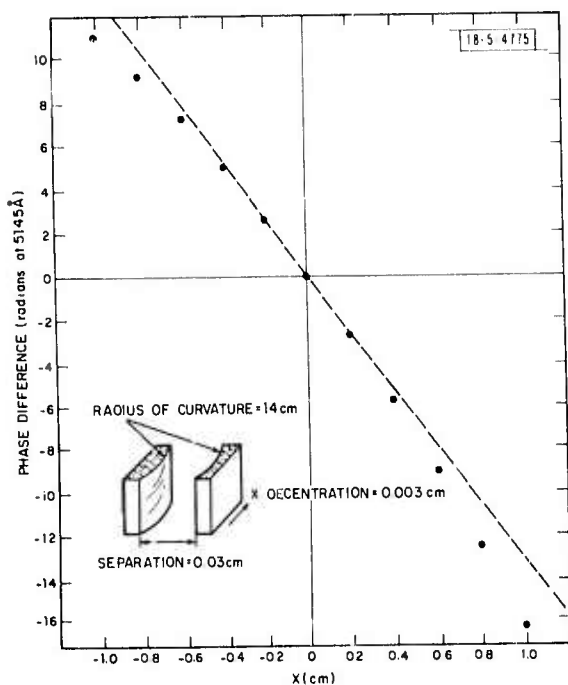
Fig. 1-10. Phase difference as a function of distance from the optical axis for a pair of cylindrical lenses, one of which is shifted off-axis from the other.
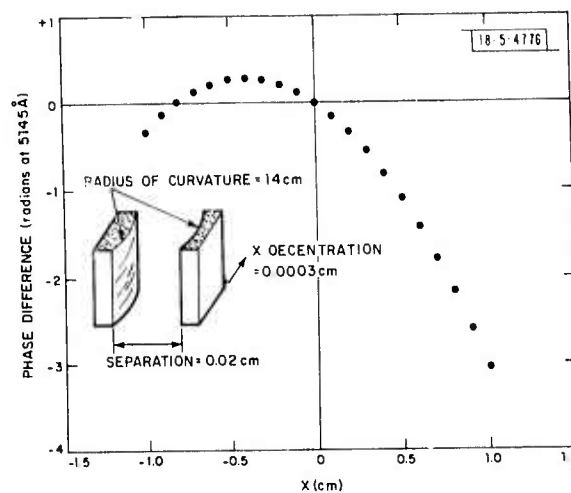
Fig. I-11. Phase difference as a function of off-axis distance when the decentering is small.

cancel out the difference in Fig. I-8. The separation and decentering can be varied to give the phase correction which minimizes the thermal blooming.

D. G. Fouche
H. A. Pike

B. PULSE PROPAGATION

1. Theoretical Calculations of the Influence of Thermal Blooming in Laser Radar

The laser radar has been designed with a beam which passes through a focus before reaching the final transmitter mirror, so that it can be chopped effectively. We have calculated the effect of thermal blooming, which takes place predominantly in the vicinity of the focus, on the transmitted beam for a model case.

For our model we have chosen a single pulse of an untruncated Gaussian spatial shape focused to a spot and allowed to expand again to its original size. The parameters chosen (energy — 1 kJ; pulse length — 1 msec; absorption coefficient — 10^{-6} cm^{-1}; initial and final $1/e^2$-power diameter — 8.5 cm; focused at 3 m; $\lambda = 10.6$ μm; unbloomed focal spot diameter — 0.47 mm) lead to appreciable blooming in the focus, as can be seen in Fig. I-12.

We now propagate the beam a distance of 3 m beyond the focus. In this plane the striking feature is that the irradiance is nearly unaffected by the strong thermal blooming in the focal area. Figure I-13 shows the irradiance in this plane at the beginning and the end of the pulse. The main effect here is the buildup of a phase distortion, also shown in Fig. I-13. There is also a change of absolute phase ("chirp") with time, as shown in Fig. I-14. The phase distortion is small enough to be acceptable; the chirp may be significant for some applications.

J. Herrmann
L. C. Bradley
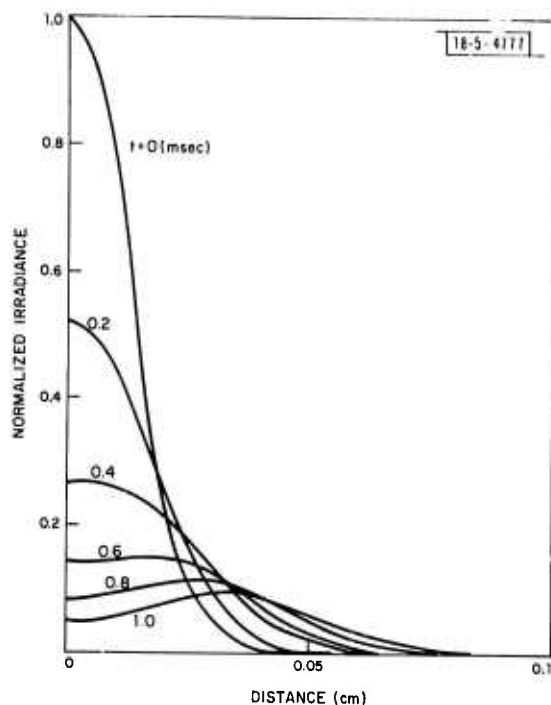
Fig. I-12. Normalized irradiance in the focal plane as a function of radial distance, at various times after initiation of the pulse.
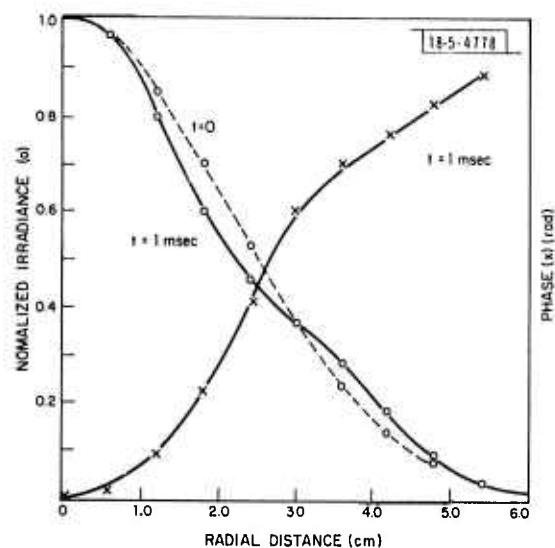
Fig. I-13. Normalized irradiance and phase 3 m beyond the focal plane, at the beginning and end of pulse, as a function of radial distance. The initial phase is zero for all radial distances.
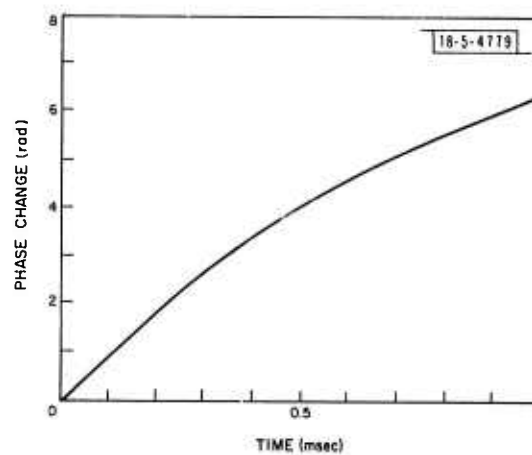
Fig. I-14. Phase change on axis 3 m beyond the focal plane, as a function of time.

2. Evidence of Pulsed Thermal Blooming at 10.6 μm

Previous work has shown that when a surface is irradiated with a high-power pulsed CO_2 laser a plasma is formed which propagates back along the laser beam in the form of a laser-supported detonation wave.[3,4] Raizer[3] has shown that the LSD wave velocity is given by

$$v = \left[\frac{2(\gamma^2 - 1)}{\rho_0} q \right]^{1/3} , \qquad (1\text{-}1)$$

where q is the incident power density, γ is the ratio of specific heats, ρ_0 is the ambient atmospheric density, and v is the velocity.

Observations of the plasma front expansion with a high-speed framing camera (2×10^6 frames/sec) during a 15-μsec E-beam CO_2 laser pulse have shown that the plasma front velocity decreases rapidly while the incident power density remains relatively constant. A possible explantion of these observations is that the on-axis power density is decreased during the laser pulse by thermal blooming. Thermal blooming calculations were carried out for a Gaussian beam focused with a 25-m mirror in the short-pulse approximation.[5] The results are shown in Fig. I-15 as a function of the scaling parameter $(\alpha P)^{1/3} t$, where α is the 10.6-μm coefficient (cm^{-1}), P is the power (W), and t is the time (μsec). For example, with $\alpha = 10^{-6}$ cm^{-1}, E = 300 J, t_p = 15 μsec we get $t_{1/2}$ = 6 μsec for the time at which the on-axis power density drops to one-half its initial value.
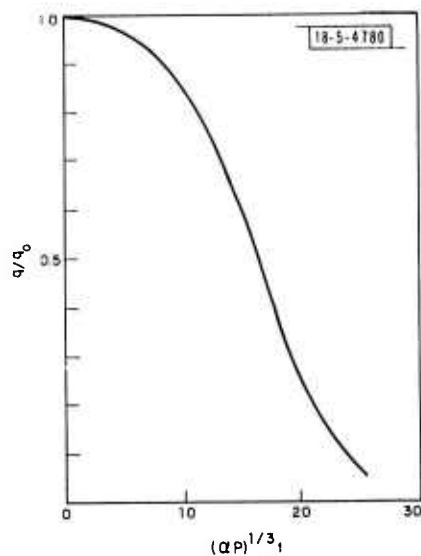
Fig. I-15. Plot of the ratio of the thermally bloomed on-axis power density to unbloomed power density as a function of the scaling parameter $(\alpha P)^{1/3} t$. Here α (cm^{-1}) is the absorption coefficient, P(W) is the total power, and t (μsec) is the time.

A plot of plasma front velocity as a function of incident power density for two shots is shown in Fig. I-16. The open symbols denote incident power densities in the absence of thermal blooming. These power density histories are plotted in Figs. I-17 and I-18.

The solid symbols denote on-axis power densities which have been corrected for thermal blooming with the use of the curve given in Fig. I-15. The time scales refer to elapsed time from the beginning of the laser pulse for the corrected power densities only (i.e., solid symbols). The thermal blooming corrections were applied for an absorption coefficient of 10^{-6} cm^{-1} at 10.6 μm which under ambient conditions corresponds to water vapor absorption at 48 percent relative humidity.[6] The solid line in Fig. I-16 is the theoretical prediction, Eq. (I-1), for $\gamma = 1.2$. These
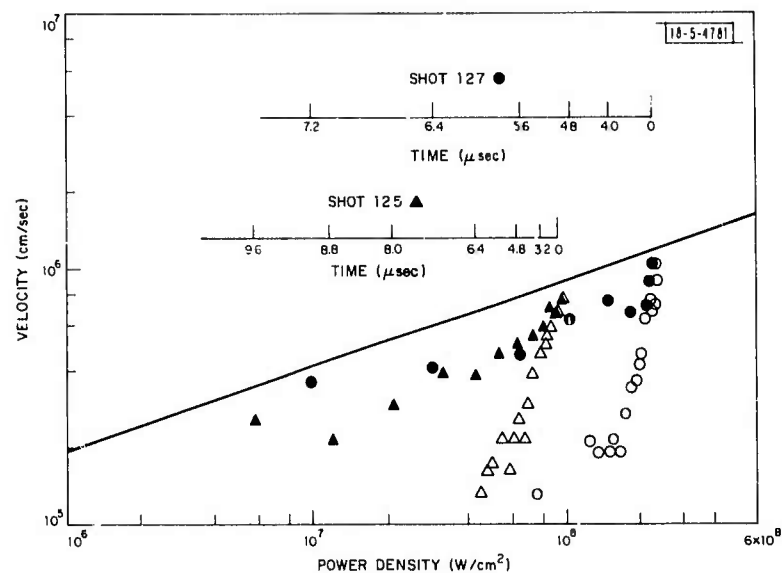
Fig. 1-16.   Plot of plasma front velocity as a function of incident power density for two shots.   The open symbols refer to uncorrected power densities and the solid symbols refer to power densities corrected for thermal blooming.   The time scales refer to the corrected power densities only.   The solid line is the theoretical prediction[1] obtained from Eq. (I-1) for ambient air and $\gamma = 1.2$.
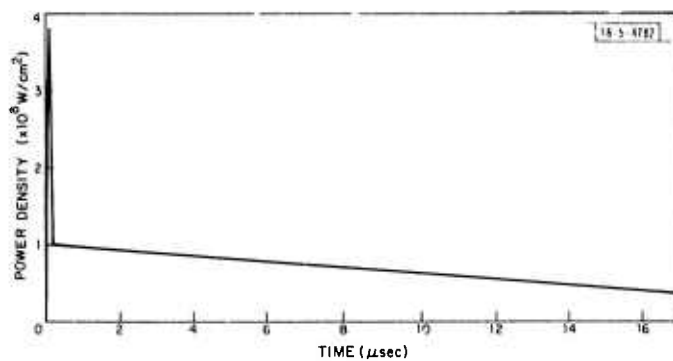
Fig. I-17.   Uncorrected power density history for shot 125.   The total energy in this shot was 206 J.

12
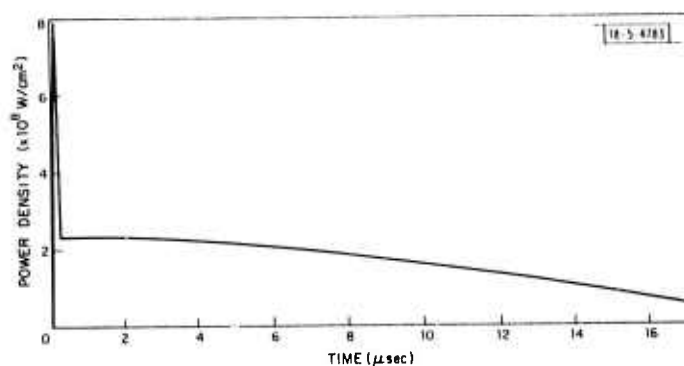
Fig. I-18. Uncorrected power density history for shot 127. The total energy in this shot was 365 J.

data indicate that if the incident power density is corrected for the effect of thermal blooming the resulting variations of velocity with power density are close to the theoretical $1/3$-power law. Recent pulsed thermal blooming experiments performed with the Lincoln E-beam CO_2 laser suggest another possible cause for these observations. Preliminary indications are that the laser itself may cause blooming due to degradation of the lasing medium with time. These experiments will be analyzed and reported in a future publication.

<div align="right">
J. E. Lowder
J. Herrmann
L. C. Bradley
</div>

3. CO_2 Laser Pulse Transmission Through Fog

Some preliminary observations of high-power CO_2 laser pulse transmission through fog are presented. The Lincoln E-beam CO_2 laser was used for these experiments.

The experimental arrangement is outlined in Fig. I-19. The fog chamber was placed 1.85 m beyond the focus of the 25-m mirror so that the beam was diverging as it passed through the fog. The incident and transmitted power and energy were measured on each shot with photon drag and pyroelectric barium titanate detectors placed in various orders of the linear transmission diffraction gratings. From geometrical optics the beam area was found to vary from 1.6 cm^2 at the entrance to 8.6 cm^2 at the exit of the fog chamber. Burn patterns at these locations indicated these areas were approximately correct and that the beam profile consisted of a number of hot spots. As an approximation we have taken the beam area to be 5 cm^2 and uniformly illuminated. A uniform fog was generated in the 2.5-m-long chamber with ultrasonic transducers and a number of small fans. The fog was characterized for each shot by probing through 30 cm of the chamber with a low-power CO_2 laser and a visible HeNe laser. The measured 10.6-μm extinction coefficient characterized the approximate water content of the fog irrespective of the predominate particle size and the 0.63-μm extinction coefficient served to determine the equivalent particle size.[7] The fogs generated varied in water content from 1 to 20 g/m^3 and the mean particle diameter varied from 3 to 5 μm, respectively.

The percent transmission of incident energy is shown in Fig. I-20 as a function of the ratio of incident energy to the energy required to vaporize all of the droplets in the beam. The incident energies ranged from 20 to 365 J and the corresponding average power densities ranged from 2×10^5 to 4×10^6 W/cm^2. The data show that the transmission increases rapidly when the incident energy is more than the energy required to vaporize the droplets in the beam. For
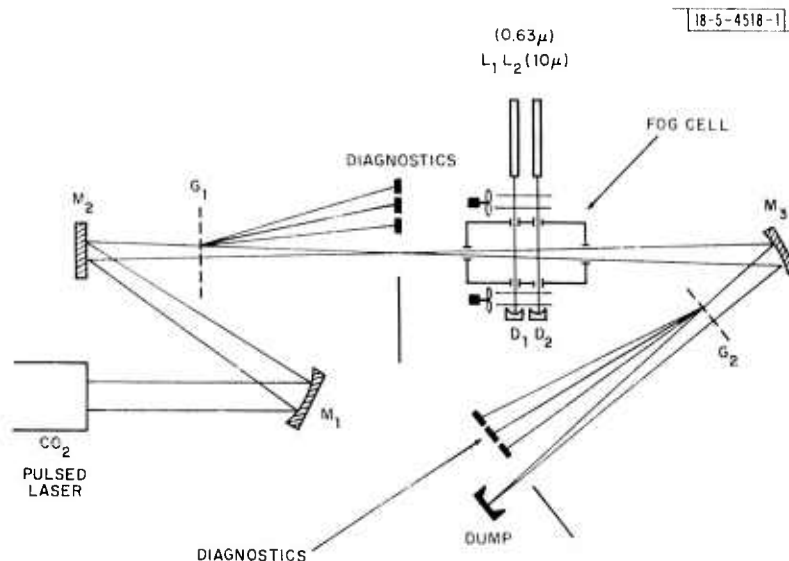
Fig. I-19. Experimental arrangement for CO_2 laser pulse transmission experiments. The laser beam was brought to a focus 1.85 m before the entrance to the fog chamber by a 25-m focal length mirror (M1) and the expanding beam was refocused with a 7-m focal length mirror (M3). G1 and G2 are linear transmission gratings for incident and transmitted energy and power measurements.

Fig. I-20. Percent transmission of incident energy as a function of the ratio of incident energy to the energy required to vaporize the fog droplets in the beam. The solid line is a theoretical prediction[2,3] for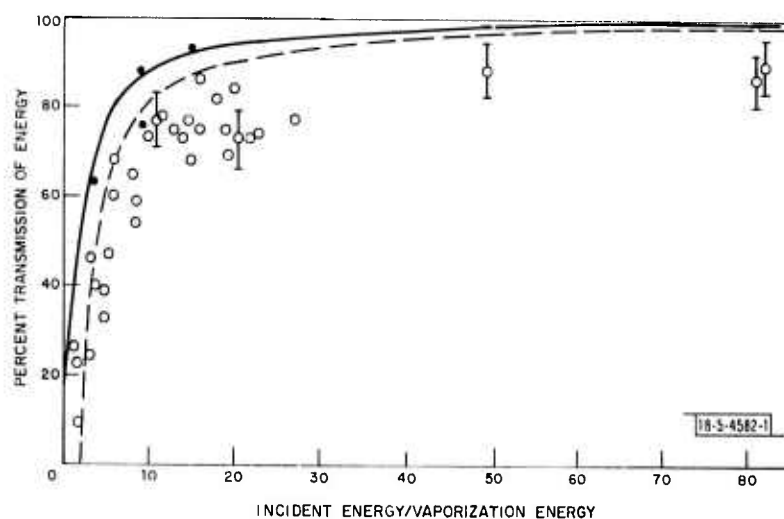 the fog level of most of the data (5 g/m³). The dashed line is a theoretical prediction for a very heavy fog of 400 g/m³.

14

comparison the solid line was calculated using the theory first given in Ref. 8 and developed in Ref. 9. The following expression from Ref. 9 was used,

$$E_t = E_o + \frac{A}{C_1} \ln \left\{ e^{-\tau_o} + (1 - e^{-\tau_o}) e^{-C_1(E_o/A)} \right\} \quad , \tag{I-2}$$

where E_t is the transmitted energy, E_o is the incident energy and A is the area of the beam. The constants C_1 and τ_o are determined by the particular fog and its mean particle size. The solid line refers to a fog with 5 g/m^3 and a mean particle diameter of 3 μm. Much of the data plotted in Fig. I-20 was taken with approximately this fog. The dashed line in Fig. I-20 refers to a heavy fog of 400 g/m^3 to show the insensitivity of the presentation in Fig. I-20 to the particular fog density. The open symbols denote fogs produced from distilled water and the solid symbols denote sea-water fogs. Most of the data falls somewhat below the theoretical prediction. This is probably due to a combination of the uneven energy distribution in the beam and hence uneven clearing and the fact that after traversing the fog chamber some of the energy may not have been captured by the calorimeters.

An interesting aspect of the fog transmission experiments was that the fog was found to behave as a saturable absorber and pulse shape the CO_2 laser pulse. This effect was predicted in Ref. 8 and recent work with other saturable absorbers is described in Ref. 10. Some examples of pulse shaping with fog are shown in Fig. I-21. The top trace in each photograph is the transmitted pulse and the bottom trace is the incident pulse. In Fig. I-21(a) there is little pulse shaping evident for an incident energy of 281 J and a 1 g/m^3 fog; moderate pulse shaping is shown in Fig. I-21(b) for an energy of 243 J and a 5.7 g/m^3 fog; and substantial pulse shaping is evident in Fig. I-21(c) for an energy of 171 J and a 6.1 g/m^3 fog.

The transmission through the sea-water fog seemed to be somewhat higher than through the distilled-water fog as shown in Fig. I-20. But breakdown in the sea-water fog occurred at much lower power densities than those required for distilled-water fogs. A breakdown occurring in sea-water fog is shown in Fig. I-22(b) along with the incident and transmitted laser pulses. On this shot 45 percent of the total energy was transmitted and in Fig. I-22(a) the last 12 μsec of the pulse show the effect of absorption in the breakdown plasma. A lower bound on the breakdown threshold was found to be an average power density of 3×10^6 W/cm^2 and a peak power density of 10^7 W/cm^2. This threshold was determined for a uniformly irradiated beam area of 5 cm^2. Due to the hot spots in the beam the actual threshold could be somewhat higher.

More recent experiments have been conducted in which the fog chamber was lengthened to 5 m and was placed in the focusing portion of the beam. With this configuration the saturation phenomena and time dependent blooming of the transmitted pulse were investigated. These data will be analyzed and reported in a future report.

J. E. Lowder
H. Kleiman
R. W. O'Neil

4. Pulsed Thermal Blooming Experiments

Experiments have been completed which measure thermal blooming of a focused high-energy 10.6-μm pulsed laser beam. The primary experiment was designed to examine blooming in the short-pulse time regime where the index of refraction (at constant power) varies with the cube of the pulse time. In the short-pulse regime, measurable blooming occurs in a time less than an acoustic transit time, τ_H, across a focal radius.
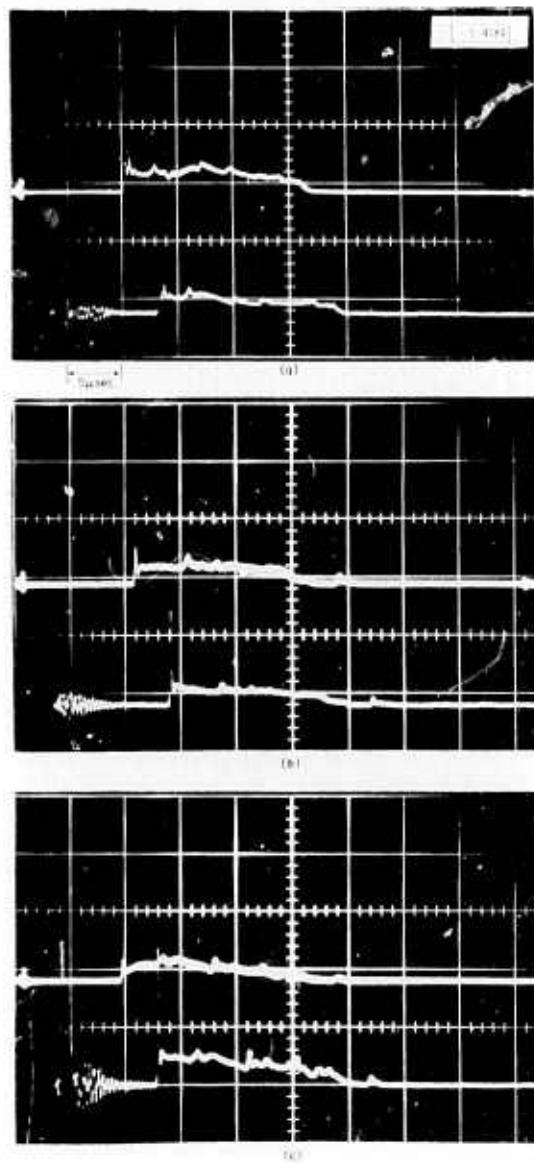
Fig. 1-21. Incident and transmitted CO_2 laser pulse shape for three different fog levels: (a) transmission for an incident energy of 281 J and a 1 g/m^3 fog; (b) transmission for an incident energy of 243 J and a 5.7 g/m^3 fog (c) transmission for an incident energy of 171 J and a 6.1 g/m^3 fog
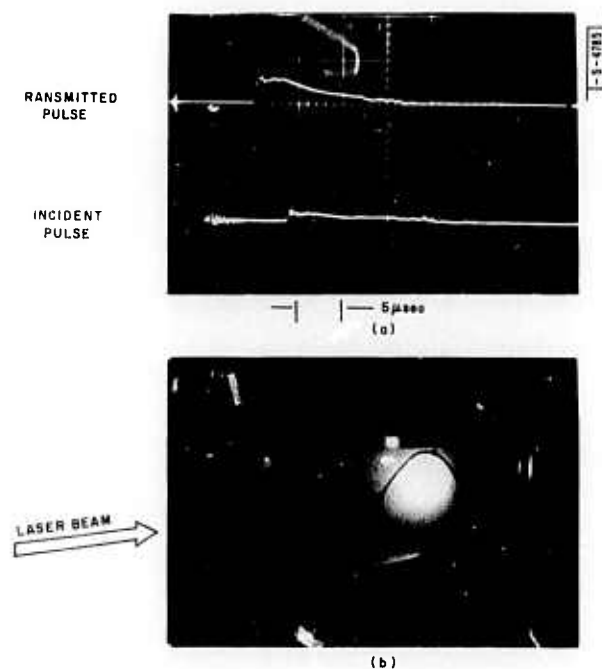
Fig. I-22. (a) Incident and transmitted CO_2 laser pulse shapes through a 5 g/m^3 fog generated with sea water. (b) Open-shutter photograph of breakdown in the fog chamber.

In the experimental setup illustrated in Fig. I-23 the 20- × 15-cm beam from the Lincoln Laboratory 500-J laser was focused with a 25-meter mirror through the center of a 45-cm-diameter, 10-meter-long environmental chamber. The radius of the central lobe of the focused beam from the 85-percent outcoupled unstable resonator was 1.5 mm for $\tau_H \approx 4$ μsec. Measurements were made with both broadband and resonant absorbing gas seedants in the "absorption section" of the chamber enclosing the beam in front of focus. Dry nitrogen at STP was used in the section beyond focus to eliminate blooming effects beyond the focal region. Mechanical shutters opened in synchronism with the laser firing, thus eliminating the need for chamber windows.

Diffraction grating sampling was used in the diagnosis of the unbloomed and bloomed focal patterns. The energy, power, and beam profile (from grating generated burn patterns) characteristic of the unbloomed beam were measured in diffraction orders separated from the converging beam before it entered the absorption section. To diagnose the bloomed beam, the focal distribution at the end of the absorption section was reimaged with a mirror placed after the non-absorbing section. A second grating sampled the imaging beam. In addition to the transmitted energy and power, the time-resolved irradiance and the time-integrated energy distribution were measured using techniques described in Sec. IV-A-4.

Specific experiments include:

(1) Thermal blooming due to a broadband, non-resonant absorption where energy and absorption coefficient, α, were varied. Both short- and long-pulse blooming conditions were studied.

(2) Thermal blooming in resonant absorbers (CO_2 and CO_2-Argon mixtures) where energy and α were varied.
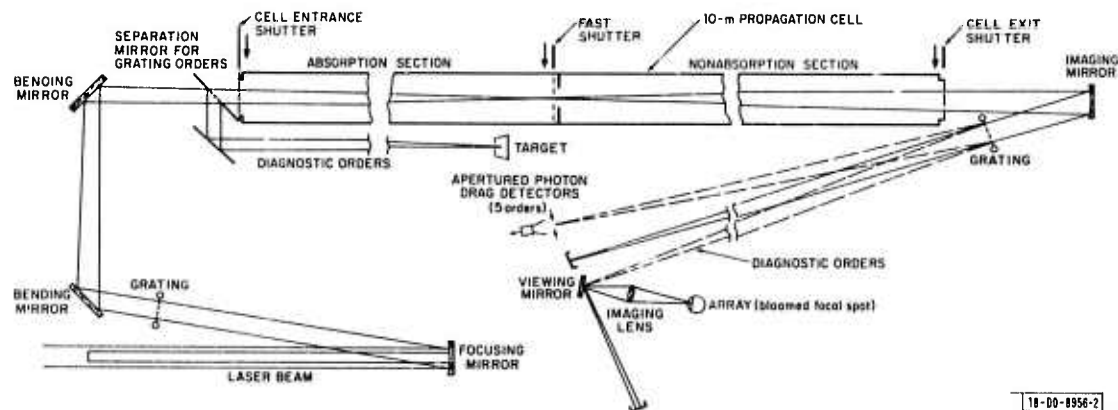
Fig. I-23. Schematic of experimental apparatus used in pulsed thermal blooming measurements.
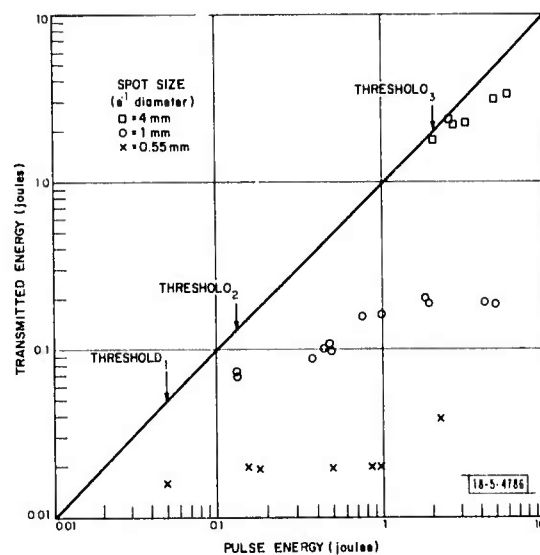
Fig. I-24. Energy transmitted through particle-induced breakdown for spot sizes 4 mm, 1 mm, and 0.55 mm. The qualitative features of these data are explained by the finite radial growth rate of the breakdowns.

(3) Saturation in resonant absorbers, where power density was varied.

(4) Thermal blooming in laboratory air, where energy was varied for measurements in the long-pulse regime.

(5) Temporal redistribution of the focal pattern in the absence of absorption (i.e., laser effects).

Data from these experiments are now being analyzed and will be summarized in the next report.

R. W. O'Neil
H. Kleiman
J. E. Lowder

5. Particle-Induced Breakdown Studies

During the past six months a series of experiments have been conducted to study the effects of particles on laser-induced breakdown in air. The effects of particle size, beam size, and pulse length on the breakdown threshold, and the transmission of energy through particle-induced breakdowns have been investigated.

a. Studies with a 10-J Febetron Laser

The effect of spot size on the particle-induced breakdown threshold and transmission of energy was studied with a 10-J per pulse Febetron laser operated in a short-pulse mode.[11] The pulse shape for this device was similar to a TEA laser with a 200-nsec spike followed by a 2-μsec tail. Peak powers of 10 MW were obtained. Single 50 μm carbon particles were placed in the focal volume by the technique described in Ref. 12. Three spot sizes were used with the following e^{-1} diameters: 4 mm, 1 mm, and 0.55 mm. The incident and transmitted energy and power were monitored with $BaTiO_3$ and photon drag detectors.

The energy transmitted through particle-triggered breakdowns is shown in Fig. I-24 as a function of incident energy for three different spot sizes. The solid line represents the transmitted energy when no breakdowns occur. The first significant feature of these data is that the energy at which breakdowns occur at a given spot size is a measure of the threshold intensity. Although the pulse shape varied somewhat from shot to shot the incident energy is roughly proportional to the peak laser power. The data in Fig. I-24 indicate that threshold intensity is approximately the same for these three spot sizes. Measurements of the threshold intensities, defined as that intensity for which breakdowns occur on 50 percent of the shots, are shown in Fig. I-25 for the three spot sizes. The other interesting features of the data in Fig. I-24 are the drop in transmitted energy when breakdowns occur near threshold and the change in transmitted energy through breakdowns for higher energies. Both of these features can be explained by the finite

Fig. I-25. Threshold intensity (breakdown on 50 percent of shots) as a function of spot size for 50-μm carbon particles.

19
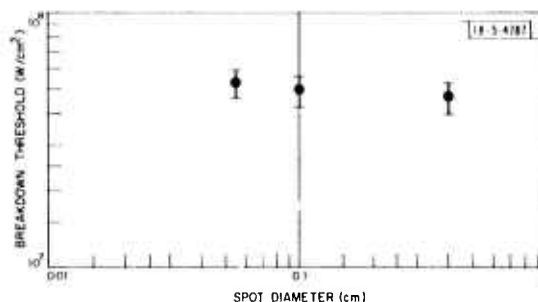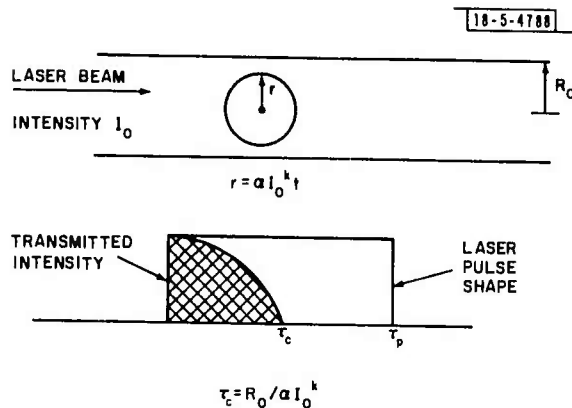
Fig. 1-26.   Model for transmitted energy through a radially growing breakdown.

radial growth rate of breakdown.   The simplified model given below will illustrate these effects. The basic assumptions are shown in Fig. 1-26.   We assume the breakdown grows radially with velocity $v_r = \alpha 1_o^k$, where 1_o is the beam intensity, and either absorbs or scatters all the radiation incident upon it.   Then for a beam radius R_o, and a rectangular pulse shape of pulse time τ_p the transmitted energy will be

$$E_t = \int_0^{\tau_c} [1_o \pi R_o^2 - 1_o \pi (\alpha 1_o^k t)^2] \, dt$$

where τ_c is the time required for the breakdown to fill the beam: $\tau_c = R_o / \alpha 1_o^k$.   This gives

$$E_t = \frac{2R_o 1_o^{-k} E_o}{3\alpha \tau_p} \qquad \text{for } \tau_c < \tau_p$$

$$E_t = E_o \left[1 - \frac{\alpha^2 1_o^{2k} \tau_p^2}{3R_o^2} \right] \quad \text{for } \tau_c > \tau_p \quad ,$$

where E_o is the total pulse energy.   This shows that when $\tau_c < \tau_p$ the fraction of energy transmitted at a given intensity should scale as the beam radius.   The data for beam sizes 1 and 0.55 mm for which $\tau_c < \tau_p$ do in fact scale in this way.   For the 4-mm data for which $\tau_c > \tau_p$ as determined from measurements of the transmitted power, the fraction of energy transmitted is correspondingly higher as indicated by this model.   This scaling was also verified by using a shorter pulse length at a given spot size.   From the slope of transmitted energy an intensity dependence of the radial growth rate of $v_r \propto 1^{0.7}$ is obtained.

More quantitative information can be extracted by using the actual pulse shape and a more realistic model for the plasma growth.   Experiments are also under way to measure directly the radial growth rates as a function of intensity.

D. E. Lencioni

b.   Studies with the 500-J E-Beam Laser

Experiments were conducted with the 500-J E-beam laser to determine the long-pulse threshold for several different particle sizes.   For these measurements pulse shaping[13] was used to either eliminate or reduce the initial spike on the laser pulse.

For a 3-mm spot size – diameter of the central null – the threshold was measured in a chamber filled with a known distribution of carbon dust.[14] The largest particle diameter expected in the beam was 6 μm. The threshold for 10-μsec pulses was found to be $\approx 2 \times 10^8$ W/cm^2 which was comparable to the 200-nsec threshold previously measured.[14]

For a 9-mm spot a similar measurement was made when the chamber was filled with 50-μm particles. Here the threshold was found to be $\approx 3 \times 10^7$ W/cm^2 comparable to previously reported measurements for 50-μm carbon particles[15] at pulse lengths ≈ 10 μsec and roughly a factor 2 below the 200-nsec threshold measurements.[14] This long-pulse large-particle threshold is almost a factor 10 higher than for fiber breakdown[16] and other large-particle experiments.[17]
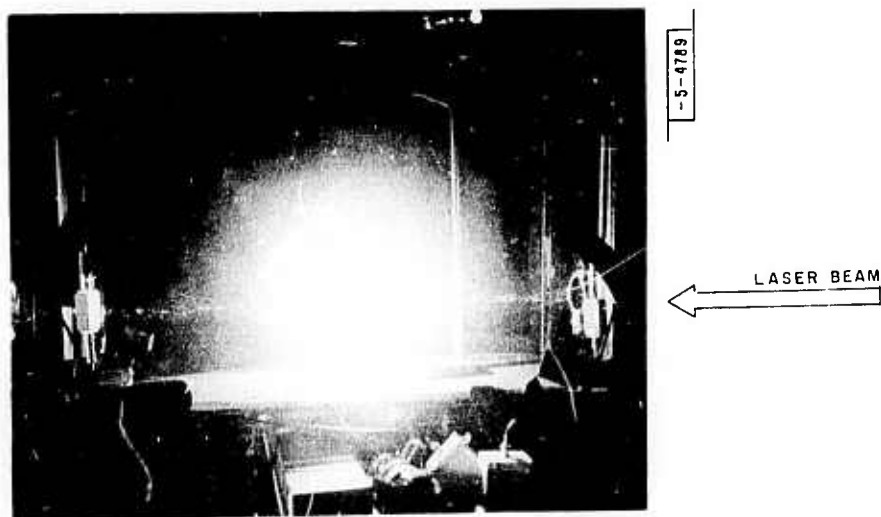
Fig. 1-27. Breakdown in dust chamber with 50-μm carbon particles. Laser pulse was 10 μsec with average intensity 3×10^7 W/cm2. Note jetting of carbon particles in the beam.

For the 50-μm carbon particle experiments pronounced jetting of particles was observed as discussed in Ref. 15. Figure 1-27 shows a photograph of the beam passing through the dust chamber in which breakdown did occur. Note the jetting of particles in the beam.

<div align="right">

D. E. Lencioni   J. E. Lowder
H. Kleiman   R. W. O'Neil

</div>

C. EFFECTS

1. Pulsed CO$_2$ Laser Surface Effects Experiments

Some results from the continuing laser – surface interaction studies which utilize the Lincoln 500-J E-beam CO$_2$ laser are presented. Included are measurements of the impulse transferred to metallic targets with areas much larger than the focal spot area, peak focal spot pressure measurements in Plexiglas, and pressure and impulse distributions.

The experimental setup is outlined in Fig. 1-28. The laser beam was first focused with a 25-m focal-length mirror and passed through a focus at table 1. Small glass fibers (100-μm diameter) were placed at focus 1 to cause a breakdown and effectively limit the laser pulse transmitted to table 2 to durations of 1 to 5 μsec. The radiation from focus 1 was collected by 7-m focal-length mirror and refocused at table 2. The plastic tube at table 1 was continuously flushed
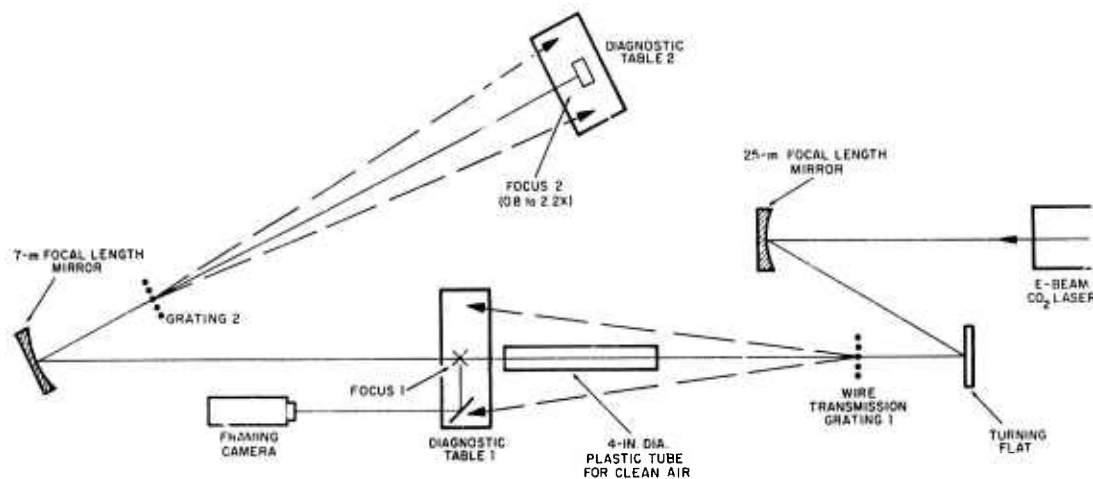
Fig. I-28.   Diagram of the experimental setup for the surface effects experiments.
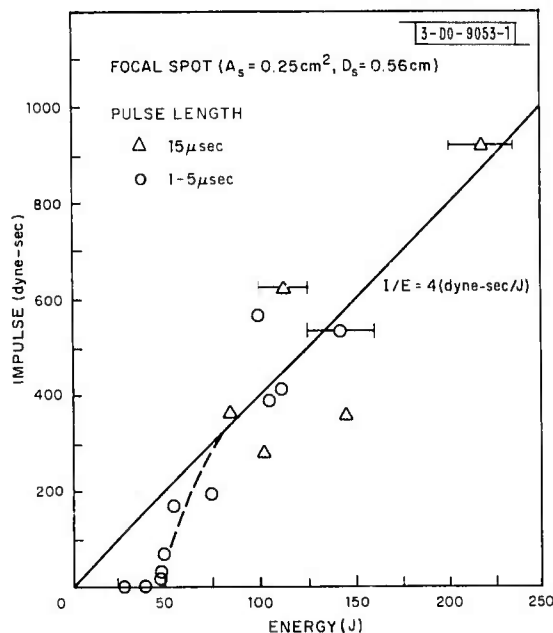
Fig. I-29. Total impulse transferred to a 10-cm-diameter aluminum target as a function of energy. The solid line denotes a coupling coefficient of 4 dyne-sec/J. The average power densities for these data ranged from 8×10^6 to 7×10^7 W/cm².
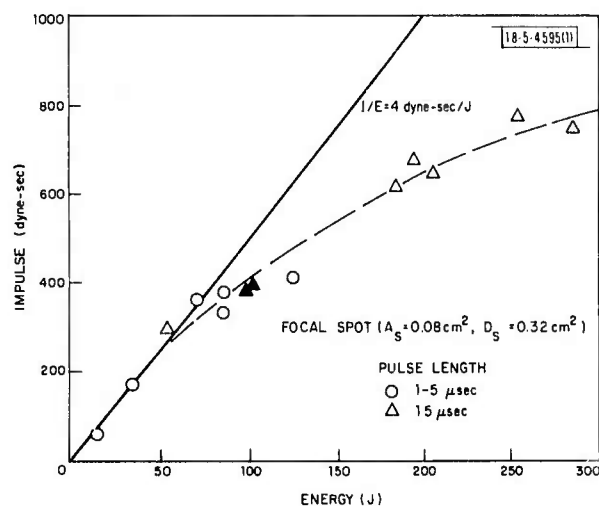
Fig. I-30. Total impulse transferred to a 10-cm-diameter aluminum target as a function of energy. The solid symbols denote copper and tin targets. The solid line denotes a coupling coefficient of 5 dyne-sec/J. The average power densities for these data ranged from 7×10^7 to 5×10^8 W/cm².

with clean air to prevent breakdowns triggered by dust in the air. The diagnostics were placed in diffraction grating orders to measure the power and total energy delivered to both tables. The focal spot size was determined from an analysis of burn patterns on thermally sensitive paper produced by from 3 to 6 diffracted grating orders.[18] The average power density was then determined from an analysis of the energy distribution in the focal spot diffraction pattern and the half-power area and is given by:

$$\bar{q} = \frac{0.5(E_o)}{A_{eq}\tau} \quad . \tag{1-3}$$

Here $\bar{q}$ is the average power density, E_o is the total energy, 0.5 is the fraction of the energy in the central spot, A_{eq} is the equivalent half-power area of the central spot, and τ is the laser pulse length. The instantaneous power density was determined by normalizing the area under photon drag detector pulse shape measurements by the energy contained in the central spot. The focal spot size quoted in the remainder of this note corresponds to the total area of the central spot in the focal plane diffraction pattern generated by the unstable resonator output aperture of the laser.

Previous work[19,20] has shown the impulse transferred to a surface due to irradiation by a high-power CO_2 laser pulse is due to the blast wave caused by a breakdown plasma in the atmosphere just above the target surface. The blast wave was shown to expand over the surface imparting momentum to the target until it decayed to a sonic disturbance. In this work targets 10 cm in diameter were used to measure the maximum possible momentum transfer to a surface.

The total impulse delivered to large targets was measured with a ballistic pendulum which was stabilized with a five-wire suspension system. The impulse was found from the mass of pendulum and the maximum amplitude of its swing. The displacement of the pendulum was measured with a photodiode — light source assembly in which the photodiode signal was proportional to the position of the pendulum. The pendulum and position sensor combination was calibrated both by measuring the period of the pendulum and also by impacting the pendulum with small bodies of known momentum. The impulse transferred to a 10-cm-diameter target as a function of total energy is shown in Fig. I-29. The focal spot diameter was approximately 0.56 cm. The various symbols refer to the laser pulse length and are identified in the figure. These data indicate the impulse is independent of pulse length for these conditions. The solid line indicates a coupling coefficient of 4 dyne-sec/J and the error bars give the maximum uncertainty in the energy measurements. There is a fair amount of scatter in the data which may have been due to variations in laser beam quality which affected the energy distribution in the focal spot. The average power densities range from 8×10^6 to 5×10^7 W/cm^2 for these data. The dashed line indicates a threshold for impulse transfer at about 50 J which corresponds to a power density of approximately 9×10^6 W/cm^2. Similar impulse data for a smaller focal spot size are presented in Fig. I-30. The average power densities for these data ranged from 7×10^7 to 5×10^8 W/cm^2. These data are consistent with a coupling coefficient of 5 dyne-sec/J for energies up to about 75 J. The dashed line shows the trend of the data for higher energies and indicates the point where the laser energy is being inefficiently delivered to the target due to propagation of the absorbing plasma about a target radius away from the target. The solid symbols denote copper and tin targets. From these impulse data we conclude that for a wide range of power densities total coupling coefficients on the order of 5 dyne-sec/J may be expected if the laser energy is deposited close to the target (i.e., within a target radius).

-5-4790

(a)

LASER BEAM →
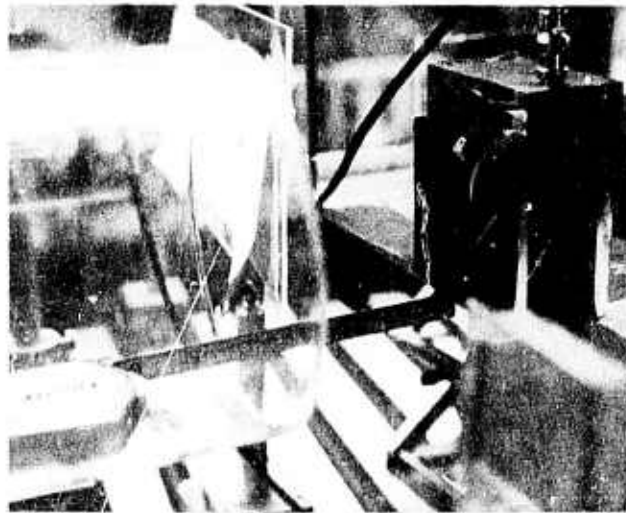
(b)

Fig. 1-31. (a) Photograph of the Plexiglas-carbon pressure gauge placed at the focus at Table 1-2. The clean air plastic tube is shown on the left. (b) Open-shutter photograph of a laser-supported detonation wave extending approximately 10 cm away from the pressure gauge.

Piezoresistive carbon pressure gauges developed by J. Charest[21] were used to measure the peak focal spot pressure on a Plexiglas target. The sensitive carbon element (~1.6 mm × 1.2 mm) is encapsulated in 1/2-mil sheets of Kapton and then bonded between a 0.6-cm-thick sheet of black Plexiglas and a 5-cm-thick piece of clear Plexiglas. The black Plexiglas was found necessary to shield the carbon element from radiant heating from the plasma formed at the front surface. The 50-Ω carbon gauge was operated with a DC current of between 20 and 30 mA and a 1000-Ω ballast resistor. The gauge assemblies were calibrated by subjecting them to the step pressure change of a reflected shock wave at the end wall of a small shock tube. The gauge calibrations ranged from 12 to 16 bar/mV and the gauges had rise times of about 100 nsec. A photograph of a gauge in position at table 2 is shown in Fig. I-31. Also shown in Fig. I-31 is an open-shutter photograph of a laser-supported detonation wave extending about 10 cm away from the gauge surface. The leading edge of a laser pulse and the gauge response are shown in Fig. I-32 for a shot in which the peak power density was 1.4×10^9 W/cm^2 and the peak pressure was 384 bar. The 200-nsec

(a)

Fig. I-32. (a) Leading edge of the incident 10.6-μm laser pulse (0.5 μsec/div.) measured with a photon drag detector. (b) Plexiglas-carbon pressure gauge response (0.5 μsec/div.) to the laser pulse shown in (a). The peak power density was 1.4×10^9 W/cm^2 and the peak pressure was 384 bar.

(b)
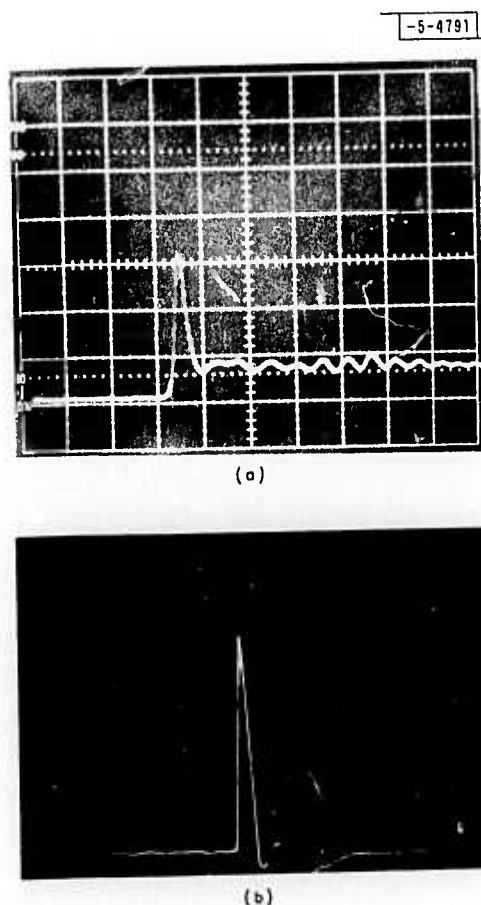
width of the pressure pulse is about the same as the leading edge spike of the laser pulse. The gauge response in Fig. I-32 shows a couple of small tension pulses after the initial pressure peak and then zero pressure. This response is due to unloading of the front Plexiglas surface and not the actual front surface pressure. A plot of the peak pressure as a function of the initial power density is shown in Fig. I-33. The variation of initial power density was obtained by pulse shaping using a controlled fog as a saturable absorber. This technique is discussed elsewhere in this
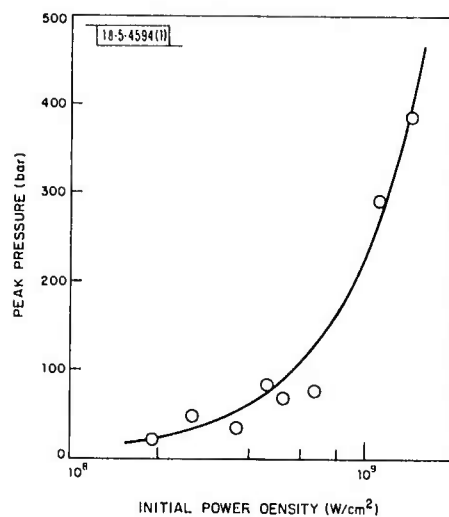
Fig. I-33. Peak pressure with a Plexiglas-carbon pressure gauge ($\tau \simeq 100$ nsec) as a function of initial power density. The solid line is a fit to the data and shows the peak pressure increases approximately as the 3/2 power of the initial power density.
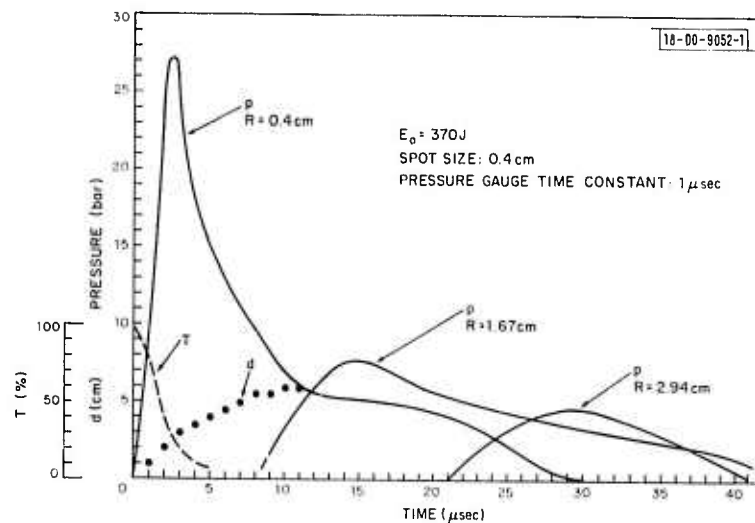
Fig. I-34. Pressure histories at three distances from the focal spot. Also shown are the distance (d) of the plasma front from the target and the percent transmission (T) of laser energy through a breakdown triggered by a glass fiber on a similar shot.

26

report (see Sec. I-B-3). The solid line shows the trend of the data and indicates the peak pressure increases roughly as the 3/2 power of the initial power density. For these measurements the diameter of the focal spot was approximately 0.32 cm. Since the gauge was located 0.6 cm from the surface and the focal spot size was small the pressure measurements reported are lower bounds on the actual surface pressure due to some spreading of the stress wave in two dimensions.

The surface pressure distribution on an aluminum plate due to the expanding blast wave was measured with three PCB/Piezotronics quartz pressure gauges spaced at 1.27-cm intervals radially away from the focal spot These gauges were frequency matched to damp out gauge resonances and had a response time of 1 μsec. Pressure histories for one shot are shown in Fig. I-34 where the first gauge was located just outside the focal spot. These measurements were taken at table 1 and the plasma expansion was photographed with the high-speed framing camera (10^6 frames/sec) shown in Fig. I-28. The distance (d) of the plasma front from the target as a function of time is shown in Fig. I-34. The percent transmission (T) through a breakdown plasma triggered by a glass fiber on a similar shot is also shown in Fig. I-34. The pressure histories measured on three shots were integrated to provide measurements of the specific impulse distribution over the target surface. These measurements are presented in Fig. I-35 and show that the specific impulse drops off rapidly with increasing radial distance from the focal spot.

Fig. I-35. Distribution of specific impulse with radial distance from the focal spot for three shots with different energies.
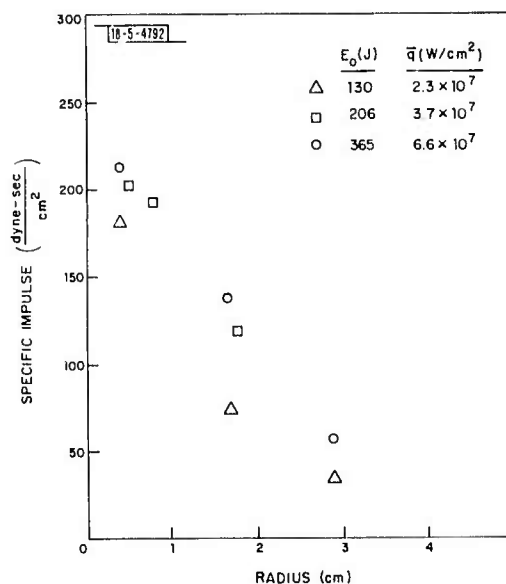
Other experiments which have been completed but not yet analyzed include peak pressure measurements in Plexiglas for large focal spot sizes ($A_s \simeq 0.5$ cm^2) and spectroscopic observations of plasmas formed at the surface of various metallic targets. For these measurements a 1-m McPherson spectrograph was used with the slit oriented perpendicular to the target surface to add spatial resolution to the spectra. The plasma front propagation was observed simultaneously with a streak camera. A wavelength interval of approximately 3500 to 4800 Å was observed. These data will be analyzed and reported in a future publication.

<div style="text-align: right">

J. E. Lowder
L. C. Pettingill

</div>

18-5-4793
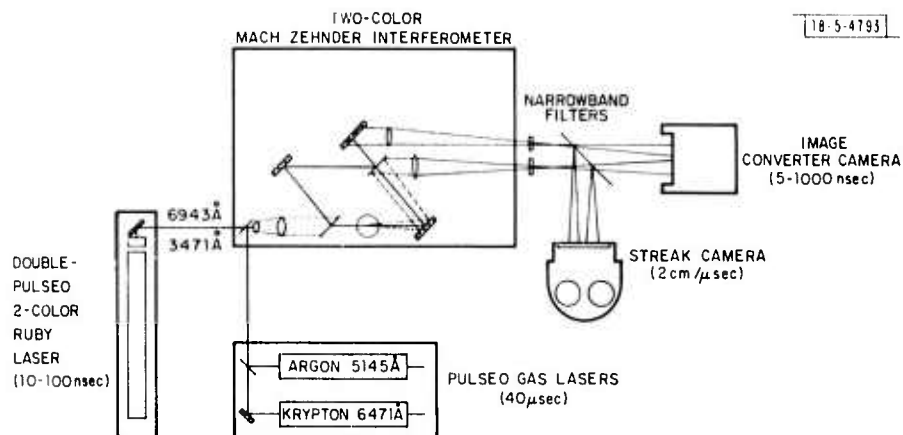
Fig. I-36. Optical schematic of two-color Mach Zehnder interferometer.

-5-4794
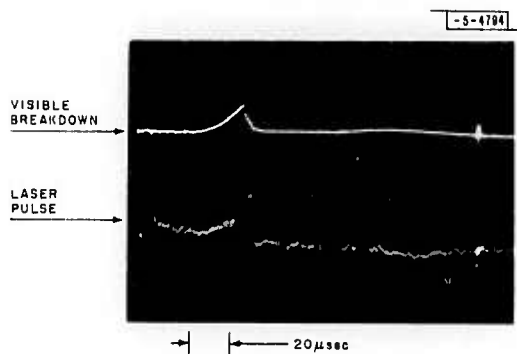
Fig. I-37. Oscillograph of the time history of the incident laser pulse (lower trace) and visible breakdown radiation (upper trace).

18-5-4795

TARGET SiO$_2$

$\bar{P} = 5 \times 10^5$ W/cm^2

A$_T$ = 0.25 cm^2

- ● 4 μsec
- + 6 μsec
- □ 12 μsec
- × 18 μsec

Fig. I-38. Plot of the electron density distribution normal to the irradiated target at 4, 6, 12, and 18 μsec after the onset of a surface breakdown.

28

2. Two-Wavelength Interferometry of Laser-Produced Plasmas

To provide quantitative information on the initiation of laser-produced surface breakdowns we have used a two-color Mach Zehnder interferometer to measure the density distribution of plasmas produced on a quartz target by a focused 10.6-μm pulsed laser. Electron densities have been estimated from the outer shock to near the target surface.

The laser output was a 40-μsec-long temporally smooth pulse focused with a 40-cm focal-length mirror to a 0.5-cm half-power diameter. The irradiance was adjusted to be 5×10^5 W/cm^2 which produces a surface breakdown 10 to 20 μsec after the beginning of the pulse. This delayed breakdown threshold is in reasonable agreement with other experimental results.[22] Under the conditions stated quartz will reach a vaporization temperature $T_v = \sim3000°$K in ~5 μsec. After evaporation it takes an additional 11 μsec to reach steady-state ablation conditions and build the concentration of SiO_2 molecules to a maximum value. There are strong 10.6-μm absorption bands in the vaporized quartz which cause the gas to heat until thermal ionization is sufficient to trigger a breakdown. When the irradiance is reduced a factor of two, no breakdown is observed; a factor-of-two higher flux produces a breakdown with virtually zero delay. In the intermediate flux condition, a 1- to 10-micron thickness of quartz is vaporized on each shot.

To measure the spatial and temporal distribution of plasma material and electron densities in a laser-target interaction over a range of incident flux conditions and pulse lengths, a modular, two-color Mach Zehnder interferometer was constructed (see Fig. 1-36). The 3-inch-diameter interferometer elements have broadband coatings that allow convenient use of several light sources. For examination of thresholds or late times (i.e., cooling plasmas), time resolution of ~1 μsec and observation times of several tens of microseconds are required. Two pulsed gas lasers (argon and krypton) are optically combined to provide a 40-μsec-long, 5145- and 6471-Å beam to illuminate the interferometer for these conditions.

A double-pulsed ruby laser with second harmonic output is to be used for very short exposure, very high-intensity illumination of hot, fast-moving plasmas.

The outputs from the interferometer can be recorded photographically with a fast-writing (~2 cm/μsec exposure) streak camera, two single-frame image converter cameras (5- to 1000-nsec exposure), or by a combination of both. Direct photoelectric observation is not now planned but is easily implemented.

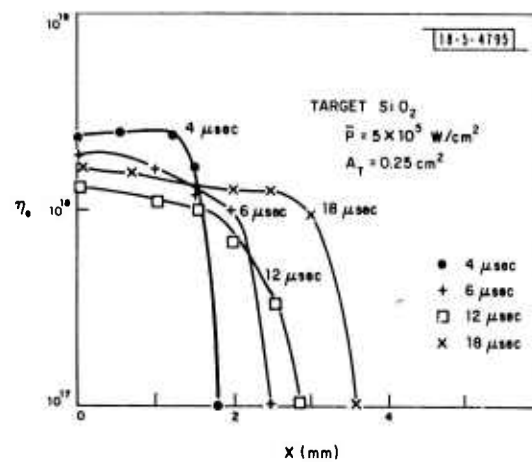In this first set of measurements the two gas lasers were used for illumination. The interferograms were reduced by standard techniques where ionized species can be neglected.[23,24] The optical path over which the electron density was distributed in an essentially hemispherical volume was calculated from the radius or distance from the target where electron density effects were no longer measurable. Similarly, the optical distance in the hemisphere due to neutral particles was calculated from the distance from the target to the boundary between the disturbed and the undisturbed air. Under optimum conditions, the wavelength difference was adequate to measure electron densities of $\gtrsim 10^{17}$/cm^3 in a 1-cm-diameter volume. Near the surface of the target where the electron density is highest, refractive effects virtually destroy the resolution of the fringes and the peak electron density can be estimated to only about a factor of three. Outside of the turbulent core accuracy is obviously better.

Figure I-37 is an oscillograph showing the time history of the laser pulse in the upper trace, and in the lower trace the output from a photodiode looking at the breakdown radiation. Figure 1-38 is a plot of the electron density distribution in the breakdown at various times after the beginning of the breakdown which occurs about 20 μsec after the beginning of the laser pulse.
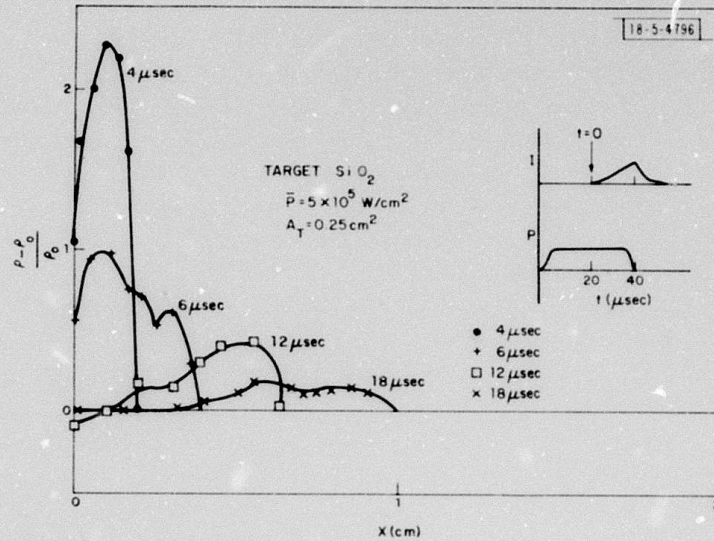
Fig. I-39. Plot of the neutral density distribution for the same data used in Fig. I-38 ($V_p \sim 4 \times 10^4$ cm/sec).
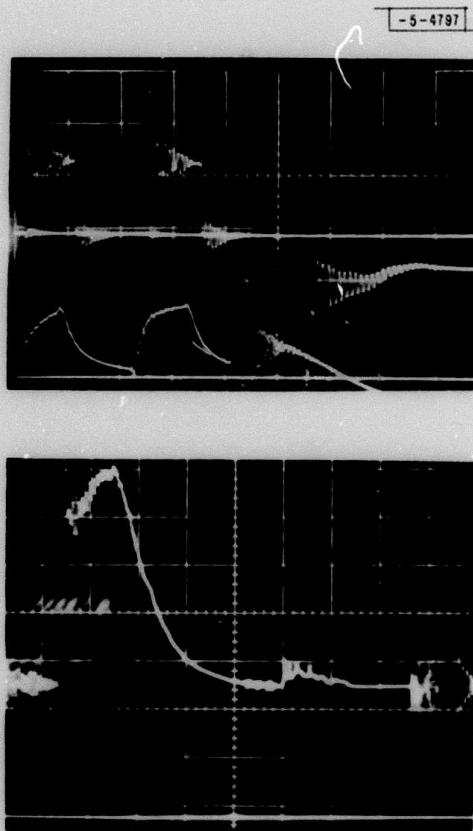
Fig. I-40. The upper trace indicates the electron beam current for the two equal-pulses case. The abscissa is in units of 20 A/division. The middle trace is the sustainer current, with an abscissa of 4000 A/division. The lower trace is proportional to the optical intensity as measured by a photon drag detector. The time scale is 10 μsec/division. The geometric resonator outcoupling was nominally 85 percent.

Within about one beam radius (2 to 3 mm) there is a hemisphere of electron density $\sim 10^{18}/cm^3$. This core remains for the duration of the pulse and effectively shields the surface from most of the incident laser radiation.

In Fig. I-39, the neutral density distribution has been plotted for these same data. The pressure wave moves from the target surface at a velocity of $\sim 4 \times 10^4$ cm/sec and is a pressure rather than a shock wave.

Additional data are being analyzed for other conditions and will be presented in a separate report.

R. W. O'Neil
H. Kleiman
J. E. Lowder

D. DEVICES

1. Single 500-J Laser

a. Measurement of Double-Pulse and Long-Pulse Effects

Using our 500-J E-beam ionized CO_2 laser[25] we have experimented with the pulse parameters for both long single-pulse shots and dual-pulse shots to determine the kinetic limitations on lasing. The adjustable parameters on the modulator of the E-beam allowed selecting the starting of each pulse, the pulse length of each pulse, and the degree of modulation (hence, primary electron beam current) which is the same for both pulses on a given shot. We used the diagnostics developed by R. W. O'Neil et al.[26] to observe the time history and energy of the shots.

The two-pulse shots were performed with 85-percent outcoupling and nominal output energy of 300 J total. Figure I-40 shows a typical shot where the two excitation pulses on the modulator are equal in length, producing equal bursts of ionizing electron beams, each 10 μsec in length and separated by a 15-μsec delay. The sustainer currents are almost identical in magnitude although it is observed that the plasma effects reduce the leading-edge rise time on the second pulse. The time-resolved traces of the laser pulse indicate the first pulse has about 18-μsec length relative to 7 μsec of the second pulse, almost 12 times the peak intensity, and 21 times the total energy. In Fig. I-41, the first electron beam pulse is only 5 μsec in length, and there is a 20-μsec delay before the subsequent 10-μsec E-beam pulse. The corresponding sustainer currents have comparable lengths, but the first sustainer current pulse fails to reach equilibrium before the corresponding E-beam pulse cuts it off. The corresponding laser pulses are comparable in both pulse length and energy. The first laser pulse is 13.75 μsec relative to about 7.5 μsec for the second, and the first has about 1.2 times the energy. Thus, by controlling both the pulse length and pulse amplitude of the ionizing E-beam, we should be able to make a wide range of multiple pulses out of a single device, as long as pulse separation is not a critical factor.

With the 85-percent outcoupling mirrors we also tested to see the maximum pulse lengths achievable, again at nominal energies of 300 J. Gain quenching due to medium heating occurred after 25 μsec although no arc occurred within 100 μsec with 45-μsec E-beam pulses. In Fig. I-42 is shown the laser pulse output for a 50-μsec E-beam current. In this case, with this 34-percent outcoupling cavity configuration, the laser pulse lasts 43 μsec but the power has trailed off due to gain quenching.

A. J. Morency
H. Granek
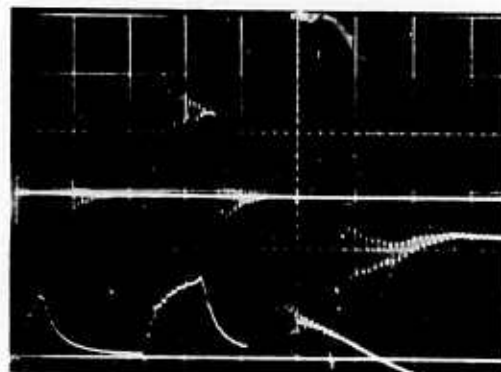
Fig. I-41. The three traces are for the case of electron-beam pulses of unequal length but the same magnitude. The upper trace is the gun current; the middle trace, the sustainer current; and the lower trace is proportional to the optical intensity. The scales are identical to those of Fig. I-40.

(a)

(b)
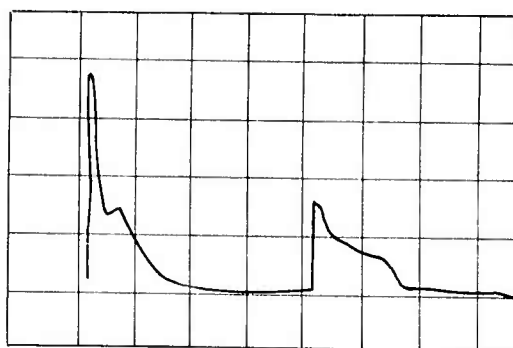
Fig. I-42. We see the electron beam current, the sustainer current, and the optical output for a 50-μsec E-beam current and nominal optical outcoupling of 34 percent. The abscissa of the upper current trace is 10 A/division, the abscissa scale of the sustainer current is 4000 A/division, the optical intensity scale is half as sensitive as in Fig. I-40, and the ordinates are all 10 μsec/division.
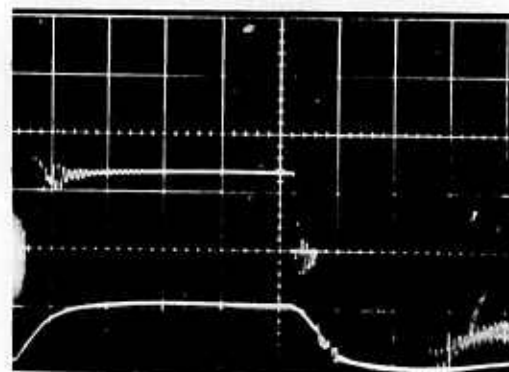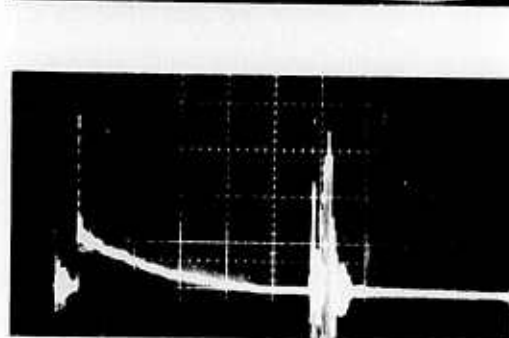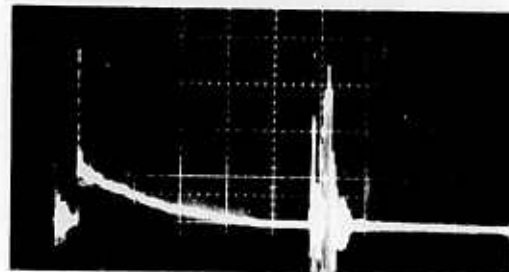
(c)

b. High Equivalent Fresnel Number Confocal Unstable
   Cavity Measurements

The present experimental study[27] presents data on the 500-J electron-beam-ionized CO_2-N_2-He laser[25] with large effective Fresnel number and outcouplings from 34 to 85 percent. For the lowest outcoupling, tuning of the effective Fresnel number was accomplished with change in length. We observe that for the lowest outcoupling, even with an equivalent Fresnel number of the order of 15, there is still a sensitivity of the beam quality to the particular value. For outcouplings of greater than 60 percent, there appears to be no sensitivity to equivalent Fresnel number.
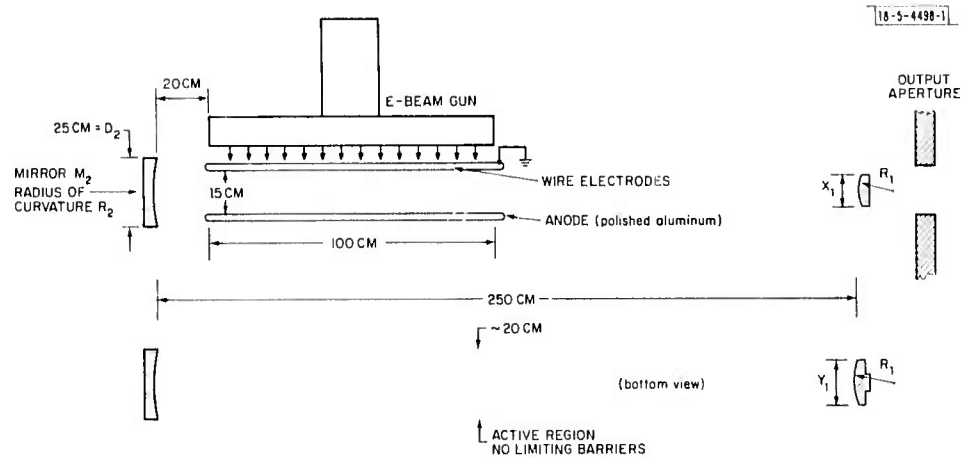
Fig. I-43. Positive confocal unstable resonator cavity configuration used with E-beam ionized CO_2 laser.

A schematic of the laser resonator is shown in Fig. I-43. The two mirrors have been chosen to form a confocal set, with longitudinal adjustment allowed on the secondary. This tuning was used for changing the effective Fresnel number and then the best focal plane position was re-established for measurement. No confining aperture existed in the transverse direction. A polished aluminum anode, we believe, produced some vertical parasitics for the lowest outcoupling systems. The active region is 1 m in length and nominally 15 by 15 cm in cross section with a mirror spacing of 250 ± 9 cm. Both mirrors were copper, and the smaller mirror had a square cross section. Mirror parameters are given in Table I-1.

TABLE I-1					
		Concave Mirror		Convex Mirror	
Geometric Outcoupling	Magnification	Diameter (cm)	Radius of Curvature (m)	Square Cross Section (cm^2)	Radius of Curvature (m)
0.34	1.23	25	26.7	12.2 × 12.2	−21.7
0.6	1.58	25	13.6	9.5 × 9.5	−8.6
0.85	2.58	25	8.2	5.3 × 5.8	−3.2

$I_{3n} = 0.0091\ I_o$ $I_{4n} = 0.0064\ I_o$ $I_{5n} = 0.0050\ I_o$

$I_{6n} = 0.0031\ I_o$ $I_{7n} = 0.0017\ I_o$ $I_{8n} = 0.00068\ I_o$

$M = 2.58$
$N_{eq} = 24.27$

(a)

$M = 2.58$
$N_{eq} = 24.27$

EXPERIMENTAL

THEORETICAL

$\int_{-\infty}^{+\infty} I(x,y)\,dy$

X
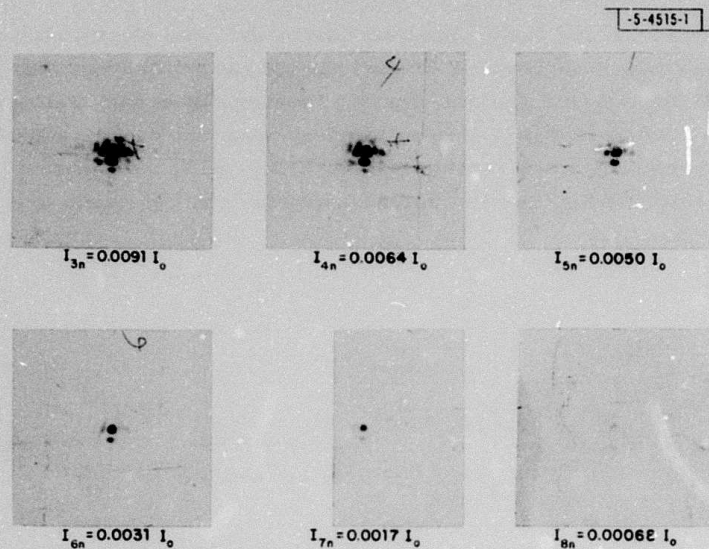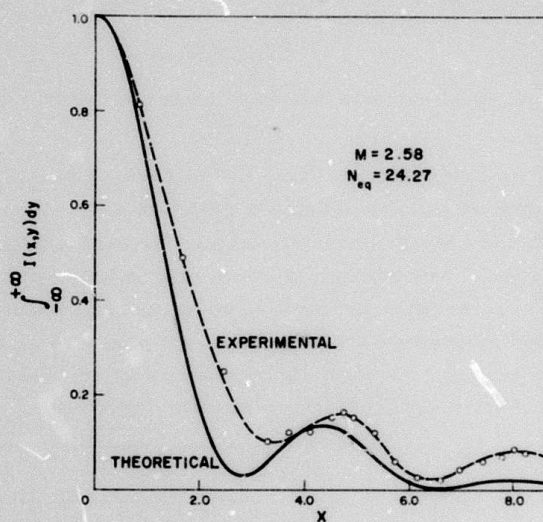
(b)

Fig. I-44. (a) Burn pattern for mirror configuration for $\delta = 0.85$ and $N_{eq} = 24.27$ and (b) the transverse energy integrated in the vertical direction.

34

For alignment, two techniques have been employed with success. Both use a far-downrange autocollimator that is aligned to the center of the cavity. The large primary mirror is installed and aligned. The secondary mirror is installed and rough-aligned off of its mirrored back surface. The image projected by the autocollimator and formed by round-trip transversal through the cavity is then centered. A helium-neon beam is then brought into the system via a replaceable pellicle at an intermediate position and aligned on the telescope. This beam is used for downrange alignment.

Another technique that we have found extremely convenient is to insert a collimated helium-neon laser beam through a small hole in the primary and align the beam on the image formed by the unstable resonator. The downstream beam then produces extremely accurate aiming for the CO_2 laser pulses, and this is convenient for setting up downrange detection systems. Preliminary evidence indicates that the hole in the primary produces negligible effects on beam quality.

We use the diagnostic techniques developed by R. W. O'Neil et al.[26] to reconstruct the energy profile of the focal-plane radiation field. This is achieved by passing the beam through a 10.6-μm transmission grating and recording the diffraction orders on Electrotrace thermal sensitive paper. Burn patterns of the various orders are indicated in Figs. 1-44 through I-46.

The parameter that best characterizes the laser is the equivalent Fresnel number as defined by Siegman[28]

$$N_{eq} = \frac{a_1^2}{\lambda L} \left[\frac{g_1}{g_2} (g_1 g_2 - 1) \right]^{1/2} \tag{I-4}$$

where a_1 is half the small-mirror diameter, λ is the laser wavelength, L is the mirror separation, and

$$g_i = 1 - L/R_i \tag{1-5}$$

for the two mirrors, R_i being the mirror radius of curvature. For the positive confocal branch of the unstable resonator, g_1 and g_2 are related to the round-trip geometric magnification, M, by

$$g_2 = \frac{M + 1}{2M} \quad \text{and} \quad g_1 = \frac{M + 1}{2} \tag{I-6}$$

where 1 refers to the smaller convex mirror and 2 refers to the larger concave mirror. In describing the outcoupling it is convenient to use the parameter

$$\delta = 1 - 1/M^2 \tag{1-7}$$

which is the geometric outcoupling, although the resonator fields usually establish themselves such as to minimize the diffractive outcoupling and thus an outcoupling less than the value that is given by Eq. (1-7) in general exists.

In Fig. 1-44(a) is a characteristic burn pattern for the 85-percent outcoupling, corresponding to a magnification of 2.58. One can see even with this outcoupling an asymmetry in the y-direction, which is present in all of the data. We have not established its source, but there are three known asymmetries in the system: the secondary mirror is supported on a post from above, the polished aluminum electrode can permit field distortion on the bottom, and the electron density variation due to the high-energy electrons entering from above can produce y-variations in gain.

Because of the asymmetry in the y-direction, we feel that the most appropriate way to describe the beam quality is relative to the intensity distribution in the transverse direction having

$I_{2n} = 0.011\, I_o$ $I_{3n} = 0.0091\, I_o$ $I_{4n} = 0.0064_o$

$I_{5n} = 0.005\, I_o$ $I_{6n} = 0.0031\, I_o$ $I_{7n} = 0.0017\, I_o$

$M = 1.58$
$N_{eq} = 23.78$

(a)

$M = 1.58$
$N_{eq} = 23.78$

EXPERIMENTAL

THEORETICAL

(b)
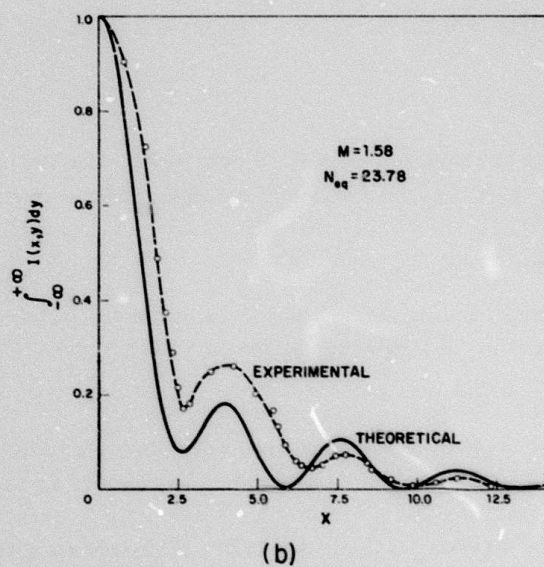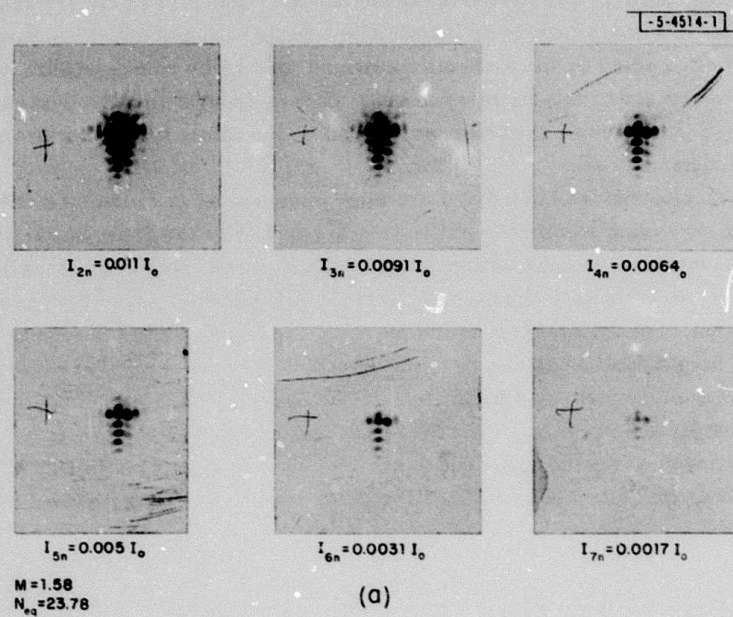
Fig. I-45. (a) Burn pattern and (b) one-dimensional energy profile integrated in vertical direction for $\delta = 0.6$ and $N_{eq} = 23.78$.

$I_{2n} = 0.011 \ I_o$ $I_{3n} = 0.0091 \ I_o$ $I_{2n} = 0.011 \ I_o$ $I_{3n} = 0.0091 \ I_o$

$I_{4n} = 0.0064 \ I_o$ $I_{5n} = 0.0050 \ I_o$ $I_{4n} = 0.0064 \ I_o$ $I_{5n} = 0.0050 \ I_o$

$M = 1.23$
$N_{eq} = 15.59$ (a) $M = 1.23$
$N_{eq} = 15.65$ (b)

$I_{2n} = 0.011 \ I_o$ $I_{3n} = 0.0091 \ I_o$

$I_{4n} = 0.0064 \ I_o$ $I_{5n} = 0.0050 \ I_o$

$M = 1.23$
$N_{eq} = 15.71$ (c)
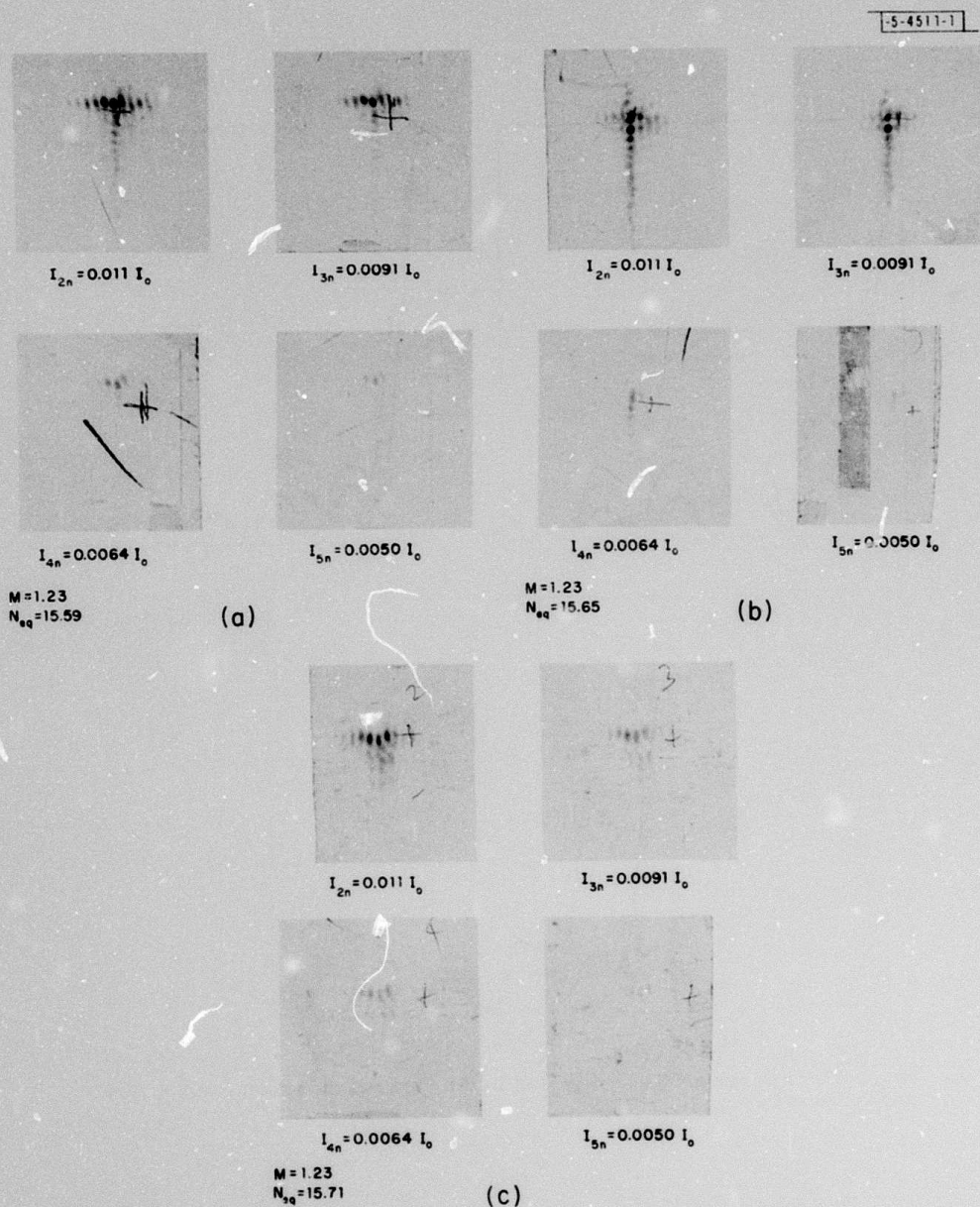
Fig. I-46(a-c). Burn patterns for $\delta = 0.34$ and three values of N_{eq}.
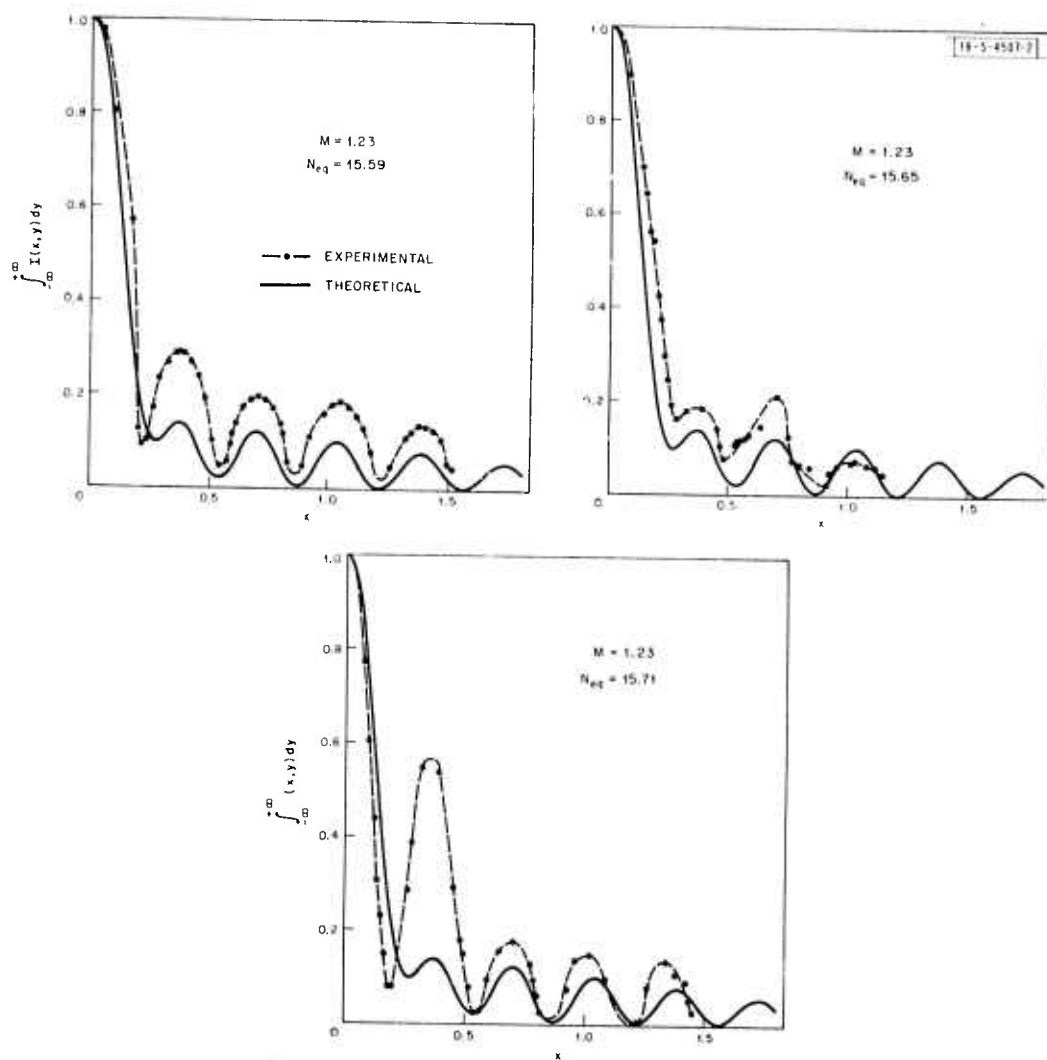
Fig. I-47. Energy profile integrated in the vertical direction for $\delta = 0.34$ and three values of N_{eq}.

integrated the intensity in the y-direction for a given x, normalizing the peak intensity to 1. This is compared to the solid curve of a uniform radiation field upon our output mirror and aperture in Fig. 1-44(b) for the 85-percent outcoupling. The intensity distribution integrated along the y-axis is achieved by weighting the spot sizes in the y-direction and summing all such intensities. For our measurements, the energy in any unmeasured portions have been less than 6 percent of the total energy. It is important to observe that the equivalent Fresnel number is not a half integer value for this case. The beam quality was essentially invariant of the equivalent Fresnel number for this high equivalent Fresnel number, high-outcoupling case, although less than diffraction limited.

The same is true for our intermediate case of 60-percent outcoupling, whose characteristic burn pattern is shown in Fig. I-45(a). Here we again have good symmetry in the transverse direction, but the asymmetry in the y-direction becomes worse than for $\delta = 0.85$. In Fig. I-45(b) we see the transverse energy distribution integrated in the y-direction for the 60-percent case.

For the 34-percent outcoupling resonator, we begin to see the effect of tuning the equivalent Fresnel number. Even for a high value of the order of 15.5, the exact value appears to be important. The beam quality falls off as the value of the equivalent Fresnel number is shifted from half integer towards an integer value. This is seen as the energy for 15.65 is spread in the transverse direction, and for 15.71 is spread strongly in two spots in the vertical direction in Fig I-46. In Fig. I-47, however, a comparison of the patterns integrated in the y-direction shows that the $N_{eq} = 15.59$ is close to the ideal case while the $N_{eq} = 15.71$ and 15.65 cases are more distorted relative to the ideal limit, although definitely more divergent than the diffraction-limited case.

Fig. I-48. Comparison of fractions of total energy in central spot versus geometric outcoupling as predicted by uniform illumination of output mirror and output aperture (solid curve) and as measured experimentally (dashed curve).
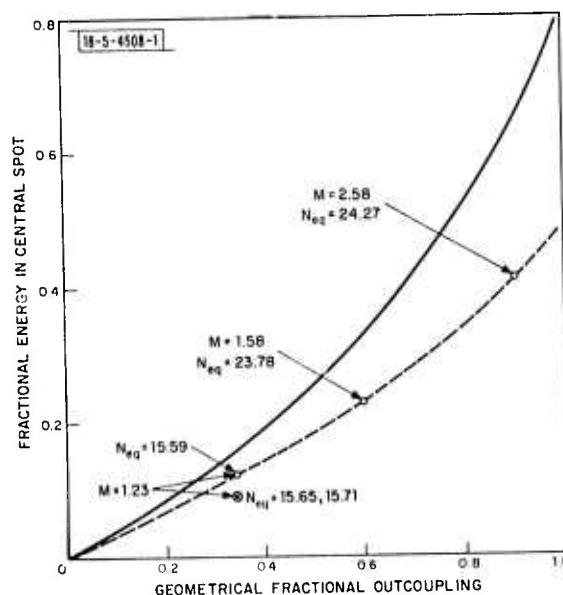
In Fig. I-48 we see a comparison for all of these cases of the fractional energy in the central focal spot compared to the diffraction-limited.case. All of the cases are less than diffraction limited, but the 34-percent outcoupling cases that are farthest from half integer equivalent Fresnel number are noticeably worse. The primary conclusions we can draw from these results are that for outcouplings at least greater than 60 percent, near diffraction-limited far-field radiation patterns are achievable and insensitive to the particular value of the equivalent Fresnel number
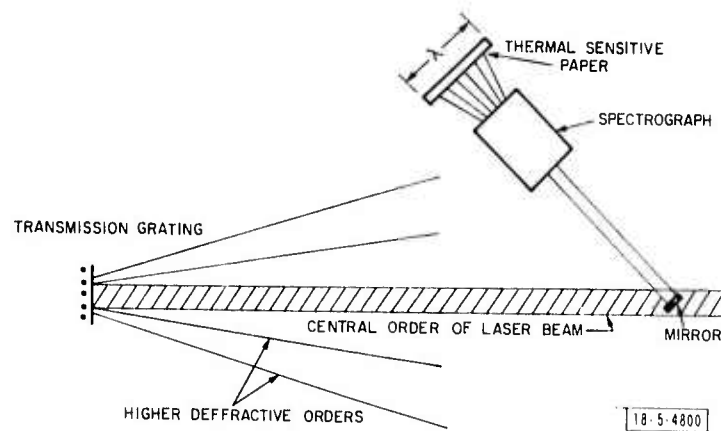
Fig. I-49. Schematic of technique to measure transition frequencies of the E-beam CO_2 laser. In order to time resolve the lines, a second spectrum analyzer receives another clipped portion of the central order of the transmission grating and fast detectors are inserted at the positions of the various lines. Total energy and time history of the composite beam are measured at the diffraction orders of the 10.6-μm transmission grating.
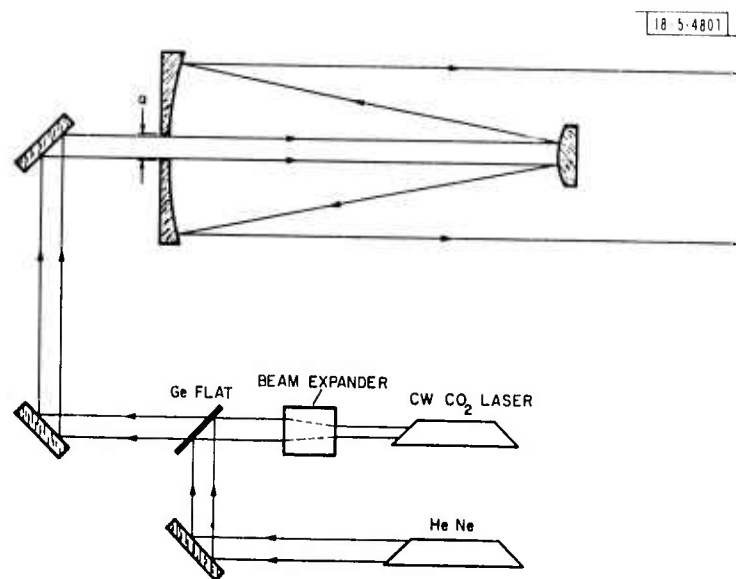
Fig. I-50. Scheme to injection-lock the pulsed E-beam laser. The beam expander on the CW CO_2 laser produces a near collimated output. The He-Ne is used for downrange alignment and is kept inserted even during the shot. Insertion holes of both 4-mm and 10-mm diameters were used.

for large values of this parameter. However, for lower outcoupling, at least 34 percent and less, the beam quality is improved near half integer values of the equivalent Fresnel number, even for $N_{eq} \approx 15$.

<div align="right">
H. Granek
A. J. Morency
</div>

c. Frequency Measurement and Injection Locking

To enhance our understanding of the kinetics of our 500-J E-beam-ionized CO_2 laser, we implemented a scheme to monitor the laser transitions that occur as we vary the lasing conditions. Seen in Fig. I-49 is a schematic of the experiment where we clip part of the central order and direct it into a spectrograph after which the positions of the various 9.4- and 10.6-μm rotational transitions recorded on thermosensitive paper are resolved and calibrated. With the sensitivity of the paper, we can observe transitions over about an order of magnitude of intensity and thus can adjudge that if any other transitions lased they were at least down by this factor from those which were observed.

We noted that in our 85-percent square unstable resonator configuration the laser consistently produced output on a single transition when a single 20-μsec E-beam pulse ionized the medium, although from shot to shot the transition might vary between P(16) and P(20) of the 001 → 100 vibrational band.

When the laser was double pulsed with a 5-μsec initial pulse, a 20-μsec delay, and then a 10-μsec pulse, transitions were observed with about equal intensity on P(16) and P(20) of 10.6-μm band, and more weakly on the P(18) transition of this band. We have not yet observed the time history of each of these rotational transitions, so we cannot confirm the agreement of these results with theory; time-resolution spectroscopy is planned for the future.

In an attempt to injection-lock the laser on a particular desired transition, we inserted a 7-watt CW laser on the R transition of the 001 → 020 band through a small hole in the concave mirror of the 70-percent circular set of optics (see Fig. I-50). When the hole was 4 mm in diameter, no degradation in the far-field pattern and energy was noticed for single pulsing. When the hole was expanded to 10 mm, a reduction in total energy of the laser was observed but the laser still operated on a single transition for single pulsing when the CW laser was not injected. When the CW laser was injected, weaker lasing was additionally observed in the P(16) transition of the 10.6-μm band also for a single pulse. No time resolution of these transitions has yet been made, although further experiments for injection locking are planned.

<div align="right">
H. Granek
A. J. Morency
</div>

d. Laser Beam Diagnostics

Energy Density Measurement

When substantially all of the laser energy reaching a focal plane is contained in the diffraction pattern appropriate to the specific output aperture, the energy distribution in the focal pattern can be reconstructed from grating generated burn patterns.[29] To demonstrate that there is no large spray contribution or significant redistribution during the pulse (e.g., from thermal blooming) the focal pattern was scanned using a number of semi-infinite narrow-aperture calorimeters in five or more grating-generated diffraction orders. Recently, this basic scanning operation has been greatly simplified with a 16-element commercial calorimeter array constructed

E(x)

| | 5 mm
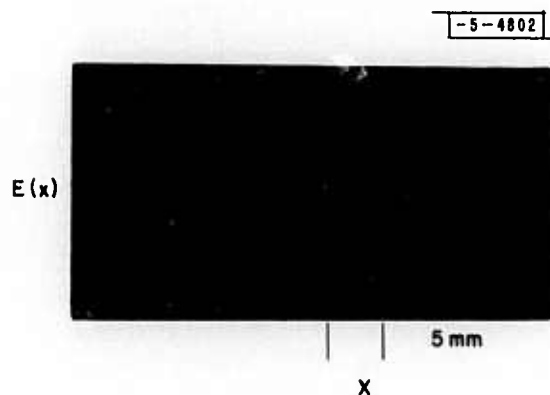
X

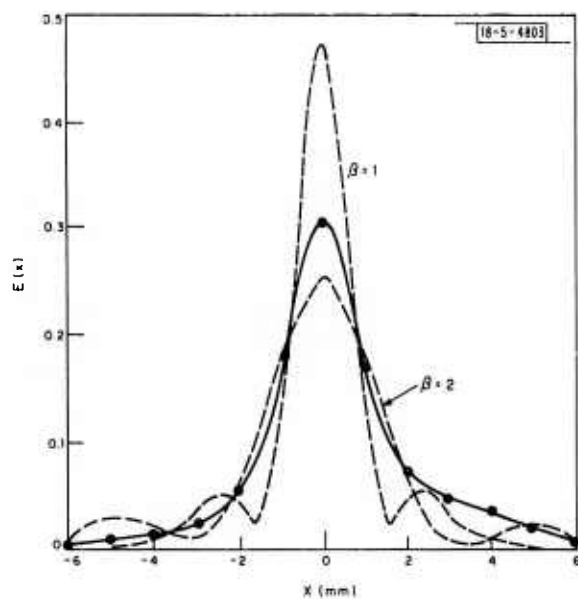Fig. I-51. Multiplexed output from a 16-element energy scanning array.

Fig. I-52. Plot of data in Fig. I-51 along with distributions appropriate to a diffraction-limited beam ($\beta = 1$) and to this same distribution increased in scale a factor of 2 ($\beta = 2$).
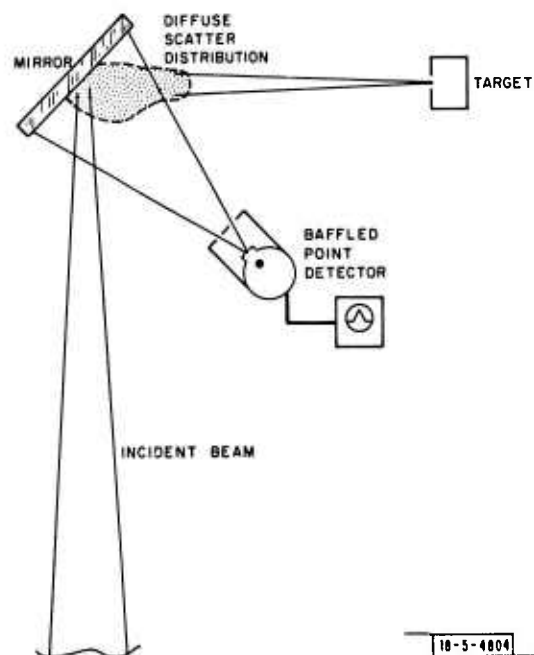

Fig. I-53. Scheme to measure the relative total power by detecting the scattered radiation from a specular mirror.

42

at our request with long (1.5-cm), narrow (0.1-cm) pyroelectric elements. This unit accepts a single diffraction order and presents a single multiplexed output which is a one-dimensional scan of the focal energy in a 1.5- × 1.7-cm area. Figure I-51 is a typical example of such a scan taken of the output from the Lincoln Laboratory E-beam laser. Figure I-52 is a comparison of the profile obtained by this technique to the diffraction-limited distribution $\beta = 1$ and to the same distribution increased in scale a factor of 2 ($\beta = 2$).

Power Measurements

Although the measurement of the power output of a focused high-energy laser is easily accomplished with photon drag detectors used in side orders of a diffraction grating, it is sometimes useful to measure the total power before it has been sampled with a grating. (Multi-wavelength operation is a typical example.) The method now used routinely is illustrated in Fig. I-53. A fast point detector (PbSnTe) is placed a short distance from a bending mirror to view at near-normal incidence the diffuse scatter from the specular surface. A commercial-quality mirror finished to $\pm\lambda/2$ in the visible irradiated at near 45 degrees with a nearly collimated beam scatters 10^{-4} to 10^{-5} ster^{-1} of the incident power near the mirror normal. When the detector is carefully baffled to see only the specular surface or the incident beam is apertured to insure that this condition is met, the detected signal is a measure of the total power as a function of time. Although very small changes in the mirror surface or geometry can change the scattered fraction, absolute calibration is a possible, but difficult, task.

As part of a relative calibration procedure, this detection scheme was compared with the photon drag detectors. A 1-J TEA CO_2 laser pulse was focused via an observation flat onto a photon drag detector. When the beam incident on the bending mirror was constrained to fall on only the central area of the specular surface, the photon drag signal and the time history of the scattered radiation measured by the point detector were identical. When the defining aperture was enlarged to a diameter just slightly larger than the viewing mirror the point detector signal indicated a large growth of power with time. Actually, a small fraction of the incident laser beam spreads progressively beyond the viewing mirror edges and appears as an erroneously larger signal late in the pulse. Although the edge spreading is generally low-level, the higher scattering efficiency of the mirror edges and mount contributes disproportionately to the scattered signal. Figure I-54(a-c) shows oscillograph traces of power measurements from the Lincoln Laboratory laser operated at ~300 J in a 20-μsec pulse. The photon drag traces are in the left-hand column, and the corresponding point-detector signals from the radiation scattered from the 30-cm-diameter viewing mirror are in the column on the right. When the field-of-view of the scattering detector was restricted to the irradiated region of the mirror (15 × 20 cm), good agreement can be seen [Fig. I-54(a)]. In Fig. I-54(b), the field-of-view was nearly 30 cm and there is some serious late time distortion. When no baffling was used, the scattered radiation, which bears little resemblance to the actual power history, is dominated by contributions from outside the irradiated area for times greater than ~1 μsec [Fig. I-54(c)].

This low-level spreading of the laser beam with time has been observed on both the AVCO and Lincoln Laboratory E-beam lasers and also on several TEA lasers and is probably a general property of pulsed high-energy lasers.

I(t)

5 μsec

t

t
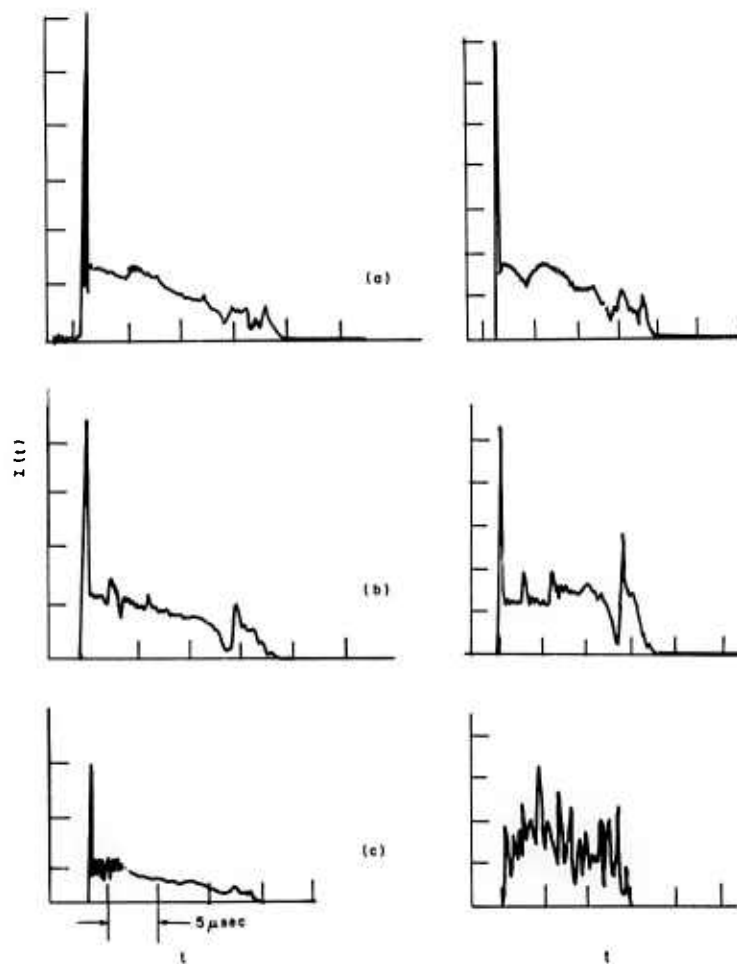
18-5-4449-1

Fig. I-54. Oscillograph traces of power measurements made on the Lincoln Laboratory laser operated at ~300 J. Photon drag traces made in a grating order are in the left-hand column. PbSnTe diode traces are in the right-hand column. As explained in the text, the three sets of data compare the two detection schemes for different fields-of-view of the point detectors.

Time Resolved Measurement of Focal Irradiance

To measure spatial changes in the focal distribution of a pulsed laser beam as a function of time, two complementary techniques have been developed. The first is an obvious extension of the energy density measurement using multiple grating orders where fast, power-sensing detectors replace the calorimeters.[29] Photon drag detectors equipped with 5-cm aperture shallow-angle copper cones are placed behind semi-infinite narrow scanning apertures (3 cm × 0.1 cm) that are positioned to scan the focal distribution. Figure I-55 is a typical example of the one-dimensional power distribution at t = 0.5 μsec. The normalized appropriate distribution for a diffraction-limited beam is indicated.
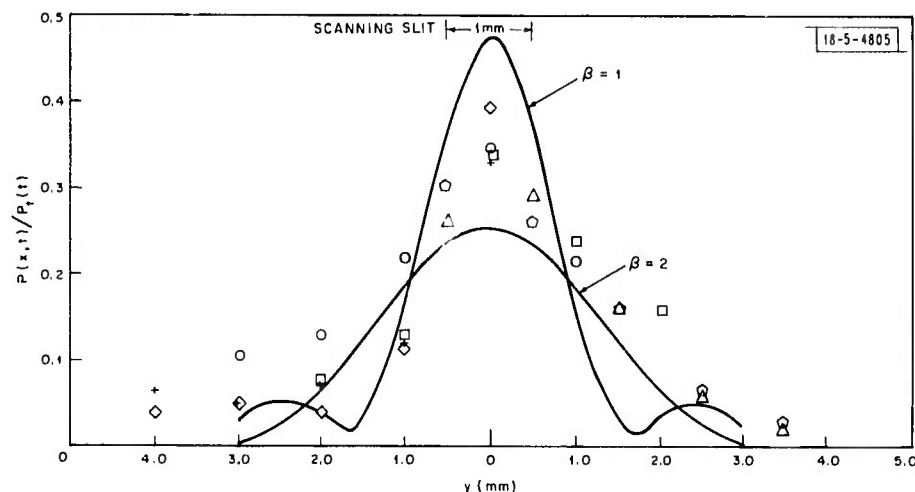
Fig. I-55. The normalized fraction of the total power passing through 5 scanning apertures is plotted for 6 typical shots. On the graph a theoretical curve has been drawn that corresponds to a diffraction-limited beam scanned by a 1-mm-wide semi-infinite aperture ($\beta = 1$). A second curve ($\beta = 2$) is an identical scan of a diffraction-limited distribution scaled upward a factor of 2.

The second technique is illustrated in Fig. I-56. A transmission grating side order is focused on an ultra-low-scatter mirror. The small diffuse component from this very uniform viewing screen is imaged by a BaF lens onto a 21-element HgCdTe detector array (Fig. I-57). The magnification of the imaging optical system is adjusted to achieve the desired spatial resolution required for the focal pattern being measured. In the near future, two such arrays will be sampled with a 48-channel, 10-MHz digital sampling system.

Prior to the completion of this recording system, fifteen channels of a single array were used to observe the focal pattern produced by the Lincoln Laboratory 500-J laser. Once the contributions from the electrical and optical backgrounds were substantially eliminated, the imaging-array system was used during recent pulsed thermal-blooming experiments to measure the redistribution of the focal energy. Figure I-58 illustrates the instantaneous profiles along the x-axis when focused through a non-absorbing path ($\alpha < 10^{-6}$ cm^{-1}).

R. W. O'Neil
H. Kleiman
G. L. Valcourt
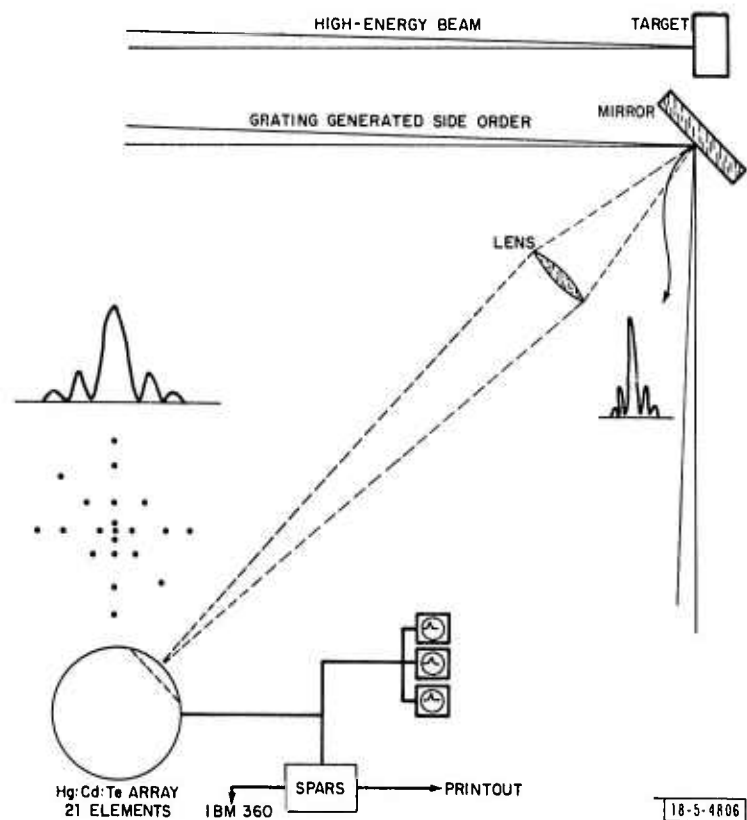
Fig. I-56.   Illustration of technique to measure the spatial and temporal distribution of focused laser energy.

P179-60

(a)

Fig. I-57. (a) 21-element Hg:Cd:Te detector array and amplifiers; (b) enlargement of detector array elements.

P179-61

(b)
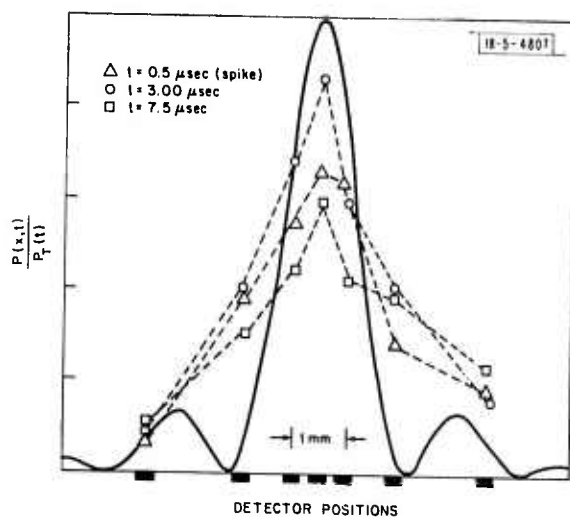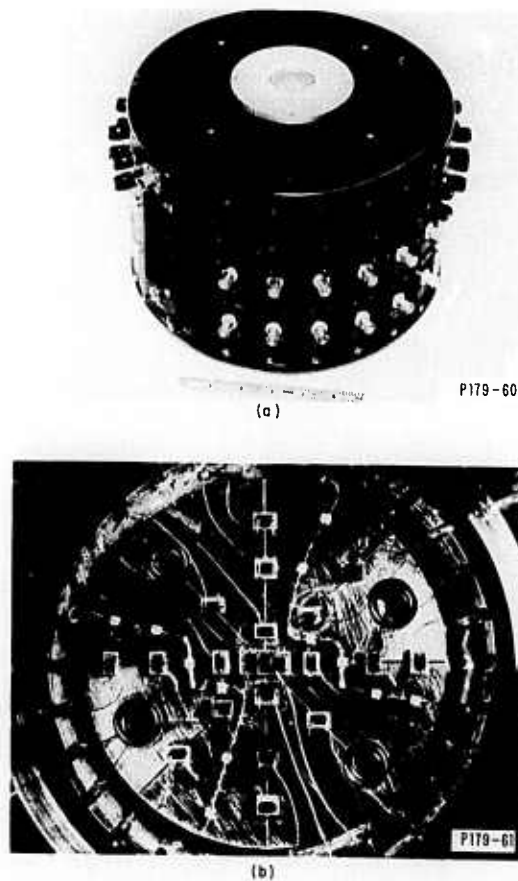
Fig. I-58. The instantaneous power distribution along the x-axis as measured by 7 small-area detectors. Measured values at 3 observation times have been plotted with theoretically predicted diffraction-limited distribution.

2. Dual 500-J E-beam Laser

The 500-J E-beam device will be modified this summer by the addition of a second identical laser. This will permit double-pulse experiments requiring pulse separation of up to a few milliseconds.

The changes to the control system and physical arrangements will be completed during the month of July and will require the complete shutdown of the existing laser. A description and current status of each major component for this system are given below.

a. Electron Gun

A second Physics International (PI) electron gun has been procured.

b. Vacuum System

The dual system will use the existing Turbo-Molecular systems for pumping of the electron guns. The sustainer cavities will be evacuated with mechanical pumps. These components have been ordered and will be delivered shortly.

c. Sustainer Enclosure

An interim thin-wall Lucite cavity has been fabricated for initial use in the dual system in a flowing-gas configuration. An aluminum cavity is now being designed for high-pressure operation within the sustainer cavity, and this should be ready for use this fall.

The remaining components in the system are either identical to or very similar to the existing components.

Tests and diagnostics on the dual laser will start early in August and the new system is expected to be operational some time in September.

A. J. Morency   P. J. Rothenheber
W. R. Fanning   S. E. Woodbury

3. Photoionization

a. Experimental Determination of Photon Penetration
   Depth in Tri-n-propylamine

In earlier publications[30,31] the authors speculated on the possibility of producing laser plasmas by photoionizing trace amounts of a low-ionization-potential species added to the normal gas laser medium. The penetration depth of the ionizing radiation in such a scheme is determined
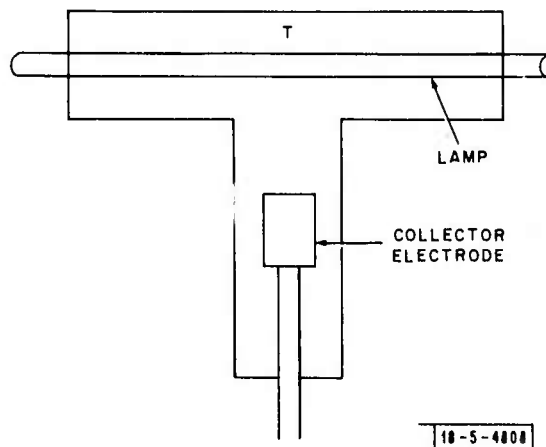
Fig. I-59. Apparatus for measuring Photon Penetration Depth.

by the density of the seedant and the cross section for absorption of ionizing radiation by ground-state seed molecules: $L = 1/n\sigma$. The realization of laser pumping via a photoionization-generated plasma was reported in a subsequent publication.[31] In this initial device a large organic molecule, tri-n-propylamine, is photoionized in a two-step process, the initial step being the absorption of an UV photon into a band extending from 2500 to 2000 Å. It can be simply shown that it is this initial absorption which determines the effective penetration of ionizing radiation and the spatial extent of the resulting photoelectrons. We present the results of a direct measurement of the spatial distribution of electrons produced by the photoionization of tri-n-propylamine in a buffer of N_2. The penetration depth for photoionizing radiation is extracted from this data and an effective absorption cross section for the process is determined to be 7.3 Mbarn.

Photoelectron spatial distribution was measured in an apparatus represented schematically in Fig. I-59. Enclosed in a glass "T" are a 7-mm i.d. Xenon flashlamp and a photoelectron collecting electrode which is movable by means of a support tube which slides through a double o-ring seal. The collector consists of a disc-shaped anode, 1 cm in diameter, surrounded by a wire-mesh cathode. Photoelectrons formed in the 0.5-cm-thick disc-shaped region between anode and cathode are swept to the anode by a 400-volt accelerating potential. The resultant current is proportional to the photoelectron density when the accelerating potential is below that which produces avalanche multiplication. All data were taken in this low-field regime. Electrons formed outside the screen are not detected because the cathode acts like a Faraday cage in confining the collecting field to the region between anode and cathode.

A mixture of 500 torr N_2 and trace amounts of tri-n-propylamine were flowed slowly through the apparatus. The seedant density was determined by measuring the UV absorption of the mixture and comparing it to the known absorption of tri-n-propylamine at densities corresponding to its known vapor pressure at STP. Relative photoelectron density was measured as a function of d, the distance between the photon source and the ionization volume. Results of the 0.5- and 0.01-torr tri-n-propylamine density runs are presented in Fig. I-60. The penetration depth for ionizing photons may be extracted from this data in the following manner.

Fig. I-60. Photoelectron density vs lamp to collector distance for 0.01 torr (top) and 0.5 torr (bottom) tri-n-propylamine.
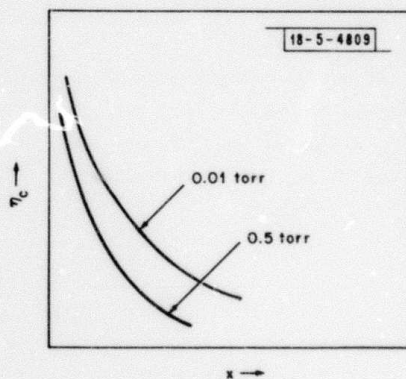
Tri-n-propylamine is ionized by the absorption of two photons in succession. For simplicity, we assume that both photons lie within a bandwidth $\Delta\nu$ over which the initial photon absorption cross section has an average value σ. It can be simply shown that this initial-step cross section determines the photoelectron spatial distribution. Ionizing light intensity as a function of distance may be expressed as the product of two factors.

$$I(x) = G(x) \, e^{-n\sigma x} \tag{I-8}$$

The first factor $G(x)$ describes the fall in light intensity due to geometric spreading of the beam. For a perfectly collimated beam this factor would be a constant. The exponential accounts for photon absorption and the exponent gives the penetration depth for ionizing light as

$$L_{photon} = \frac{1}{n\sigma} \tag{I-9}$$

where n is the tri-n-propylamine density. Photoelectron density varies with light intensity as shown in Eq. (I-10).

$$n_e = An\sigma I^2 \quad . \tag{I-10}$$

The factor A is a constant in the spatial coordinate (see Sec. IV-C-3). Substituting Eq. (I-8) into Eq. (I-10) gives the fall-off of photoelectrons with distance from the photon source,

$$n_e(x) = An\sigma G^2(x) \, e^{-2\sigma nx} \quad . \tag{I-11}$$

For a collimated beam of ionizing light, the electron distribution shows an exponential fall-off with characteristic length $L_{electrons} = 1/2n\sigma$.

In order to eliminate the unknown factor, G, from the analysis, the following ratios are found. For a given seedant density, the ratio of electron densities at two distances, x_a and x_b, is computed.

$$R(x_a) \equiv \frac{G^2(x_a)}{G^2(x_b)} \, e^{-2n\sigma(x_a - x_b)}$$

The factor $R(x_a)$ is evaluated for a second seedant density and a second ratio found.

$$\frac{R^{(1)}(x_a)}{R^{(2)}(x_a)} = e^{-2\sigma[(n^{(1)} - n^{(2)})(x_a - x_b)]} \tag{I-12}$$

The superscripts denote two different tri-n-propylamine concentrations. Experimentally, the electron density is determined by measuring a current which depends in part on the electron mobility through the doped gas. There may be some small variation of mobility with seed density, but the ratio in Eq. (I-12) eliminates this uncertainty from the analysis. Taking Eq. (I-12) for the cross section yields

$$\sigma = \frac{1}{2\left[(n^{(2)} - n^{(1)})(x_a - x_b)\right]} \ln \frac{R^{(1)}(x_a)}{R^{(2)}(x_a)} \quad . \tag{I-13}$$

The expression (I-13) is evaluated with $x_b = 0.5$ cm, $n^{(1)} = 7.6 \times 10^{14}$/cc (0.02 torr) and $n^{(2)} = 2.2 \times 10^{16}$/cc (0.57 torr) for $x_a = 1$, 2, and 3 cm (the range over which the data are reliable). This gives an average value of $\alpha = 7.3 \times 10^{-18}$ cm^2, with a scatter in the results of ± 15 percent. A typical tri-n-propylamine density for a 1-atm CO_2 laser is 0.1 torr, for which the penetration depth $L_{photon} = 36$ cm and $L_{electron} = 18$ cm.

<div align="right">J. S. Levine</div>

b.   Spectrum Measurements of New Seed Molecules

As previously reported[32] efforts are being continued to examine new seedant molecules for photoionization of lasing mixtures.   In the past, tri-n-propylamine has been found to be extremely attractive as such a seedant; but still sought are other molecules with good absorption coefficients, low photoionization potentials, and absorption spectra better matched to the photon source and which minimize the interaction with kinetics of the lasing molecules.   Presented in Fig. I-61 are the transmission curves from 1850 to 3600 Å for N-methylaniline, N, N-dipropylaniline and N, N-dibutylaniline at their respective vapor pressures, all of which have ionization potentials of the order of 7 electron volts.   These molecules might be attractive both because of their possible increased penetration depth and their absorption of higher wavelength photons.   Further experimental tests on the usefulness of these molecules are planned by J. S. Levine.
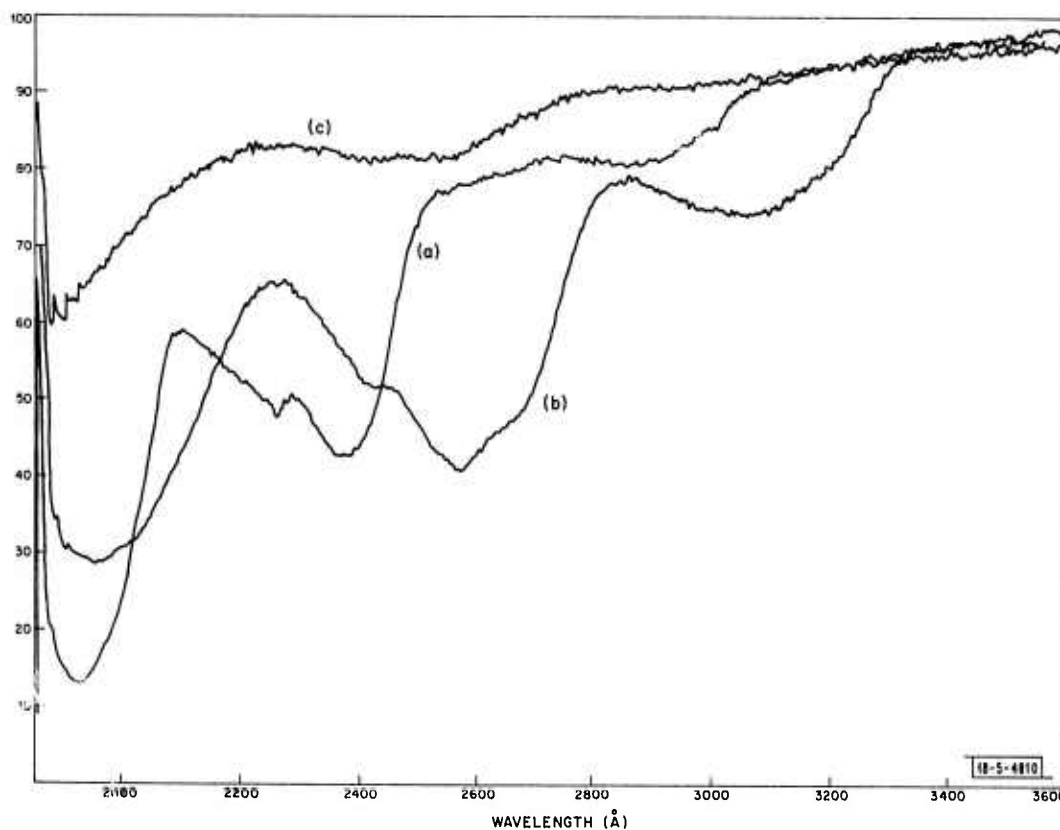
Fig. I-61.   The transmission spectra in the near UV for three anilines are shown:
(a) N-methylaniline in a 1-cm cell; (b) N, N-dipropylaniline in 5-cm cell; and
(c) N, N-dibutylaniline in a 10-cm cell.

Compared with the tri-n-propylamine with its maximum absorption at approximately 2140 Å and α = 2.44 cm^{-1} at its vapor pressure of 2.9 torr, the N-methylaniline appears to be attractive with an α = 0.84 cm^{-1} at 2375 Å at its vapor pressure.   Likewise, N, N-dipropylaniline with relative absorption minimums at 2570 and 3050 Å with respective absorption coefficients of α = 0.178 cm^{-1} and α = 0.06 cm^{-1} might be useful because of its higher wavelength response.   The absorption of N, N-dibutylaniline appears to be too weak to be a likely candidate.

H. Granek

c. Theoretical Analysis of Efficiency of Photoelectron Production

The substantial penetration depth obtained in the previous report implies that large volume plasmas may be produced in high-pressure gas media. In this section we perform a theoretical analysis bearing on the efficiency with which coherent radiation may be produced via a photoelectron-pumped laser.

We define the quantity conversion gain, C_g, as the ratio of the UV energy absorbed per unit volume in producing ionization to the laser energy coupled out per unit volume. Conversion gain is only one link in the chain of processes which must be inspected to determine the overall efficiency of a laser. It is this term, however, which determines the efficiency of the unique photoionization process which we consider here.

It is convenient to express the outcoupled energy density in terms of a mean collision time for electrons

$$\frac{n_e}{\tau_m} \, h\nu_{1R} \tau_p = \text{outcoupled energy density} \quad . \tag{I-14}$$

Here, $h\nu_{1R}$ is the energy of each 10.6-μm photon and τ_m is the mean time for collisions between electrons and molecules which lead to population of the upper laser level, τ_p is the flash pulse length, and n_e is the electron density.

Equation (I-14) says that the rate of upper laser state production per electron times the number of electrons per unit volume times the energy of the photon produced by each excited molecule times the duration of photon production equals the outcoupled energy density. For an outcoupled energy density of 25 J/liter in a 10-μsec pulse and $n_e = 5 \times 10^{12}$, typical of an atmospheric pressure CO_2 laser, τ_m is 2.5×10^{-11} second.

Conversion Gain for Single-Step Photoionization

The equilibrium electron density for a single-step ionization when $\tau_p > \tau_e$ is given by

$$n_e = Rn\sigma\tau_e \tag{1-15}$$

where

R = rate of arrival of ionizing photons/cm^2

σ = photoionization cross section from the ground state of the seedant

τ_e = free electron lifetime

τ_p = duration of ionizing pulse

In terms of penetration depth this may be written:

$$n_e = \frac{R}{L_{photon}} \, \tau_e \quad . \tag{1-16}$$

For UV incident over 1 cm^2 for a time τ_p, an amount of IR energy will be outcoupled equal to Eq. (I-14) times the penetration depth $L_{electron} = L_{photon}.$* So, the conversion gain may be written:

_____

* For a single-step process, electron density falls at the same rate as the light flux.

52

$$C_g = \frac{\frac{n_e}{\tau_m} h\nu_{IR}\tau_p L_{photon}}{Rh\nu_{UV}\tau_p} \tag{I-17}$$

where $h\nu_{UV}$ is the ultraviolet photon energy. Using Eq. (I-16) in Eq. (I-17):

$$C_g = \frac{\tau_e}{\tau_m} \frac{\nu_{IR}}{\nu_{UV}} \epsilon \tag{I-18}$$

where the photoionization efficiency* has been inserted for completeness. This expression has a simple interpretation. Since high-energy UV photons are put in and low-energy IR photons out-coupled, the conversion gain suffers by the ratio of these energies. But each UV photon produces an electron which is recycled many times during its lifetime. This factor, τ_e/τ_m, is very large; for $\tau_e = 1$ μsec it is 4×10^4.

Assuming a 7-eV ionization potential seed molecule in a CO_2 laser, the photon energy ratio is approximately 1/50. With $\epsilon = 0.8$, $C_g \cong 600$.

Conversion Gain for Two-Step Photoionization

Consider the case in which a 7-eV IP seedant is ionized by the successive absorption of two photons. The first absorption populates intermediate states, i, with lifetime, τ_i, lying approximately half-way to the continuum. For a UV pulse of duration $\tau_p > \tau_i$, the intermediate state density is given by:

$$n_i = Rn\sigma_1\tau_i \tag{I-19}$$

R = rate of arrival of photons/cm^2 in the bandwidth
of the $1 \rightarrow i$ transition

n = density of tri-n-propylamine

σ_1 = cross section for photon absorption in $1 \rightarrow i$ transition

For a two-step process:

$$L_{photon} = \frac{1}{n\sigma_1} = 2L_{electron}$$

so Eq. (I-18) may be written in terms of $L_{electron}$:

$$n_i = \frac{R}{2L_{electron}} \tau_i \quad . \tag{I-20}$$

For a UV pulse with $\tau_p > \tau_e$, the equilibrium electron density is given by:

$$n_e = Rn_i\sigma\tau_e \quad . \tag{I-21}$$

For simplicity, the photon flux has been taken over the same bandwidth as the first step. This underestimates the overall efficiency since the $i \rightarrow e$ transition, e being the unbound state, is

---

* This is the fraction of those photons of energy exceeding the ionization potential which actually results in ionization. Typically, ϵ is in excess of 80 percent, the remainder of the photons resulting in molecular excitation or dissociation.

generally much broader than the $1 \rightarrow i$ transition. The photoionization cross section from the excited state is denoted by σ.

Using the definition of conversion gain and Eqs. (I-19) and (I-20), we may write the general expression which pertains when $\tau_p > \tau_e$ and $\tau_p > \tau_i$:

$$C_g = \frac{\frac{n_e}{\tau_m} h\nu_{IR}\tau_p L_{electron}}{Rh\nu_{UV}\tau_p}$$

or

$$C_g = \frac{1}{2} R\sigma\tau_i \frac{\tau_e}{\tau_m} \frac{\nu_{IR}}{\nu_{UV}} \epsilon \quad . \tag{I-22}$$

In this case ν_{UV} is approximately half that for the single-step ionization. The factor of 2 in the denominator may then be absorbed into the UV frequency factor in which case the two-step expression is simply the single-step expression reduced by the factor $R\sigma\tau_i$. This factor has a simple interpretation. Under the influence of a radiation field inducing transitions from the intermediate states to the continuum, the intermediate state suffers a loss of population at a rate of $R\sigma$ per second. We denote $1/R\sigma$ by τ_s, for "saturated lifetime." The intermediate lifetime has two components; one is denoted by τ_u and is attributable to processes other than saturation (e.g., radiative decay, collisional deactivation). The second component is the saturation effect. The proper expression for τ_i is:

$$\tau_i = \frac{1}{\frac{1}{\tau_u} + \frac{1}{\tau_s}} \quad . \tag{I-23}$$

Using this in Eq. (I-17):

$$C_g = \frac{1}{\tau_s} \frac{1}{\frac{1}{\tau_u} + \frac{1}{\tau_s}} \frac{\tau_e}{\tau_m} \frac{\nu_{IR}}{\nu_{UV}} \epsilon \quad . \tag{I-24}$$

It is seen in the limit of $1/\tau_s \gg 1/\tau_u$ that this expression converges to that for the single-step process. The extremely high conversion gain of the single-step ionization then is recaptured in the two-step process. Saturation of the intermediate state population, of course, calls for either a very high photon flux or very large cross section for photoionization from the intermediate state. Little is known at present about the photoionization cross sections for the large organic molecules presently used as seedants. A survey of the literature, however, shows that cross sections from the ground state as large as 10^{-16} to 10^{-15} cm^2 are not uncommon. Further, the scant data available on cross sections from excited states indicate that they may exceed the ground state cross section by two orders of magnitude. These two facts hold open the possibility that saturation of the intermediate state may be achieved with an attainable photon flux.

<div style="text-align: right">

A. Javan
J. S. Levine

</div>

d. Design of a Short and Chubby Photoelectron Pumped Laser

A large-aperture photoelectron-pumped CO_2-N_2-He gain cell has been designed to demonstrate the scalability of the technique. The active region has dimensions 15 cm $\times$ 15 cm $\times$ 30 cm;

hence the designation "short and chubby." The medium is to be seeded with tri-n-propylamine. Ionizing light flux is produced by two banks of 8 Xenon lamps each flanking the active region. Each lamp may be driven with a maximum of 200 joules in a 5-μsec pulse. Gain and homogeneity measurements will be performed. An optical resonator may be added to produce oscillation. Output of ~100 J is projected.

J. S. Levine

4. CO_2 Isotope Laser Measurements

The frequencies of $^{12}C^{18}O_2$, $^{13}C^{16}O_2$, and $^{13}C^{18}O_2$ isotope lasers have been measured to better than 3 MHz (0.0001 cm^{-1}) by comparison to a $^{12}C^{16}O_2$ reference laser. Heterodyne techniques were used to generate 139 difference frequencies in a liquid-nitrogen-cooled HgCdTe photodiode. Microwave frequency counter measurements of the difference frequencies were then used to calculate new values for the band centers and rotational constants of the rare isotopes.

It is shown that rare CO_2 isotopes can provide a many-fold expansion of the already highly useful spectral range of CO_2 lasers. In terms of number of lasing transitions, power output, gain, stability, and sealed-off CW operation characteristics, these three rare isotope lasers are generally similar to the commonly used $^{12}C^{16}O_2$ lasers. Since sealed-off CO_2 laser operating life times of over 10,000 hours have been reported by a number of laboratories, the additional cost of a few torr-liters of isotope required for a properly designed laser is not significant.

Laser beats to beyond 60 GHz have been detected by using a single high-speed HgCdTe photodiode as a microwave harmonic generator and frequency downconverter as well as an optical heterodyne receiver at 10.6 μm. This mode of operation has greatly reduced the problem of high-frequency attenuation and coupling loss, and has resulted in greatly improved signal-to-noise ratios. Although the photodiode was designed for a 1-GHz heterodyne receiver at 10.6 μm, its simultaneous use as a microwave mixer greatly improves its performance well above its roll-off frequency where the sensitivity drops by about 12 dB/octave. These varactor-photodiodes provide a very simple and effective means of precisely measuring and monitoring infrared laser line separations, since their 200-μm-diameter active area is easily brought into alignment and does not require focusing of the laser beams.

C. Freed   D. L. Spears
A. H. M. Ross   R. G. O'Donnell

5. Other Lasers

a. E-Beam Preionized CO_2 Laser

During this period, a short-pulse E-beam preionized CO_2 laser was developed for use in the surface-effects program. This device is an adaptation of a long-pulse E-beam laser previously reported.[33] A description of the laser will appear in the September 1973 issue of the Journal of Applied Physics. The Abstract of this publication is as follows:

A longitudinal electron beam was used to provide the preionization for a TEA-type CO_2 laser. Single-line energy in excess of 10 joules/liter at 10.6 μm can be obtained from this laser in approximately 2 μsec. This device may be simply converted to one previously reported which used the electron beam to provide the total ionization required for laser excitation and emits 20- to 120-μsec pulses of comparable energy.

S. Marcus   R. W. O'Neil
H. Kleiman   L. C. Pettingill

b. Feasibility of Electron-Beam-Ionized H_2-HF Transfer Laser

The chemically excited HF laser has the advantage of direct and potentially efficient utilization of chemical energy. However, the very fact that the laser does rely on chemical excitation introduces several seriously undesirable features. These include:

(1) The necessity of a continuous, single-pass flow of costly and highly toxic chemicals; and

(2) The difficulty of precise control over the reaction time and, hence, the laser pulse length.

The type of HF laser proposed below eliminates the requirement for chemical pumping and yet it retains the capability for high-power, efficient operation. The medium has the combined attributes of high-energy storage density and only moderate small-signal gain. This fact would make the device more amenable to scaling than standard HF chemical lasers where the prohibitively high gains at high reactant pressures permit the existence of parasitic modes.

The central idea associated with this new form of HF laser is that a population inversion in HF gas may be achieved for the condition of high vibrational temperature and low rotational temperature. Such a nonequilibrium is easily accessible in pulsed (or perhaps even CW) gas discharges. It is well-known, for example, that the electrically excited CO laser operates under these conditions.[34] For the case of the HF molecule, calculations of optical gain show that for an HF vibrational temperature of 4500°K, a rotational temperature of 300°K, and an HF pressure of 100 millitorr, one can achieve a gain of 0.3 percent/cm on the $P_1(7)$ transition.

Such conditions are probably obtainable in pure HF in an electron-beam-stabilized discharge. However, considerable advantage can be achieved by using the HF as a low-pressure dopant in a host of high-pressure H_2. One desirable aspect of such a mixture is that the primary energy storage species is the metastable H_2 molecule. Thus, the well-known rapid self-relaxation rate of the HF molecule is not a significant drain on the stored optical energy as it would be if all energy was stored in HF alone. Another advantage gained from the hydrogen host is that the vibrational temperature of the HF is determined by the transfer of vibrational energy from H_2 to HF. Because the H_2 energy-level spacing is slightly larger than that of HF, the HF vibrational temperature will be higher by a factor depending on the gas kinetic temperature and the energy difference. If, for example, H_2 has a 2700°K vibrational temperature, HF will be 4500°K. Thirdly, the discharge properties of H_2 are well-known and are much more desirable than the electronegative HF gas. The final point is that since the excited H_2 molecules do not contribute to the laser medium gain, the total laser gain (for a given H_2 vibrational temperature) is controlled solely by the HF partial pressure. Thus, by working at high H_2 and low HF pressure, one can achieve high energy storage for low laser gain. For example, if the initial H_2 pressure is 200 torr and its vibrational temperature is 2700°K, one can calculate that approximately 10 joules/liter of extractable optical energy is stored in the H_2 molecules. Note that for short-pulse operation, the pulse duration time is governed by the rate of energy transfer from H_2 to HF. For a mixture of 200 torr H_2 to 100 millitorr HF the transfer time is about 300 nsec. For long-pulse operation the maximum pulse length is governed by rotation-translational heating of the medium.

As stated above, a desirable method of achieving the required discharge properties for exciting the H_2-HF mixture is to use electron-beam preionization with a sustainer current supply. Such a system allows one to achieve an electric field-to-pressure ratio which is optimal for

exciting the vibrational levels of HF. In such a case, the electrical power of the discharge goes almost wholly into the laser levels of H_2.

At present, we are developing a workable theoretical model for vibrational excitation of H_2 in an E-beam sustained discharge. The model will be formulated in a manner similar to that given by Frost and Phelps[35] and Nighan[36] for discharges in molecular gases. With this model it should be possible to predict the optimum voltage-to-pressure ratios for vibrationally exciting H_2 gas and to ascertain the requisite n_e electron density for achieving the vibrational temperatures mentioned above. Plans are under way to verify the predictions of the model experimentally. This will be accomplished by exciting the gas mixture with a low-energy sustainer E-beam combination. By monitoring the HF infrared fluorescence it will be possible to measure the vibrational temperature as a function of pressure.

R. M. Osgood

c. HF Electric-Discharge Laser

Work was begun this period on the development of an electric-discharge HF laser. The goal of this program is to produce a laser which delivers 10 to 20 joules of near diffraction-limited energy for use in surface effects and propagation experiments.

As a first step, a 0.2-liter transverse-discharge laser was built. In this device, an SF_6H_2 discharge was struck between two opposing Rogowski-shaped electrodes by means of a 100-kV, 100-J Marx bank. Assuming an output energy density of 10 joules per liter as was obtained from a similar laser,[37] an output of 2 joules is expected.

The maximum output obtained thus far, however, is only 0.13 joules. This is due to the fact that most of the energy in the discharge appeared in the form of an arc rather than a uniform glow between the electrodes. This was not a problem in Ref. 37 since they were able to bring the discharge time down to ~100 nsec — too short a time for arcs to develop. To accomplish such short pulses requires reducing the inductance in the discharge circuit to an absolute minimum. We have redesigned our laser and Marx bank to achieve this and will soon be ready to test them out.

An attempt was also made to preionize the laser mixture by the technique of photoionization. There was a marginal increase in output energy (~10 percent) using flashlamps but no seed gas. This was attributed to photoemission from the electrodes. Addition of tri-n-propylamine[38] as a seed molecule, however, led to a decrease in output. An infrared spectrophotometer plot was taken which showed that tri-n-propylamine does not absorb at the laser wavelength of 2.7 µm. Accordingly, the observed decrease in output is not due to absorption but either collisional relaxation or inhibition of the chemical reaction.

A further marginal improvement in output was achieved by coating the cathode with a 50-ohm-cm conducting epoxy. This coating proved unsatisfactory, however, as it pitted easily when high-energy arcs occurred. Several electrodes are currently being surfaced with a newly-developed hard coating by Hughes Aircraft and will soon be tested.

S. Marcus

REFERENCES

1. J. Herrmann and L. C. Bradley, "Phase Compensation for Thermal Blooming," Appl. Opt. (to be published).

2. Luc R. Bissonnette, "Thermally Induced Nonlinear Propagation of a Laser Beam in an Absorbing Medium," Appl. Opt. $\underline{12}$, 719 (April 1973).

3. Yu. P. Raizer, Sov. Phys., JETP $\underline{21}$, 1009 (1965).

4. J. E. Lowder, D. E. Lencioni, T. W. Hilton, and R. J. Hull, J. Appl. Phys. June (1973).

5. L. C. Bradley, J. Herrmann, Optics Research Report, Lincoln Laboratory, M.I.T. (1971:1), p. 4, DDC AD-888823-L.

6. J. H. McCoy, D. B. Rensch and R. K. Long, Appl. Opt. $\underline{8}$, 1471 (1969).

7. T. S. Chu and D. C. Hogg, Bell Systems Tech. J. $\underline{47}$, 723-759 (1968).

8. G. L. Lamb and R. B. Kinny, J. Appl. Phys. $\underline{40}$, 416 (1969).

9. S. L. Glickler, Appl. Opt. $\underline{10}$, 644 (1971).

10. H. Kleiman and S. Marcus, J. Appl. Phys. $\underline{44}$, 1646 (1973).

11. S. Marcus, H. Kleiman, R. W. O'Neil and L. Pettingill, Optical Research Report, Lincoln Laboratory, M.I.T. (1973:1) (to be published).

12. R. J. Hull, D. E. Lencioni, and L. C. Marquet, Laser Interaction and Related Plasma Phenomena − II, H. J. Schwartz and H. Hora, Eds. (Plenum Press, 1972), p. 147.

13. H. Kleiman, and S. Marcus, J. Appl. Phys. $\underline{44}$ (April 1973).

14. D. E. Lencioni, Appl. Phys. Letters (1 July 1973).

15. D. E. Lencioni, and J. E. Lowder, IEEE/OSO Digest of Technical Papers, p. 76 (1 June 1973).

16. J. E. Lowder and H. Kleiman, Optics Research Report, Lincoln Laboratory, M.I.T. (1972:2).

17. R. E. Schlier, A. N. Pirri and D. J. Reilly, AFWL-TR-72-74 (February 1973).

18. R. W. O'Neil, H. Kleiman, L. C. Marquet, C. W. Kilcline, D. Northram, "Beam Diagnostics for High Energy Pulsed CO_2 Lasers," submitted for publication to Appl. Opt. (1973).

19. R. W. O'Neil, L. C. Marquet, J. E. Lowder, D. E. Lencioni, C. W. Kilcline, H. Kleiman, T. W. Hilton and R. J. Hull, LTP-17, Lincoln Laboratory, M.I.T. (28 September 1972).

20. J. E. Lowder, D. E. Lencioni, R. W. O'Neil, L. C. Marquet, C. W. Kilcline, T. W. Hilton and H. Kleiman, LTP-18, Lincoln Laboratory, M.I.T. (22 January 1973).

21. J. A. Charest, EG&E Inc., Santa Barbara Division, personal communication (March 1973).

22. J. E. Lowder and H. Kleiman, Appl. Phys. Letters (to be published).

23. See, for instance, Plasma Diagnostic Techniques, by Huddlestone and Leonard (Academic Press, 1965), Optical Interferometry, by Alpher and White, pp. 431-477.

24. Hall and Chang, J. Appl. Phys.

25. A. J. Morency, Optics Research Report, Lincoln Laboratory, M.I.T. (1972:2), DDC AD-7623200.

26. R. W. O'Neil et al., "Beam Diagnostics for High Energy Pulsed CO_2 Lasers," submitted to Appl. Opt. for publication.

27. H. Granek and A. J. Morency, "Experimental Study of Large Effective Fresnel Number Confocal Unstable Resonators," Conference on Laser Engineering and Applications, Washington, D.C., 30 May − 1 June 1973.

28. A. E. Siegman, "Stabilizing Output with Unstable Resonators," Laser Focus, 44-47 (May 1971).

29. Optics Research, Lincoln Laboratory, M.I.T. (1972:2), pp. 13-15.

30. A. Javan and J. S. Levine, IEEE J. Quantum Electron. QE-8, 827 (1972).

31. J. S. Levine and A. Javan, Appl. Phys. Letters 22, 55 (15 January 1973).

32. Optics Research Report, Lincoln Laboratory, M.I.T. (1972:2), pp. 27-28.

33. S. Marcus, Appl. Phys. Letters 21, 18 (1972).

34. J. W. Rich, J. Appl. Phys. 42, 2719 (1971).

35. L. S. Frost and A. V. Phelps, Phys. Rev. 127, 1621 (1962).

36. W. L. Nighan, Phys. Rev. (A) 2, 1989 (1970).

37. G. P. Arnold and R. G. Wenzel, IEEE J. Quantum Electron. QE-9, 491 (April 1973).

38. J. S. Levine and A. Javan, Appl. Phys. Letters 22, 55 (1973).

II. OPTICAL MEASUREMENTS AND INSTRUMENTATION

A. OPTICAL BOUNDARY LAYER MTF MEASUREMENTS*

1. Introduction

Wind-tunnel tests were carried out during October and November 1972 at the NASA Ames 14-foot transonic wind tunnel using the shearing interferometer.[1] MTF measurements were made with the airfoil reflector designed for boundary-layer tests and previously flown on the Lincoln Laboratory KC-135 jet aircraft (Project PRESS program).[2]

Theoretical calculations of the expected MTF (based in part on the earlier results of photometric scattering data obtained by Stine and Winovich[3]), for both the wind-tunnel experiment and the flight tests, were then carried out and compared with the experimentally measured MTF data here.

2. MTF Measurements in the Wind Tunnel

The airfoil was mounted inside the wind tunnel on the inner wall, as shown in Fig. II-1. The interferometer and the laser source (a CW HeNe laser) were mounted on a tripod outside the tunnel next to the outer wall, as shown in Fig. II-2. An aerodynamically designed tube (the airflow shield) could be fitted (as before[2]) between the gold-coated mirror and the tunnel wall window to completely enclose and shield the light path inside the wind tunnel from the boundary layer. About 30 runs to measure the MTF were made in the wind tunnel, with and without the boundary layer (when the air shield was out or in), at various wind speeds up to Mach 0.9.

The peak amplitude ("best seeing") of the signal was taken over each 20-second interval for each interferometer shear setting over the full shear range to obtain a complete MTF curve. Several MTF curves were thus obtained at each tunnel condition. The wind speed was varied, and in some cases different tunnel temperatures were run as measurements were taken. There was no obvious correlation in the data between the MTF and tunnel or outer window (laboratory ambient) temperature. The mean of all the MTF curves for each wind speed, with or without the boundary layer, was obtained from the data, and is shown in Fig. II-3. MTF data obtained during changing tunnel conditions or where the focusing was uncertain, have not been used here. The maximum deviation of any MTF curve (each curve was a relatively smooth curve) from its mean, is indicated by bars in Fig. II-3. On the same figure, the optical diffraction-limited curve (for a clear 24-mm-diameter beam) is shown, together with the previous KC-135 flight boundary-layer MTF measurements (mean curves) obtained with the same airfoil.

There is essentially little degradation being produced in the wind tunnel, and it is significantly less than the KC-135 flight curves. The main uncertainty here is that we did not get diffraction-limited performance when the boundary layer was excluded (airfoil air shield in place) from the light path, as was the case in the flight measurements. On the other hand, the degradation did not get any worse when the air shield was removed. Effectively we measured no significant difference in the peak MTF when the tunnel was running, with or without the boundary layer, when all the runs were averaged. Humidity conditions were quite variable and may have influenced the separate MTF measurements to yield a spread of curves. With the tunnel off,

---

*This report describes the work performed at Lincoln Laboratory under the sponsorship of the Air Force Weapons Laboratory.
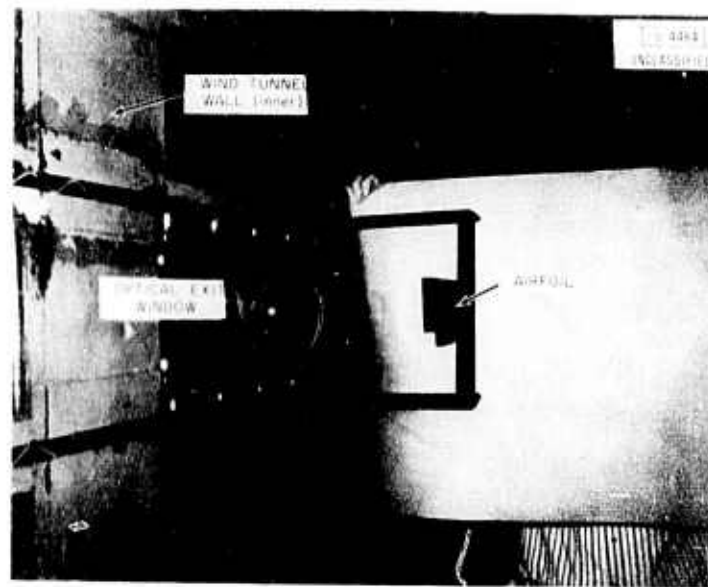
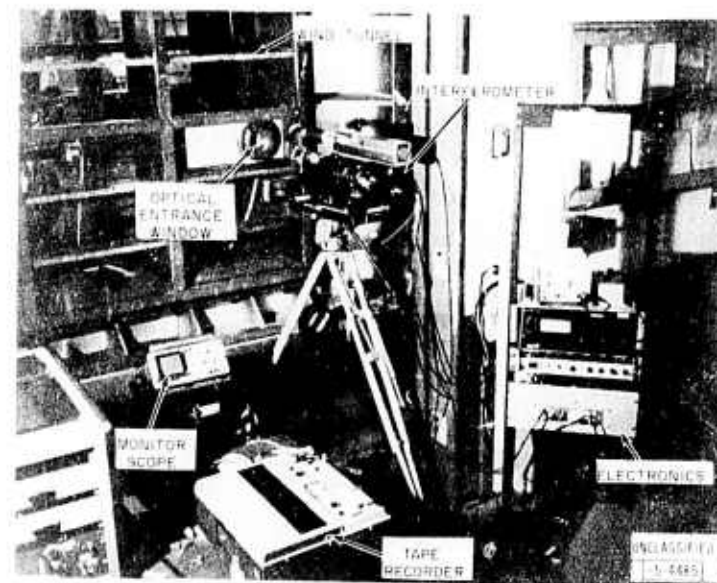Fig. II-1. Airfoil location inside wind tunnel.

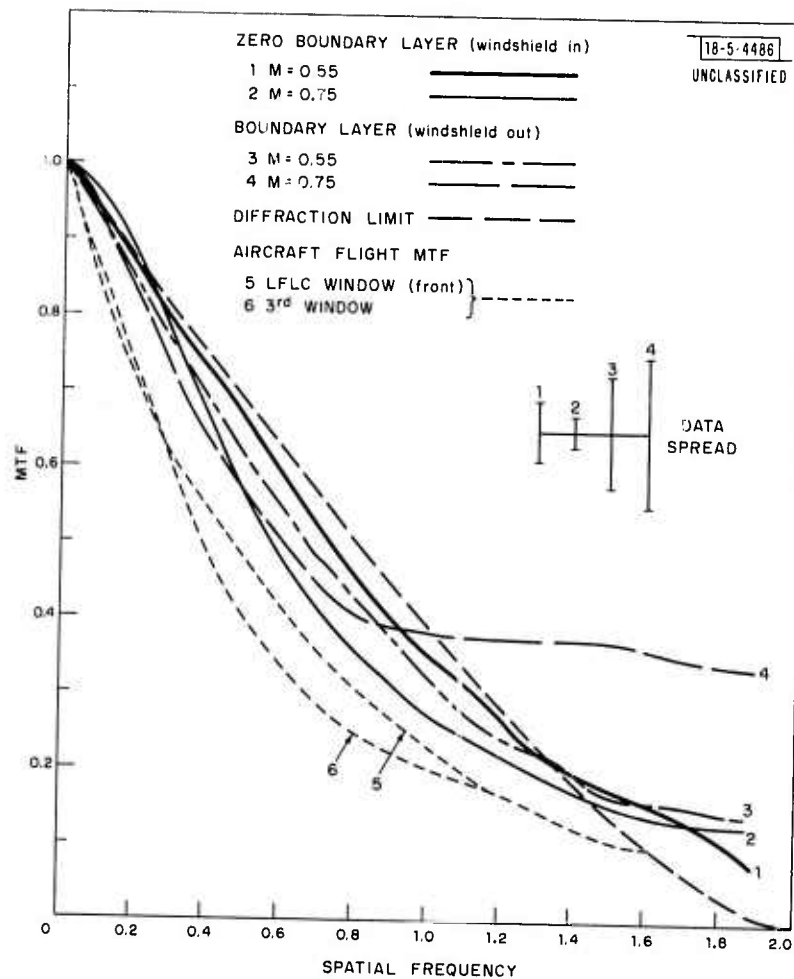Fig. II-2. Interferometric equipment outside wind tunnel.

Fig. II-3. Wind-tunnel boundary-layer MTF measurements.

the measured MTF was diffraction limited. Some additional (and slightly variable) degradation in our light path does occur with the tunnel running, but this is not due to the boundary layer. The cause of the different MTF results from the wind tunnel and flight measurements is probably due to the different temperature characteristics in each case. The ambient temperature in the flight environment is about $-30°$ to $-40°C$, while in the wind tunnel it is from $+25°$ to $+50°C$.

The wind-tunnel boundary layer is roughly 20 cm thick, and operation was close to atmospheric pressure. The flight measurements were made cruising at about 1' km altitude, where the pressure is one third that of atmospheric, and the boundary-layer thicknesses at the front and mid-section windows were calculated to be 8 cm and 17 cm. The airplane optical window, due to fuselage curvature, was slightly recessed (about 1 inch maximum), but the wind-tunnel window was mounted flush and smooth with the wall.

3. Computation of the MTF from Refractive Index Fluctuations

An analysis of earlier wind-tunnel experiments such as those of Stine and Winovich[3] can be made in order to predict the MTF expected in the flight and in the wind-tunnel boundary-layer measurements. The boundary-layer MTF can thereby be computed and compared with the measurements reported here. Details of this calculation are given in Ref. 4 and only the results will be summarized here.

The refractive index fluctuations in the boundary layer can be estimated in each experiment and the corresponding rms wavefront deformation, σ, determined for the various boundary-layer conditions. The MTF [$D(s)$] can then be calculated in each case from the relationship (for a double pass through the boundary layer), between $D(s)$ and σ,

(a) Wind tunnel: $D(s) = D_o(s) \exp-[k^2\sigma^2(1 - \exp-0.018\ s^2)]$

(b) KC-135 flight: $D(s) = D_o(s) \exp-[k^2\sigma^2(1 - \exp-0.81\ s^2)]$

where $D_o(s)$ is the optical diffraction-limited MTF, k is $2\pi/\lambda$, and s is the interferometer shear (reduced spatial frequency). The values of σ in each case were calculated to be, $\sigma \sim \lambda/5$ in the wind tunnel; $\lambda/29$ and $\lambda/14$, respectively, for the front and mid-section window in the airplane tests. Using these numbers, the MTF in the wind tunnel is diffraction limited, the flight test MTF at the front window again is diffraction limited, while the flight test MTF at the mid-section window is about 6 percent lower. The computed and measured flight MTF curves are shown for comparison in Fig. 11-4.

4. Conclusion

The calculated and measured MTF curves for the wind-tunnel boundary layer are close to diffraction limited, showing no degradation. The measured flight MTF curves (at 11 km altitude) are much lower than either of the above and than the computed flight MTF curves. However, the difference (about 6 percent) between the front and mid-section windows of the aircraft, respectively, shows up in both the measured and computed flight MTF curves. This implies that in the airborne case some additional refractive index fluctuations arise, not predicted by the usual aerodynamical boundary-layer analysis.

These larger fluctuations probably arise from the fact that the ambient temperature in the flight environment at 11 km altitude is considerably lower than that in the wind tunnel. In future
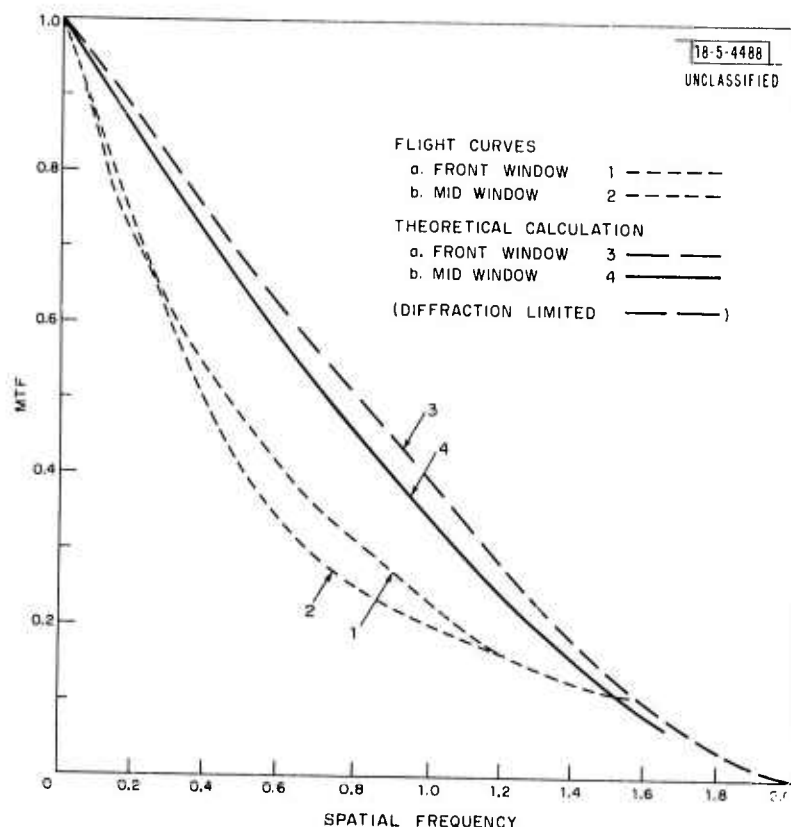
Fig. II-4. Comparison of computed and measured flight boundary-layer MTF curves.

wind-tunnel experiments it is suggested that experiments be done placing a cooled (refrigerated) plate downstream from the test area, to introduce larger temperature fluctuations in the boundary layer. Attempts can then be made to match the flight data with wind-tunnel data.

It is therefore concluded that present wind-tunnel optical experiments may not provide real-istic measurements for the corresponding flight cases. The measured MTF in the actual flight case has been found to be poorer than that anticipated from both earlier and our own wind-tunnel data.

<div align="right">D. Kelsall</div>

B. DIODE LASER SYSTEM FOR MONITORING STACK GASES*

A system utilizing semiconductor diode lasers for the detection of SO_2 by differential infrared absorption was developed and field-tested on the smoke stack of an operating power generation station. This work was described in detail in a Final Report to the Environmental Protection Agency, "Development of In Situ Prototype Diode Laser System to Monitor SO_2 across the Stack." A summary of this Report follows:

Eventual application of tunable lasers in air pollution monitoring has been significantly advanced by recent developments both in laser technology and in the realization that certain remote sensing techniques can become more sen-sitive and specific when tunable lasers are used. Semiconductor diode lasers

---

*This report describes the work performed at Lincoln Laboratory under the sponsorship of the Environmental Protection Agency.

have been in the forefront of these advances because of their ability to match strong infrared spectral lines of the known pollutant gases, their simplicity of design and operation, and prospects for low ultimate cost.

This program followed a previous year's effort of broader scope, during which point sampling, source monitoring, and ambient air monitoring by resonance absorption were investigated, as well as remote heterodyne detection. Diode lasers were developed to operate in the 1100 to 1200 cm^{-1} region corresponding to the ν_1 band of SO_2; its fundamental infrared band structure parameters were measured, and the results published.

For this year's effort new lasers were fabricated for a selected narrow wavelength region (1120 to 1130 cm^{-1}) appropriate for source monitoring of SO_2, i.e., where the line strengths are strong, but relatively independent of temperature. Improvements during the year resulted in diode lasers with power levels more than ten times greater than the best achieved earlier. Various monitoring schemes were considered, and one was selected which involved a single laser operating pulsed at two different wavelengths approximately 1 cm^{-1} apart, where the tuning of alternate pulses was accomplished by a third controllable current pulse of relatively long duration. System linearity was confirmed over a wide range of SO_2 concentrations, and the system response was also checked for day-to-day reproducibility. Measurements of interference rejection were made by using varying amounts of smoke, water vapor, steam, ammonia (NH_3), and ethylene (C_2H_4). As the program progressed, in-stack experiments were performed several times at an oil-burning power plant in order to produce information useful for final system design. At the end of the program, measurements were made at a coal-burning power plant, and the resulting SO_2 determination was compared with data obtained with a point-sampling monitor.

<div align="right">
E. D. Hinkley
A. R. Calawa
</div>

C. WAVELENGTHS FOR TUNABLE INFRARED LASER DETECTION OF NO, CO, O_3, AND SO_2 IN THE 3- TO 5-μm ATMOSPHERIC "WINDOW"[*]

Our present efforts in air pollution monitoring with tunable semiconductor diode lasers are directed toward long-path (~2 km) monitoring of NO, CO, O_3, and SO_2 in the atmosphere. This report describes the selection of optimal wavelengths for the detection of these gases in the 3- to 5-μm atmospheric "window." For SO_2 and O_3 there are stronger absorption bands in other regions of the infrared; however, by restricting consideration to the 3- to 5-μm region, a single infrared detector may be used for all the gases under consideration — namely, an InSb photodiode. Similarly, a single type of semiconductor compound ($PbS_{1-x}Se_x$) may provide all the necessary diode lasers.

The atmospheric transmission spectra to be shown here were taken from reports prepared by McClatchey,[5] and McClatchey and Selby,[6] containing computer-generated spectra based upon

experimental measurements of the line strengths and wavelengths of gaseous atmospheric constituents, as well as representative concentrations. The data correspond to a 10-km path at sea level, in winter at midlatitude, for which the amount of water vapor over a 10-km path is assumed to be 3.5 precipitable centimeters. Although we are considering shorter pathlengths, it must be realized that there can be several times more water vapor present during summer, which tends to cancel the better transmission that would be expected[7] for a 2-km path length. The transmission data in the region which we are considering take into account molecular absorption by H_2O, CO_2, O_3, CO, and N_2O.

Nitric Oxide

Strong absorption lines in the fundamental vibration-rotation band of NO exist from 1830 to 1930 em^{-1} (Ref. 8), all of which is a region of strong water vapor absorption.[9] There are, however, R-branch transitions of NO which exist within partial "windows" in the H_2O absorption, as indicated in Fig. II-5 around 1882, 1900, 1930, and 1936 em^{-1}. Superimposed on the atmospheric transmission data are the NO absorption lines, with the lengths of the solid vertical bars indicating their relative strengths. Because of uncertainty in the actual shapes of these small "windows," which is important for narrow-line tunable laser transmission, initial consideration must be given to both the 1900 and 1930 em^{-1} regions where reasonably strong NO lines exist. The strongest NO line is $R(13/2)_{1/2}$ at 1900.13 em^{-1}. Next is the $R(33/2)_{1/2}$ line within the apparently better "window," at 1929.08 em^{-1}. Which of these lines is ultimately selected will depend on the high-resolution atmospheric-transmission measurements to be performed with tunable diode lasers.

Carbon Monoxide

Since it is a natural constituent of our normal (somewhat polluted) atmosphere, CO was included in the computer transmission spectra around 4 μm, as shown in Fig. II-6. The relative strengths of the CO lines are also indicated.[10] Most of the (non-CO) atmospheric absorption in this region is due to water vapor, so the choice of an appropriate line for monitoring CO is reduced to selecting one in a region that is furthest away from H_2O absorption. On the basis of Fig. II-6, the best CO lines are: P(4) at 2127.69 em^{-1} and P(3) at 2131.64 em^{-1}. Between these transitions is another strongly-absorbing line, probably due to atmospheric CO_2.

Ozone

Infrared absorption due to the $\nu_1 + \nu_3$ and $2\nu_3$ bands of O_3 overlaps the CO absorbing region described above. For this reason, it is possible that the same semiconductor laser, or at least the same material, can be used for monitoring both these gases. The atmospheric transmission and superimposed O_3 relative absorption strengths are indicated in Fig. II-7 (Ref. 11). There is not much more than a factor of two variation in line strength over the region from 2080 to 2130 em^{-1}, and there are 15 lines which could be used, as indicated by the arrows. Since several lines are present between 2120 and 2130 em^{-1}, which is near the wavenumbers selected for CO detection, it would appear that this region would be best for O_3 detection as well.
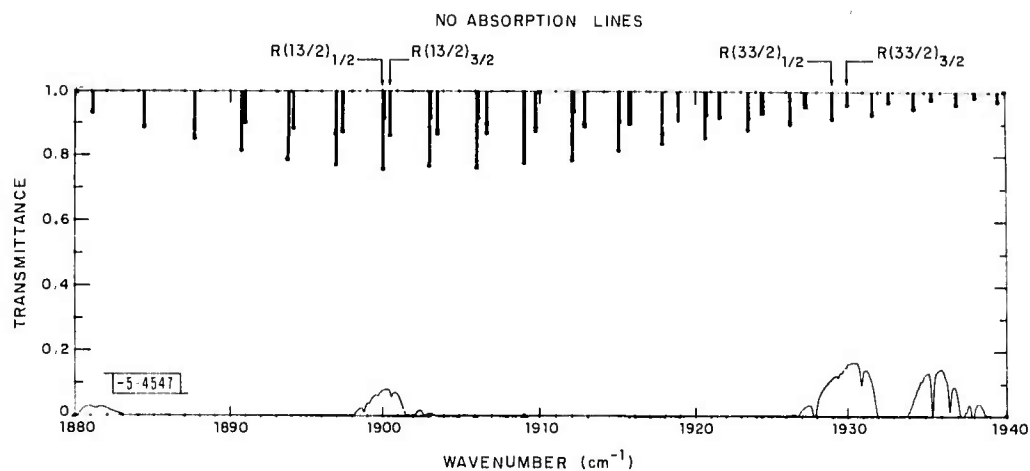
Fig. II-5. Atmospheric transmission between 1880 and 1940 cm^{-1}, as computed for 10-km path at sea level during midwinter humidity conditions. Locations and strengths of NO absorption lines are also indicated.
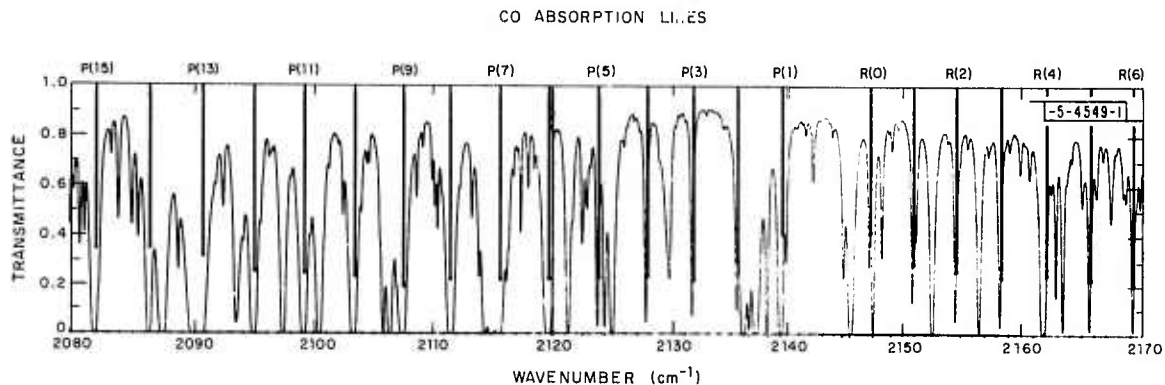

Fig. II-6. Atmospheric transmission between 2080 and 2170 cm^{-1}, as computed for 10-km path at sea level during midwinter humidity conditions. Locations and relative strengths of CO absorption lines are also indicated.
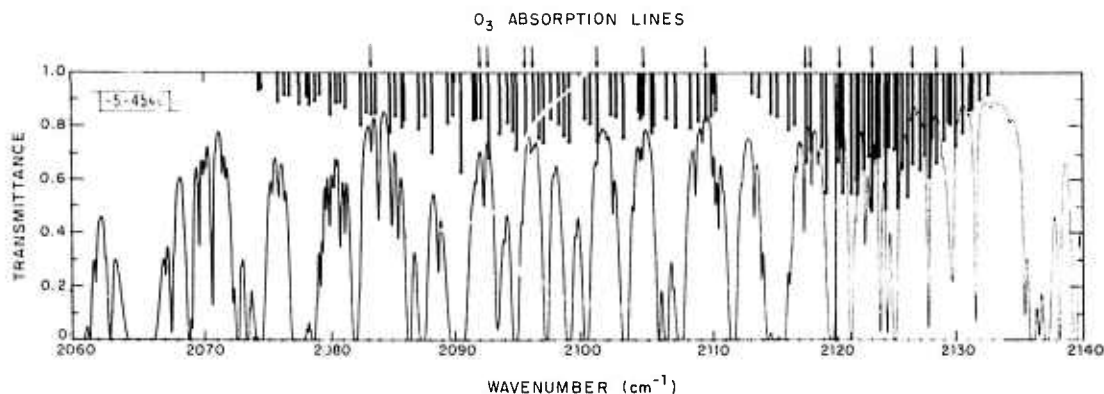
O$_3$ ABSORPTION LINES

WAVENUMBER (cm^{-1})

Fig. II-7. Atmospheric transmission between 2060 and 2140 cm^{-1}, as computed for 10-km path at sea level during midwinter humidity conditions. Locations and relative strengths of O$_3$ absorption lines are also indicated.

Sulfur Dioxide .

The $\nu_1 + \nu_3$ combination band of SO$_2$ extends from 2465 to 2525 cm^{-1}, and is comprised of many lines, as shown in Fig. II-8 (Ref. 12). Because of overlap between adjacent atmospheric-pressure-broadened lines, the base line for SO$_2$ detection is not at the top of the figure, as it was for the other three gases discussed here, but is represented by the solid line sketched through the absorption-strength trace, designated as "SO$_2$ base line." There are many relatively strong SO$_2$ lines between 2482 and 2493 cm^{-1} and between 2508 and 2515 cm^{-1}. Although background absorption is somewhat larger in the former region, it may well be possible to use relatively strong technologically advanced PbS diode lasers for detection of SO$_2$, rather than having to grow a different type of crystal, $Pb_{1-x}Cd_xS$, to produce laser emission around 2510 cm^{-1}.

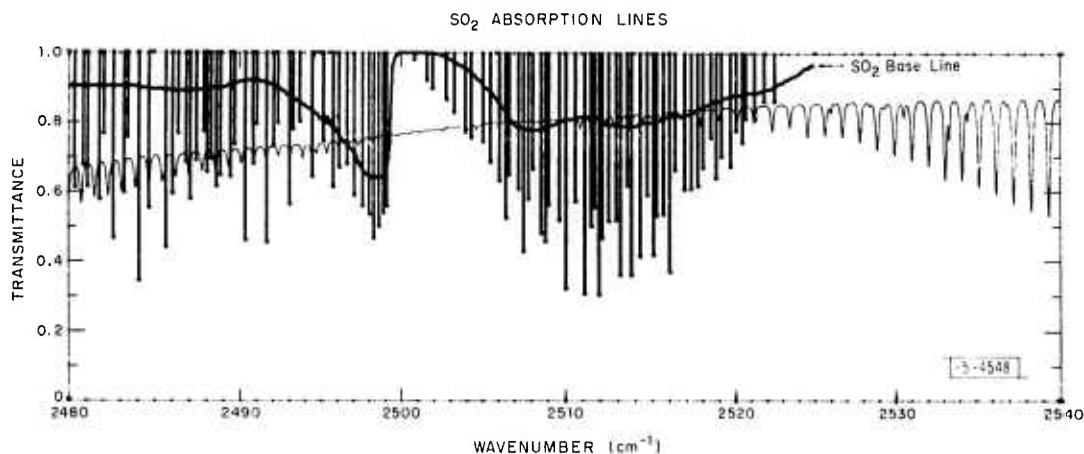SO$_2$ ABSORPTION LINES

WAVENUMBER (cm^{-1})

Fig. II-8. Atmospheric transmission between 2480 and 2540 cm^{-1}, as computed for 10-km path at sea level during midwinter humidity conditions. Locations and relative strengths of SO$_2$ absorption lines are also indicated.

Summary:— The following table summarizes the optical wavelengths for detecting the four gases in the atmosphere:

TABLE II-1 OPTIMUM DETECTION REGIONS			
Gas	Transitions	cm^{-1}	Principal Interferant(s)
NO	$R(13/2)_{1/2}$	1900.13	H_2O
	$R(33/2)_{1/2}$	1929.08	H_2O
CO	P(4)	2127.69	H_2O, O_3
	P(3)	2131.64	H_2O, O_3
O_3	Various	2120-2130	H_2O, CO
SO_2	Various	2482-2493	CO_2

E. D. Hinkley

REFERENCES

1. Optics Research Report, Lincoln Laboratory, M.I.T. (1970:3), p. 35, DDC AD-882617.

2. Optics Research Report, Lincoln Laboratory, M.I.T. (1972:1), p.62, DDC AD-754939.

3. H. A. Stine and W. Winovich, "Light Diffusion through High-Speed Turbulent Boundary Layers," NACA RM A56B21 (25 May 1956).

4. Semiannual Report AFWL (December 1972).

5. R. A. McClatchey, Technical Report AFCRL-71-0370 (1 July 1971).

6. R. A. McClatchey and J. E. A. Selby, Technical Report AFCRL-72-0312 (23 May 1972).

7. D. L. Ford, Technical Report RADC-TR-72-140 (April 1972).

8. J. H. Shaw, J. Chem. Phys. 24, 397 (1956).

9. D. E. Burch, D. A. Gryvnak and J. D. Pembrook, Technical Report AFCRL-TR-73-0092.

10. Commission on Molecular Structure and Spectroscopy, Tables of Wavenumbers for the Calibration of Infrared Spectrometers (Butterworths, London, 1961), p. 581.

11. S. A. Clough, unpublished.

12. R. J. Corice, Jr., K. Fox and G. D. T. Tejwani, Technical Report UTPA-ERAL-03 (December 1972).